

REPORT DOCUMENTATION PAGE

Form Approved
OMB No. 0704-0188

Public reporting burden for this collection of information is estimated to average 1 hour per response, including the time for reviewing instructions, searching existing data sources, gathering and maintaining the data needed, and completing and reviewing this collection of information. Send comments regarding this burden estimate or any other aspect of this collection of information, including suggestions for reducing this burden to Department of Defense, Washington Headquarters Services, Directorate for Information Operations and Reports (0704-0188), 1215 Jefferson Davis Highway, Suite 1204, Arlington, VA 22202-4302. Respondents should be aware that notwithstanding any other provision of law, no person shall be subject to any penalty for failing to comply with a collection of information if it does not display a currently valid OMB control number. PLEASE DO NOT RETURN YOUR FORM TO THE ABOVE ADDRESS.

1. REPORT DATE (DD-MM-YYYY) 11/30/2011		2. REPORT TYPE Final Technical Report		3. DATES COVERED (From - To) 08/01/2008 -011/30/2011	
4. TITLE AND SUBTITLE Testing and Modeling Ultra-High Temperature Ceramic (UHTC) Materials for Hypersonic Flight				5a. CONTRACT NUMBER FA9550-08-C-0049	5b. GRANT NUMBER
				5c. PROGRAM ELEMENT NUMBER	
6. AUTHOR(S) Marschall, Jochen				5d. PROJECT NUMBER SRI P18570	5e. TASK NUMBER
				5f. WORK UNIT NUMBER	
7. PERFORMING ORGANIZATION NAME(S) AND ADDRESS(ES) SRI International 333 Ravenswood Ave. Menlo Park, CA 94025				8. PERFORMING ORGANIZATION REPORT NUMBER MP 11-078	
9. SPONSORING / MONITORING AGENCY NAME(S) AND ADDRESS(ES) Air Force Office of Scientific Research Directorate of Aerospace, Chemistry and Material Sciences 875 N. Randolph Street, Suite 325, Room 3112 Arlington, VA 22203-1768				10. SPONSOR/MONITOR'S ACRONYM(S) AFOSR/PK2	
				11. SPONSOR/MONITOR'S REPORT NUMBER(S) AFRL-OSR-VA-TR-2012-0295	
12. DISTRIBUTION / AVAILABILITY STATEMENT Distribution Statement A. Approved for public release; distribution is unlimited or as the Contracting Officer suggested (publicly releasable).					
13. SUPPLEMENTARY NOTES					
14. ABSTRACT This project focused on zirconium diboride and hafnium diboride ultra-high temperature ceramics in two main research areas: i) their thermal and electrical transport properties; and ii) their oxidation and volatilization behavior in simulated re-entry environments. The first area involved experimental studies of the thermal and electrical properties as a function of temperature, and the analysis of these results in terms of effective conductivity and Wiedemann-Franz models. Thermal diffusivity was measured using a photothermal radiometry technique, and the electrical resistivity and Hall coefficient were measured using a van der Pauw geometry. The second area involved experiments under simulated re-entry heating conditions at the 1.2 MW Plasmatron facility of the von Karman Institute for Fluid Dynamics in Rhode-Saint-Genese, Belgium. Zirconium diboride materials were tested over a range of surface temperatures exceeding 2000°C. A temperature-jump phenomenon was observed at threshold heating levels, at which the surface temperature spontaneously increased by hundreds of degrees under constant free-stream test conditions. This temperature jump is thought to be related to an abrupt transition in surface chemistry at the gas-surface interface. Both areas of research contribute to the continuing development of diboride-based materials for leading-edge applications on future hypersonic flight vehicles.					
15. SUBJECT TERMS Ultra High Temperature Ceramics, hafnium diboride, zirconium diboride, thermal properties, electrical properties, oxidation, hypersonics					
16. SECURITY CLASSIFICATION OF: a. REPORT U		17. LIMITATION OF ABSTRACT b. ABSTRACT UU	18. NUMBER OF PAGES c. THIS PAGE SAR	19a. NAME OF RESPONSIBLE PERSON Jochen Marschall	
				19b. TELEPHONE NUMBER (include area code) 650-859-2667	

Final Report • November 2011

Testing and Modeling Ultra-High Temperature Ceramic (UHTC) Materials for Hypersonic Flight

SRI Project Number: P18570

AFOSR Contract No. FA9550-08-C-0049

MP 011-078

Prepared by:

Dr. Jochen Marschall
Molecular Physics Laboratory
SRI International

Prepared for:

Dr. Ali Sayir, Program Manager
High Temperature Aerospace Materials
Directorate of Aerospace, Chemistry and Materials Science Air Force Office of Scientific Research
875 North Randolph Street
Suite 325, Room 3026
Arlington, Virginia 22203



INTRODUCTION

This report summarizes the activities and results of experimental and modeling work performed for the Air Force Office of Scientific Research (AFOSR) under Contract FA9550-08-C-0049, "Testing and Modeling Ultra-High Temperature Ceramic (UHTC) Materials for Hypersonic Flight." The period of performance was 08/01/2008 to 11/30/2011. This project focused on two main research areas: i) thermal and electrical transport properties; and ii) oxidation/volatilization behavior in simulated re-entry environments.

The first area involved experimental studies of the thermal and electrical properties of UHTC materials as a function of temperature and the analysis of these results in terms of effective conductivity and Wiedemann-Franz models. Thermal diffusivity was measured using a photothermal radiometry technique, and the electrical resistivity and Hall coefficient were measured using a van der Pauw geometry. Studies were performed on various ZrB₂- and HfB₂-based UHTC materials manufactured using conventional and spark plasma sintering.

The second area involved experiments under simulated re-entry heating conditions conducted at the 1.2 MW Plasmatron facility of the von Karman Institute for Fluid Dynamics in Rhode-Saint-Genese, Belgium. ZrB₂-based UHTCs manufactured by pressureless sintering techniques at the Missouri University of Science and Technology were tested over a range of surface temperatures exceeding 2000 °C. A temperature-jump phenomenon was observed at threshold heating levels, at which the surface temperature spontaneously increased by hundreds of degrees under constant free-stream test conditions. This temperature jump is thought to be related to an abrupt transition in surface chemistry at the gas-surface interface.

In addition, research has been performed in the areas of high-velocity impact resistance, O-atom oxidation of UHTC materials, material property requirements for UHTC component design, and *in situ* optical diagnostics for re-entry heating test characterization and documentation. The results of this research have led to 5 presentations at various conferences and meetings, and have been written up in 6 technical publications (5 published and 1 submitted). Three further manuscripts are under preparation.

SUMMARY OF EFFORTS AND ACCOMPLISHMENTS

Research efforts and accomplishments are summarized in abstract form below. Comprehensive details are found in the attached Appendices (A1-A4), which incorporate edited versions of published or submitted papers.

A1) Temperature Jump Phenomenon during Plasmatron Testing of ZrB₂-SiC Ultra-High Temperature Ceramics (submitted to the AIAA Journal of Thermophysics and Heat Transfer, August 2011)

The performance of ZrB₂-SiC ultra high temperature ceramic composites in subsonic high-enthalpy dissociated air flows was investigated in the 1.2 MW Plasmatron facility at the

von Karman Institute for Fluid Dynamics (VKI). Samples manufactured by pressureless sintering at the Missouri University of Science and Technology (Missouri S&T) were sequentially exposed to low heat flux and high heat flux conditions during a single test run by adjusting the Plasmatron power. During some high heat flux conditions, we observed a rapid and spontaneous rise in sample surface temperature under constant freestream conditions. We associate this temperature jump with a transition in surface chemistry that leads to the loss of protective silica glass and substantially increases the chemical component of heat flux delivered to the surface. These tests provide the first set of experimental observations that characterize a temperature jump phenomenon in a diboride/silica former UHTC composite.

A2) Thermal and Electrical Transport Properties of Spark Plasma Sintered HfB₂ and ZrB₂ Ceramics (The Journal of the American Ceramic Society, Vol. 94(8), 2011, pp. 2562-2570.)

The thermal and electrical transport properties of various spark-plasma-sintered HfB₂- and ZrB₂-based polycrystalline ceramics were investigated experimentally over the 300–700 K temperature range. Measurements of thermal diffusivity, electrical resistivity, and Hall coefficient are reported, as well as the derived properties of thermal conductivity, charge carrier density, and charge carrier mobility. Hall coefficients were negative, confirming electrons as the dominant charge carrier, with carrier densities and mobilities in the $3.5 \times 10^{21} \text{ cm}^{-3}$ and $100\text{--}250 \text{ cm}^2 \text{ V}^{-1} \text{ s}^{-1}$ ranges, respectively. Electrical resistivities were lower, and temperature coefficients of resistivity were higher than those typically reported for HfB₂ and ZrB₂ materials manufactured by conventional hot pressing. A Wiedemann-Franz analysis confirms the dominance of electronic contributions to heat transport. The thermal conductivity was found to decrease with increasing temperature for all materials. Results are discussed in terms of sample morphology and compared to data previously reported in the scientific literature.

A3) High-Enthalpy Test Environments, Flow Modeling and In Situ Diagnostics for Characterizing Ultra High Temperature Ceramics (The Journal of the European Ceramic Society, Vol. 30, 2010, pp. 2323-2336.)

Ultra-high temperature ceramic materials and composites under development as nose-tip and wing leading edge components for hypersonic flight vehicles must operate in extreme aerothermal heating environments. The performance of UHTCs for this application is ultimately evaluated using high-enthalpy, long-duration flow facilities that simulate the reactive gas environment encountered in hypersonic flight. In this paper, we describe the test environments generated by two types of these ground test facilities—subsonic inductively-coupled plasma tunnels and supersonic arc-jet tunnels—and discuss the important roles of computational fluid dynamics modeling and *in situ* optical diagnostics for interpreting test results from a materials science perspective.

A4) *Material Property Requirements for Analysis and Design of UHTC Components in Hypersonic Applications* (*The Journal of the European Ceramic Society*, Vol. 30, 2010, pp. 2239-2251.)

Analytical modeling of thermal and mechanical response is a fundamental step in the design process for UHTC components, such as nose tips and wing leading edges for hypersonic applications. The purpose of the analyses is to understand the response of test articles to high-enthalpy flows in ground tests and to predict component performance in particular flight environments. Performing these analyses and evaluating the results require comprehensive and accurate physical, thermal, and mechanical properties. In this paper, we explain the nature of the analyses, highlight the essential material properties that are required and why they are important, and describe the impact of property accuracy and uncertainty on the design process.

ACKNOWLEDGMENT/DISCLAIMER

This work was sponsored by the Air Force Office of Scientific Research, USAF, under Contract FA9550-08-C-0049. The views and conclusions contained herein are those of the author and should not be interpreted as necessarily representing the official policies or endorsements, either expressed or implied, of the Air Force Office of Scientific Research or the U. S. Government.

ONSITE PERSONNEL SUPPORTED

During the course of this project, the following SRI individuals received support from AFOSR Contract FA9550-08-C-0049:

Jochen Marschall	Senior Research Scientist, Molecular Physics Laboratory
Dusan Pejaković	Research Physicist, Molecular Physics Laboratory
Bill Olson	Engineering Assistant, Molecular Physics Laboratory
Luning Zhang	Post-doctoral Researcher, Molecular Physics Laboratory

PUBLICATIONS

J. Marschall, D. A. Pejaković, W. G. Farhnholtz, G. E. Hilmas, F. Panerai, and O. Chazot, "Temperature Jump Phenomenon during Plasmatron Testing of ZrB₂-SiC Ultra-High Temperature Ceramics," *Journal of Thermophysics and Heat Transfer*, Submitted, August, 2011.

L. Zhang, D. A. Pejaković, J. Marschall, and M. Gasch, "Thermal and Electrical Transport Properties of Spark Plasma Sintered HfB₂ and ZrB₂ Ceramics," *Journal of the American Ceramic Society*, Vol. 94, No. 8, 2011, pp. 2562-2570.

T. H. Squire and J. Marschall, "Material Property Requirements for Analysis and Design of UHTC Components in Hypersonic Applications," *Journal of the European Ceramics Society*, Vol. 30, 2010, pp. 2239-2251.

J. Marschall and D. G. Fletcher, "High-Enthalpy Test Environments, Flow Modeling and in situ Diagnostics for Characterizing Ultra-High Temperature Ceramics," *Journal of the European Ceramics Society*, Vol. 30, 2010, pp. 2323-2336.

The following two publications were initiated under a previous AFOSR contract (FA9550-050-C-0020) and completed during this project:

J. Marschall, D. Pejaković, W. Fahrenholtz, G. Hilmas, S. Zhu, J. Ridge, D. G. Fletcher, C. O. Asma, O. Chazot, and J. Thömel, "Oxidation of ZrB₂-SiC Ultra-High Temperature Ceramic Composites in Dissociated Air," *Journal of Thermophysics and Heat Transfer*, Vol. 23, No. 2, 2009, pp. 267-278.

M. Playez, O. Chazot, D. G. Fletcher, J. Marschall, W. Fahrenholtz, G. Hilmas, and S. Zhu, "Optical Emission Spectroscopy During Plasmatron Testing of ZrB₂-SiC Ultra-High Temperature Ceramic Composites," *Journal of Thermophysics and Heat Transfer*, Vol. 23, No. 2, 2009, pp. 279-285.

INTERACTIONS/TRANSITIONS

SRI has established working scientific collaborations with research groups at the Missouri University of Science and Technology (Professors William Fahrenholtz, Gregory Hilmas), the Thermal Protection Materials and Systems Branch at NASA Ames Research Center (Matt Gasch, Sylvia Johnson, Don Ellerby, Jerry Ridge), the von Karman Institute for Fluid Dynamics in Belgium (Olivier Chazot, Francesco Panerai), and the University of Vermont (Doug Fletcher).

The results of this project have led to the following talks/presentations (presenting author is underlined):

M. Gasch, S. Johnson, and J. Marschall, "Oxidation Characterization of Hafnium-Based Ceramics Fabricated by Hot Pressing and Electric Field-Assisted Sintering," talk, 7th International Conference on High Temperature Ceramic Matrix Composites, Bayreuth, Germany, September 20-22, 2010.

L. Zhang, D. A. Pejaković, J. Marschall, and M. Gasch, "Thermal and Electrical Property Characterization of Diboride-Based UHTC Materials: Effects of Microstructure and Composition," poster, AFOSR Workshop on Aerospace Materials for Extreme Environments, St. Louis, MO, August 3-5, 2009.

S. Zhu, W. G. Fahrenholtz, G. E. Hilmas, J. Marschall, “Oxidation of ZrB₂-SiC Ceramics in Dissociated Air Plasma and Low Pressure Air Conditions,” poster, Materials Science & Technology Conference and Exposition, Pittsburgh, PA, October 5-9, 2008.

J. Marschall, “Testing and Modeling UHTC Materials in Dissociated Atmospheres,” keynote presentation, Ultra-High Temperature Ceramics: Materials for Extreme Environment Applications, Lake Tahoe, CA, August 3-8, 2008.

S. Zhu, W. G. Fahrenholtz, G. E. Hilmas, J. Marschall, D. G. Fletcher, C. O. Asma, “Characterization of ZrB₂-SiC Ceramics Tested by Plasma Stream Oxidation,” poster, 32th International Conference & Exposition on Advanced Ceramics and Composites, Daytona Beach, FL, January 27 – February 1, 2008.

DISCOVERIES/INVENTIONS/PATENTS

The research conducted to date under this grant has not generated any patents or inventions.

HONORS

None.

APPENDIX 1

Temperature Jump Phenomenon during Plasmatron Testing of ZrB₂-SiC Ultra-High Temperature Ceramics*

Jochen Marschall and Dušan A. Pejaković
SRI International, Menlo Park, California 94025, USA

William G. Fahrenholtz and Greg E. Hilmas
Missouri University of Science and Technology, Rolla, Missouri 65409, USA

Francesco Panerai and Olivier Chazot
von Karman Institute for Fluid Dynamics, Rhode-St-Genèse, 1640, Belgium

Abstract

The performance of ZrB₂-SiC ultra-high temperature ceramic composites in subsonic high-enthalpy dissociated air flows was investigated in the 1.2 MW Plasmatron facility at the von Karman Institute for Fluid Dynamics. Samples were sequentially exposed to low heat flux and high heat flux conditions during a single test run. Under certain high heat flux conditions, a rapid and spontaneous rise in sample surface temperature was observed under constant freestream conditions. The temperature jump seems associated with a transition in surface chemistry that leads to the loss of protective silica glass and substantially increases the chemical component of heat flux delivered to the surface.

Introduction

Ultra-high temperature ceramic (UHTC) composites of hafnium diboride (HfB₂) and zirconium diboride (ZrB₂) with a silica former, most commonly silicon carbide (SiC), have been studied extensively over the last decade as materials for leading edge and control surface components on hypersonic vehicles.¹⁻³ Such components experience extreme aerothermal heating in chemically aggressive, partially dissociated air environments. Promising aspects of diboride-based UHTC composites include the very high melting points of HfB₂ and ZrB₂ and their refractory oxides hafnia (HfO₂) and zirconia (ZrO₂), as well as the high thermal conductivities of HfB₂ and ZrB₂ that enables efficient heat conduction away from stagnation point regions.⁴ Because it is lighter and less expensive than HfB₂, ZrB₂ has some advantages as an aerospace material.

The oxidation of ZrB₂ produces both zirconia and boron oxide (B₂O₃). Significant oxidation of ZrB₂ in atmospheric air begins at about 1050 K. The softening temperature for amorphous

* This is an edited version of a manuscript submitted to the AIAA Journal of Thermophysics and Heat Transfer, August 2011.

B_2O_3 is in the range of 830 K to 900 K⁵; below about 1500 K the oxide scale consists of a porous ZrO_2 network filled with liquid B_2O_3 that acts as an effective oxygen diffusion barrier.⁶⁻⁷ However, the vapor pressure of B_2O_3 increases rapidly with temperature,⁸ resulting in rapid loss of B_2O_3 above 1500 K. The residual porous zirconia scale provides little resistance to inward oxygen transport and further oxidation,⁹⁻¹⁰ making the oxidation resistance of pure ZrB_2 insufficient for high-temperature hypersonic vehicle applications.

The addition of a silica former to ZrB_2 improves its oxidation resistance.¹¹⁻¹⁴ Compositions containing from 10 to 30% (by volume) SiC have generally been found to be optimal in this regard. The virgin $\text{ZrB}_2\text{-SiC}$ surfaces oxidize through parallel reactions that generate ZrO_2 , B_2O_3 and SiO_2 . Liquid B_2O_3 mixes with amorphous SiO_2 to form a borosilicate glass that seals the ZrO_2 scale.¹⁵ With increasing temperature, boron oxide evaporates preferentially from the surface, and the scale becomes silica rich. As the silica-rich oxide layer thickens, it limits the inward diffusion of oxygen to the virgin material below, slowing further oxidation.¹⁶ The oxidation rates of $\text{ZrB}_2\text{-SiC}$ materials up to ~1900 K at atmospheric pressure are generally proportional to the square root of time (i.e., parabolic kinetics) consistent with diffusion-limited oxidation.⁴

The melting/softening temperature of silica is much higher, and the vapor pressure is much lower than that of B_2O_3 . Nevertheless, as temperatures exceed ~1900 K, silica volatilization too becomes significant, again leaving an outer oxide scale of porous ZrO_2 . In this regime, oxidation proceeds by rapid, linear kinetics.¹⁷ Since one goal of UHTC research is to push the operating temperatures of leading edge and control surface components above 2273 K (2000°C), it is widely recognized that reliance on silica formers alone for oxidation protection is not feasible.¹⁸ A number of efforts are currently underway to enhance the oxidation protection properties of the ZrO_2 scale through non-Si-containing additives.¹⁹⁻²¹

A related issue with SiC -based high temperature composites is the transition between passive and active SiC oxidation.²² The transition occurs at threshold combinations of temperature and oxidant pressure at which the thermodynamically-favored oxidation reaction switches from one that produces condensed silica to one that produces gaseous silicon products or vice versa. Active-to-passive (AP) and passive-to-active (PA) oxidation transitions have been studied extensively for SiC ,²²⁻²⁸ as well as other silica formers including silicon^{23,29} and silicon nitride.^{27,30} Most experiments were performed in furnace environments in which temperature, pressure, flow speed, and gas composition are easily controlled and thermochemical equilibrium prevails. Very limited experimental results in partially dissociated air and oxygen seem to indicate that the boundary between passive and active SiC oxidation moves to lower oxygen pressures at a given temperature,³¹⁻³³ but results depend on the type of SiC used in the experiment.³²

The PA transition is clearly a concern for any high-temperature thermal protection system (TPS) containing a silica former and relying on silica for oxidation protection (and, hence, its stability and reusability). Passing through the PA boundary means accelerated mass loss, a changing outer mold line, and possible component failure. Because high-temperature TPS systems will encounter partially dissociated air in chemical non-equilibrium with the TPS

surface, the PA transition has been studied for a variety of carbon/silicon carbide (C/SiC) ceramic matrix composites in induction-coupled plasma (ICP)³⁴⁻³⁷ and arc-jet facilities.^{35-36,38} During these tests, spontaneous jumps in surface temperature of several hundred degrees Kelvin have been observed. These have been associated with passing through the PA boundary of SiC, although neither the kinetic details triggering the PA transition in dissociated oxygen and air, nor the sources of the additional heat flux necessary to explain the jump, are fully understood.

Recently Glass³⁹ suggested that Si-containing UHTC materials should also exhibit such temperature jumps, and cited as a possible example data collected during arc-jet tests at NASA Ames Research Center for the SHARP B-1 program as reported by Kolodziej et al.⁴⁰ In one instance, as a ZrB₂-SiC sample was heating up in the arc-jet stream, its surface temperature suddenly increased sharply from 3800°F to 4600°F (2360 K to 2810 K) over the course of about 15 seconds. This temperature jump was rationalized as resulting from the lower emittance and lower thermal conductivity of a rapidly forming oxide layer. Since this report, the results of numerous arc-jet and ICP test campaigns on UHTC composites containing a diboride and a silica former have been published, but, to our knowledge, none have clearly identified a similar spontaneous temperature jump.⁴¹⁻⁴⁷

This paper reports test results that demonstrate a temperature jump phenomenon when ZrB₂-SiC composites are exposed to certain high-temperature, low-pressure dissociated air environments. The tests were performed in the 1.2 MW Plasmatron facility at the von Karman Institute for Fluid Dynamics (VKI) on specimens manufactured by pressureless sintering at the Missouri University of Science and Technology (Missouri S&T). Specimens were sequentially exposed to low heat flux and high heat flux conditions during a single test run by adjusting the Plasmatron power. During some high heat flux conditions, we observed a rapid and spontaneous rise in sample surface temperature under constant freestream conditions. We associate this temperature jump with a transition in surface chemistry that leads to the loss of protective silica glass and substantially increases the chemical component of heat flux delivered to the surface. These tests provide the first set of experimental observations that characterize the temperature jump phenomenon in a diboride/silica former UHTC composite.

Materials and Characterization

A. Test Specimen Fabrication

Composites were prepared with the following target formulations: 1) ZrB₂ with 30 volume percent SiC; 2) (Zr,W)B₂ with 4 atomic percent tungsten substitution for zirconium; and 3) (Zr,W)B₂ with 4 atomic percent tungsten substitution and 30 volume percent SiC. These three compositions are referenced as ZrB₂-30SiC, (Zr,4W)B₂, and (Zr,4W)B₂-30SiC throughout this paper. Test specimens of these compositions are identified by 1.x, 2.x, and 3.x, respectively, where “x” is the sample number.

All composites were made from commercially available ZrB₂ powder (Grade B, H. C. Starck, Germany), which had a starting particle size of ~2 µm. ZrB₂-30SiC and (Zr,4W)B₂-30SiC materials also used SiC powder (Grade UF-10, H.C. Starck, Germany), which had a starting

particle size of $\sim 1 \mu\text{m}$; $(\text{Zr},4\text{W})\text{B}_2$ and $(\text{Zr},4\text{W})\text{B}_2\text{-}30\text{SiC}$ materials also used tungsten carbide (WC) powder (74R-0601, Infram, Manchester, Connecticut), which had a starting particle size $< 1 \mu\text{m}$. Particle sizes are as reported by the manufacturer. Superadditions of a combination of 2 wt% B_4C (Grade HS, H.C. Starck, Germany) and 1 wt% carbon derived by decomposition of phenolic resin (GP 2074, Georgia Pacific, Atlanta, Georgia) were used as sintering aids for all three compositions.

Powder batches were produced by dispersing ZrB_2 with SiC, WC, and/or B_4C in methyl ethyl ketone using a dispersant (BYK 110, BYK Chemie Co, Willingford, Connecticut). Batches were ball milled for 24 hours using WC media in a high-density polyethylene bottle. After 24 hours of milling, 1 wt% polypropylene carbonate binder (QPAC-40, Empower Materials, Newark, Delaware) and phenolic resin were added, and the slurries were ball milled for an additional 24 hours.

After milling, the slurries were dried, ground, and sieved (-50 mesh) to prepare for compaction. Powders were pressed into cylinders approximately 40 mm in diameter and 20 mm tall using a uniaxial compression pressure of 18.6 MPa. Next, the billets were cold isostatically pressed at 315 MPa. After compaction, the billets underwent binder burnout in an atmosphere of Ar-5% H_2 , and following binder burnout, they were machined using a WC tool on a standard metal working lathe to produce near net-shaped parts approximating the desired “mushroom-shaped” test specimens (Fig. 1a).

The near net shape specimens were then sintered according to the following schedule. Specimens were first heated at $10 \text{ }^\circ\text{C min}^{-1}$ from room temperature to $1250 \text{ }^\circ\text{C}$ under mild vacuum ($\sim 20 \text{ Pa}$). After holding at $1250 \text{ }^\circ\text{C}$ for 1 hour, specimens were heated at $10 \text{ }^\circ\text{C min}^{-1}$ to $1450 \text{ }^\circ\text{C}$ ($\text{ZrB}_2\text{-}30\text{SiC}$ and $(\text{Zr},4\text{W})\text{B}_2\text{-}30\text{SiC}$) or $1500 \text{ }^\circ\text{C}$ ($(\text{Zr},4\text{W})\text{B}_2$) and held for 1 hour. After the second hold, the atmosphere was switched to flowing argon at a nominal pressure of $\sim 10^5 \text{ Pa}$. Specimens were heated at $20 \text{ }^\circ\text{C min}^{-1}$ to the densification temperature and held there for 2 hours. The densification temperatures were $2000 \text{ }^\circ\text{C}$ for $\text{ZrB}_2\text{-}30\text{SiC}$ and $(\text{Zr},4\text{W})\text{B}_2\text{-}30\text{SiC}$ materials and $2075 \text{ }^\circ\text{C}$ for $(\text{Zr},4\text{W})\text{B}_2$. After the densification hold, specimens were cooled to room temperature at the natural furnace cooling rate ($\sim 20 \text{ }^\circ\text{C min}^{-1}$ on average).

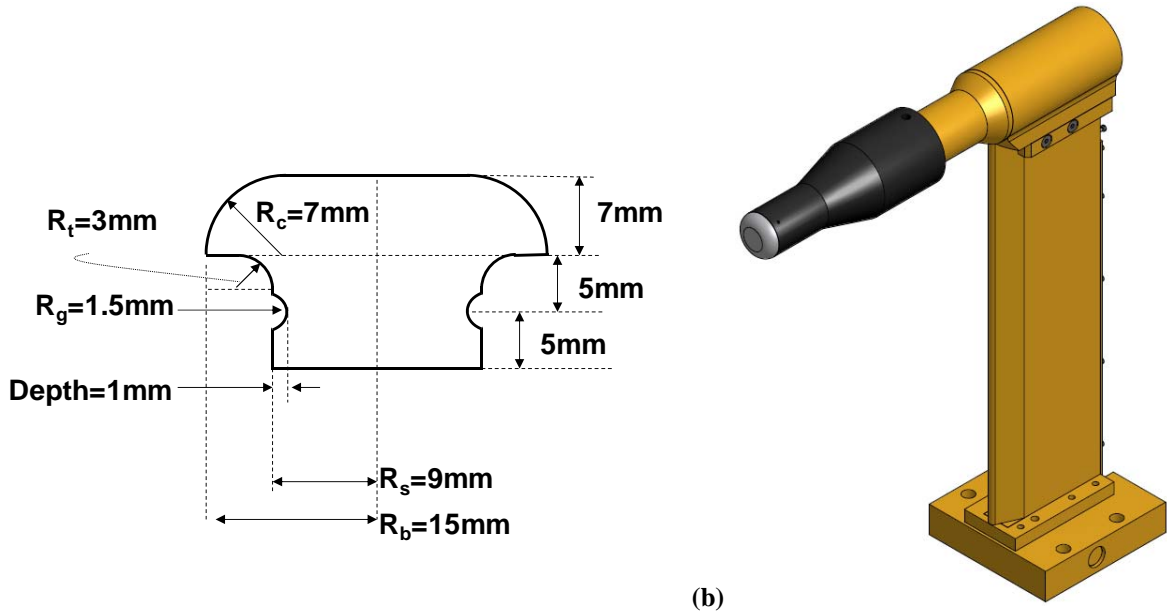


Fig. 1 (a) UHTC sample geometry; (b) stagnation point test configuration with sample, specimen holder, and sting arm.

The sintered ceramic specimens were fine-machined by a commercial vendor using diamond grinding (Bomas Machine Specialties, Somerville, Massachusetts) in an attempt to reach the target dimensions shown in Fig. 1a. While most dimensions could be achieved with good accuracy, it was not possible to maintain the 7 mm thickness of the “mushroom caps” for the majority of the specimens, resulting in thinner caps (by up to 2 mm) and larger flat face diameters (by up to 9 mm larger).

B. Specimen Characterization

The densities of the machined UHTC specimens were measured by the Archimedes method using a Mettler Toledo XP105 analytical balance with $\pm 0.01\text{ mg}$ accuracy. The average densities for the $\text{ZrB}_2\text{-30SiC}$, $(\text{Zr},4\text{W})\text{B}_2$, and $(\text{Zr},4\text{W})\text{B}_2\text{-30SiC}$ formulations were found to be $4.88 \pm 0.15\text{ g cm}^{-3}$, $5.72 \pm 0.28\text{ g cm}^{-3}$, and $4.75 \pm 0.21\text{ g cm}^{-3}$, respectively. Specimen mass changes were determined from pre- and post-plasma exposure mass measurements at VKI using an Adventurer SL precision balance with $\pm 0.1\text{ mg}$ accuracy.

Optical microscopy of post-test specimen surfaces was performed using a KEYENCE VHX-600 Digital Microscope (Itasca, Illinois). Post-test specimen surface composition was assessed with energy dispersive X-ray spectroscopy (EDS) instrumentation (EDAX, Mahwah, New Jersey) integrated into a field-emission scanning electron microscope (JEOL 6100, JEOL, Ltd. Tokyo, Japan). Crystal structure was determined by X-ray diffraction (XRD) using a Phillips apparatus (New York, New York) with a $\text{CuK}\alpha$ source and a Ge monochromator. Elemental analysis of the oxide scale was performed by a commercial analytic laboratory (ATI Wah Chang, Albany, Oregon).

Plasmatron Testing Setup and Procedures

Air plasma exposure experiments were performed in the 1.2 MW Plasmatron facility at VKI.⁴⁸⁻⁴⁹ A solid-state power supply (400 kHz, 1.2 MW, 2 kV) was used to generate a high enthalpy subsonic gas flow by inductive coupling in a 160 mm diameter plasma torch. The energetic gas stream was directed into a large vacuum chamber, where test specimens and diagnostic probes for the dynamic pressure, P_{dyn} , and the cold-wall heat flux, q_{cw} , could be swung into and out of the flow on three separate water-cooled sting arms. The distance between the torch exit and the specimen or probe face was 44.5 cm.

Test specimens were mounted in graphite holders attached to a water-cooled sting-arm, as shown in Fig. 1b. Specimens were held in place with pins that captured the grooves on the specimen stems (Fig. 1a.) In this campaign, the Plasmatron was always operated with an air mass flow rate of 16 g s⁻¹ and a static chamber pressure of 10 kPa. The freestream enthalpy was varied over the range of about 10 to 28 MJ kg⁻¹ by adjusting the Plasmatron power from 170 to 390 kW.

The cold-wall stagnation point heat flux was measured using a water-cooled copper calorimeter installed flush with the surface of a water-cooled copper probe. Both the calorimeter and probe had polished surfaces. Heat flux values were determined from the temperature change and mass flow rate of the water used to cool the calorimeter. Two heat flux probes of different size and external shape were used during the course of these experiments. One probe was geometrically similar to the test specimen (flat-faced cylinder, 30 mm body diameter and 7 mm corner radius) so that the flow environment around the specimen was closely reproduced. Unfortunately, this probe was damaged early in the campaign and a second larger probe having the standard European Space Agency (ESA) stagnation point test specimen geometry was used instead (flat-faced cylinder, 50 mm body diameter, 11 mm corner radius).

Cold-wall heat flux measurements serve two purposes: i) they are used to characterize and reproduce heating conditions between different test runs; and ii) they enable the rebuilding of boundary layer edge conditions and the estimation of gas composition at the specimen surface using computational fluid dynamics (CFD) codes. Probe geometry is not critical in the first application, in which only measurement consistency is important. However, probe geometry has a large influence in the second application because aeroconvective heating rates are strongly affected by probe shape and dimensions. In the present instance, the large probe experiences a lower cold-wall heat flux than the small probe for the same Plasmatron freestream conditions because of differences in the boundary layer thickness and the velocity gradient as the flow approaches the probe surface. The thermal and dynamic boundary layers are thicker and the velocity gradient is smaller for the large versus the small probe.

Additional tests comparing heat flux measurements with the two different probes were carried out after the UHTC test campaign concluded. These tests were performed by swinging the two calorimeter probes mounted on separate sting arms into the flow consecutively, at the same static pressure, the same air mass flow rate, and over the same range of Plasmatron powers as employed in the UHTC tests. The resulting data are shown in Fig. 2. The linear correlation

established by these measurements, $q_{cw} = 1.69q_{cw,lp} - 17.32$, enabled conversion of the cold-wall heat fluxes measured with the large probe to values appropriate for the small probe (and thus to the UHTC sample geometry.) Both heat flux measurements should agree at zero heat flux, and a linear correlation with a zero intercept could also be used to fit the data. However, in the absence of measurements at lower heat fluxes, the suitability of a linear fit over the entire range extending to zero cannot be confirmed, and it is safer to limit the correlation to the range used in our tests.

The test chamber was fitted with several windows to allow for optical diagnostics, including two-color and wide-band infrared radiometry of the sample surface, and emission spectroscopy of the gas in front of the sample. In addition, tests were also documented by different combinations of digital photography and videography.

A two-color radiometer (Marathon Series MR1SC, Raytek Corp., Santa Cruz, California) was used to record sample surface temperatures at a rate of 1 Hz. The radiometer measures temperatures in the range 1000 to 3000 °C, using two overlapping infrared wavelength bands at 0.8–1.1 and 1.0–1.1 μm. Thermal emission was collected through a quartz window at an angle of ~35 degrees relative to the surface normal, from an elliptical region centered on the specimen stagnation point (major axes: ~5.6 mm; minor axis ~4.6 mm). The radiometer was previously calibrated with the same window in place using a black-body radiation source (LANDCAL R1500T, Land Instruments International, Dronfield, United Kingdom); temperature measurements are believed to be accurate to ± 10 °C.

A broadband infrared radiometer (KT19.XX, Heitronics Infrarot Messtechnik GmbH, Wiesbaden, Germany) with a temperature range of 0 to 3000 °C was used to collect thermal emission from the sample surface over the 0.6–39 μm wavelength range. Thermal emission

measurements were recorded at a frequency of 1 Hz. Emission was collected through a KRS5 window at ~47 degrees relative to the surface normal from an elliptical region centered on the stagnation point (major axes: ~14.8 mm; minor axis ~10.1 mm). The broadband radiometer was calibrated with the KSR5 window in place using the same blackbody source as the two-color radiometer.

With this geometric arrangement of the two radiometers, and with their respective fields of view, the emitting area seen by the two-color radiometer lies within the area seen by the broadband radiometer, which in turn lies completely on the flat face of the sample away from the rounded edges.

Tests were filmed with a high-definition

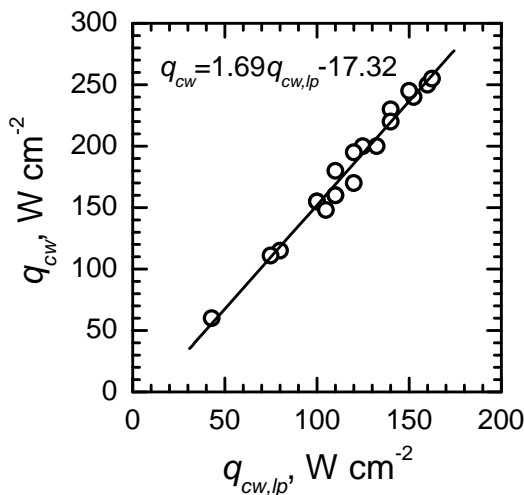


Fig. 2. Cold-wall heat flux probe measurement comparison; data and linear correlation.

digital dual camera (VPC-GH1, Sanyo Europe Ltd., Watford, United Kingdom). The camera was positioned to view the sample through a quartz window \sim 35 degrees off the surface normal. The camera has a 1920 by 1080 C-MOS sensor, a double range focal lens, and a video shutter speed that ranges from 1/30 to 1/10000 seconds.

Gas-phase emission spectrometry was performed through a quartz window viewing the test specimen and impinging gas flow from the side. Emission was collected through a variable aperture, and focused by a 300 mm focal length converging quartz lens into a 600 μm diameter optical fiber leading to a spectrometer with a 200–1100 nm wavelength range (HR-4000, Ocean Optics, Dunedin, Florida.) Spectra were recorded at 1 Hz with spectral resolution ranging from 0.27 nm to 0.23 nm. The optical axis of the collection system was aligned parallel to the sample surface at its stagnation point, with the \sim 0.5 mm diameter emission collection volume about 2 mm in front of the surface. A relative intensity calibration of the system was performed with a deuterium lamp in the ultraviolet range (< 400 nm) and with a ribbon tungsten lamp in the visible (> 400 nm). The estimated relative uncertainty of the total integrated emission of the radiative signature is less than 10%.

Computation

Computational fluid dynamics simulations of the plasma freestream and the boundary layer around the specimen and holder were used to rebuild the boundary layer edge conditions and to compute the gas composition and the catalytic component of heating at the specimen surface. The VKI Boundary Layer Code solves the boundary layer equations for a two-dimensional, steady, laminar flow of chemically reacting gas over a catalytic surface, including chemical non-equilibrium.⁵⁰⁻⁵¹ The VKI ICP Code computes the Plasmatron magnetohydrodynamic field (plasma torch plus vacuum chamber) under local thermodynamic equilibrium and provides nondimensional parameters that characterize the boundary layer over the test article.⁵²⁻⁵³ Both codes use the PEGASE library to obtain thermodynamic and transport properties of the gas mixture.⁵⁴

The total heat flux experienced by a material in the Plasmatron stream has both convective and chemical components: $q_w = q_{\text{conv}} + q_{\text{chem}}$. Convective heating arises from the large temperature difference between the hot boundary layer gases and the cooler specimen surface, while chemical heating results from exothermic reactions on the specimen surface such as catalytic recombination and oxidation. The Boundary Layer Code computes the chemical component of heat flux assuming the two independent catalytic surface reactions, $\text{O} + \text{O} \rightarrow \text{O}_2$ and $\text{N} + \text{N} \rightarrow \text{N}_2$, and restricts them to have the same recombination efficiency with complete accommodation of the exothermic recombination energy. The recombination efficiency, γ , is defined as the fraction of atom collisions with the surface that result in atom loss. The maximum chemical heating component is computed with $\gamma = 1$ and the minimum ($q_{\text{chem}} = 0$) with $\gamma = 0$.

Under steady-state conditions, the input heat flux is balanced by radiative energy loss from the surface to the environment and by heat conduction into the interior: $q_w = q_{\text{rad}} + q_{\text{cond}}$. During calorimeter measurements, water cooling keeps the surface temperature low making q_{rad}

negligible, and the cold-wall heat flux is measured: $q_{cw} = q_{cond}$. During specimen tests, the surface reaches a high steady-state temperature and the hot-wall heat flux is approximately $q_{hw} \approx q_{rad}$, where it is presumed that q_{cond} is much smaller than q_{rad} . The radiative flux is computed from the radiance measured by the broadband radiometer, or equivalently from the measured surface temperature, T_w , as $q_{rad} = \varepsilon\sigma T_w^4$, where σ is the Stefan-Boltzmann constant and ε is the total hemispherical emittance of the surface derived from the two-color and broadband radiometer measurements, as detailed in Section V below.

The Boundary Layer Code and the ICP Code were used together to rebuild the flow conditions at the boundary layer edge. First, the non-dimensional boundary layer parameters were computed by the ICP Code for each test condition – mass flow rate, static pressure, and power coupled into the gas - given the geometries of the 30 mm probe and the Plasmatron facility. With the assumption of local thermodynamic equilibrium at the boundary layer edge, the computed non-dimensional parameters then served as inputs to the Boundary Layer Code. A five-species model of dissociated air (O, O₂, N, N₂, and NO) and the gas-phase reaction rates of Dunn and Kang⁵⁵ were used. The copper calorimeter was assigned a catalytic recombination efficiency of 0.01 and a surface temperature of 350 K. The Boundary Layer Code was iterated over the boundary layer edge temperature until the numerical and experimental cold-wall heat fluxes matched. The final outputs of this procedure were the five species concentrations, the temperature, T_e , the velocity, V_e , and the enthalpy, H_e at the boundary layer edge.

Once the edge conditions were determined, the Boundary Layer Code was used to compute an abacus of heat flux vs. surface temperature for different values of recombination efficiency. For each point on the abacus, the Boundary Layer Code concurrently computes the gas-phase concentrations of O, O₂, N, N₂, and NO in contact with the hot wall at the stagnation point. The intersection of the measured surface temperature and hot-wall heat flux on this abacus identified the recombination efficiency necessary to reproduce the experiment,⁵⁶ and the particular CFD solution used to estimate the composition of the gas impinging on the specimen surface.

Experimental Results

A. Observation of the Temperature Jump Phenomenon

Figure 3 shows the surface temperature histories measured by the two-color radiometer during Plasmatron testing of the various UHTC specimens. Tests were performed by inserting the specimen into the flow at a low Plasmatron power setting, letting the sample temperature equilibrate for a given time (typically 5.5 minutes), then increasing the power and holding at the new heating condition for an additional length of time (typically 2 to 4.5 minutes). Tests were terminated by either shutting off the torch or removing the specimen from the flow; the former method produces the gradual temperature decays seen in Fig. 3. The dynamic pressures and the cold-wall heat fluxes were measured at the low-power and high-power settings during each test prior to sample insertion. Table 1 lists the Plasmatron powers, the measured cold-wall heat flux and dynamic pressure (rounded to the nearest 5 Pa) and the derived boundary layer edge conditions for each test. The Plasmatron powers listed correspond to an approximate value

determined from an image of the full power delivered by the high frequency generator; the power transferred into the gas stream is lower.

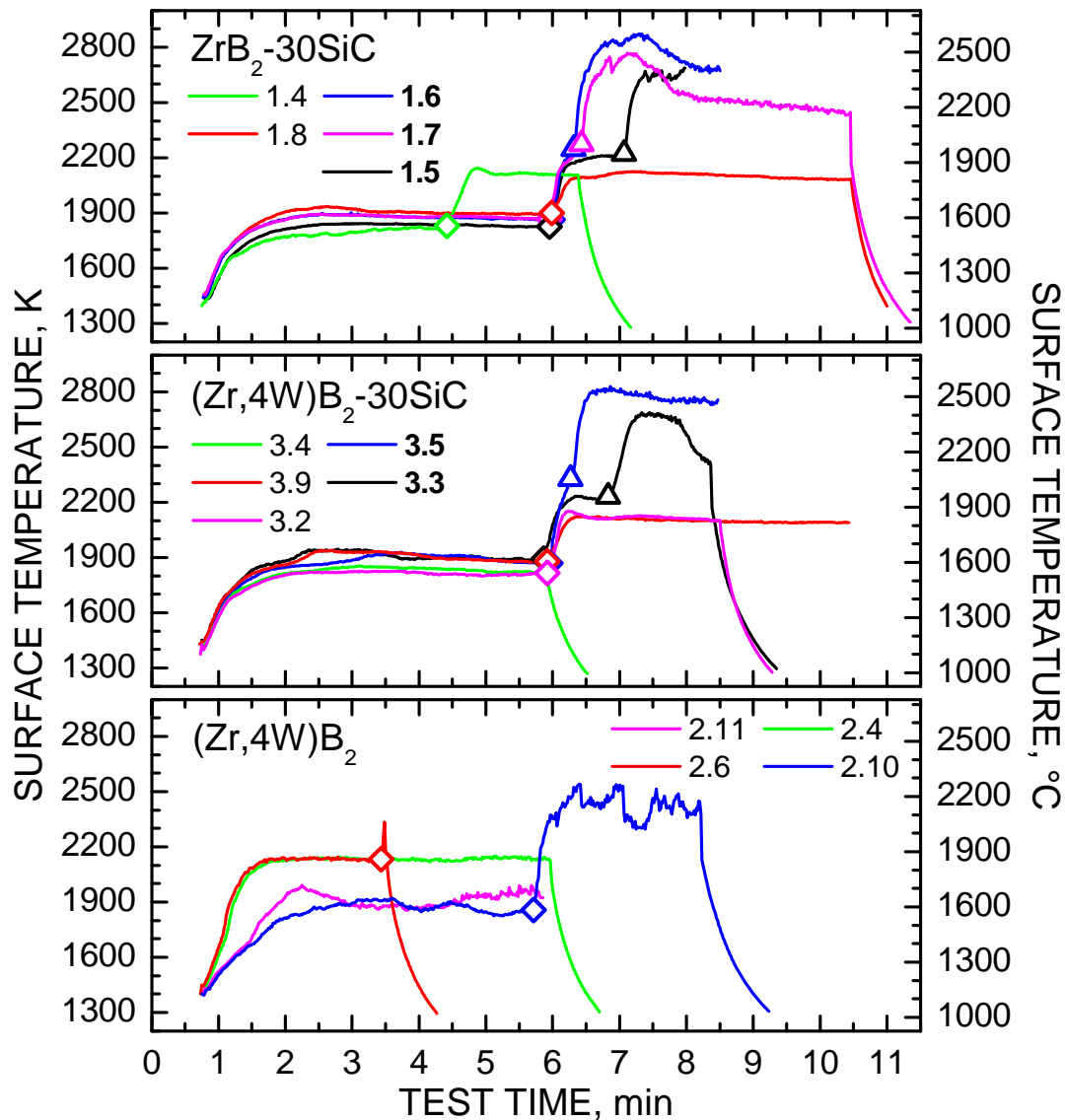


Fig. 3. Surface temperatures measured during Plasmatron testing of ZrB_2 -30SiC (top panel), $(\text{Zr},4\text{W})\text{B}_2$ -30SiC (middle panel), and $(\text{Zr},4\text{W})\text{B}_2$ (bottom panel) UHTC specimens. Open diamonds indicate when the Plasmatron power was increased and open triangles indicate the onset of spontaneous surface temperature jumps. Specimens that underwent a temperature jump are identified in bold text in the figure legends.

Table 1 Plasmatron operating conditions.*

Sample [‡]	Power, kW	q_{cw} , W cm ⁻²	P_{dyn} , Pa	H_e , kJ g ⁻¹	T_e , K	V_e , m s ⁻¹
1.4	180	108 [†]	25	12.2	5048	92
	290	185 [†]	60	17.7	5656	159
1.5	200	109	30	12.0	5003	100
	353	202[†]	75	18.6	5731	180
1.6	205	109	30	12.0	5003	100
	387	236	90	21.7	5944	207
1.7	210	108	25	12.2	5048	92
	370	219	80	20.3	5849	191
1.8	212	109	30	12.0	5003	100
	292	185	60	17.7	5656	159
1.9	200	111	30	12.2	5034	101
2.4	195	111	30	12.2	5034	101
2.6	198	111	30	12.2	5034	101
	330	245	90	22.9	6015	210
2.10	172	57	20	7.2	3464	65
	261	152	45	15.1	5427	131
2.11	170	54	20	6.9	3380	64
3.2	195	109	30	12.0	5003	100
	310	194 [†]	70	18.0	5681	172
3.3	224	111	30	12.2	5034	101
	339	202	75	18.6	5731	180
3.4	172	111	30	12.2	5034	101
3.5	203	111	30	12.2	5034	101
	402	253	95	23.5	6055	218
3.9	211	109	30	12.0	5003	100
	295	185	60	17.7	5656	159

* $P_{stat} = 10^4$ Pa and $\dot{m} = 16$ g s⁻¹ for all tests; [†] Estimated based on similar tests;

[‡]Samples that underwent a temperature jump are indicated in bold text.

Upon sample insertion, the surface temperature rises and reaches a relatively steady value determined by the energy balance between the hot-wall heat flux to the specimen, heat conduction losses into the interior, and radiation to the environment. The low power setting for

the majority of tests was adjusted to produce a cold-wall heat flux of $\sim 110 \text{ W cm}^{-2}$. Under these conditions all $\text{ZrB}_2\text{-}30\text{SiC}$ and $(\text{Zr},4\text{W})\text{B}_2\text{-}30\text{SiC}$ specimens reached steady surface temperatures between 1800 and 1900 K. The $(\text{Zr},4\text{W})\text{B}_2$ material reached a considerably higher surface temperature of about 2130 K under these same test conditions (specimens 2.4 and 2.6 in Fig. 3.)

Additional tests were run on samples 2.10 and 2.11 with the low-power setting decreased to produce a cold-wall heat flux near 55 W cm^{-2} . This lower heating condition resulted in surface temperatures similar to those observed for the $\text{ZrB}_2\text{-}30\text{SiC}$ and $(\text{Zr},4\text{W})\text{B}_2\text{-}30\text{SiC}$ materials at 110 W cm^{-1} . The lower surface temperatures experienced by the SiC-containing materials versus the $(\text{Zr},4\text{W})\text{B}_2$ specimens are likely due to the development of a silica-rich oxide scale covering the ZrO_2 formed during testing, which retards the rate of oxidation. Additionally, silica surfaces are known to have relatively low catalytic efficiencies for oxygen recombination⁵⁷ compared to zirconia surfaces,⁵⁸ and so will experience lower chemical heating contributions to the heat flux for a given freestream condition.

The transition between the low-power and high-power settings during each test run is indicated in Fig. 3 by open diamonds on the temperature traces. An increase in Plasmatron power leads to an increased cold-wall heat flux (Table 1), and is expected to correspondingly increase the hot-wall heat flux to the specimen and drive its surface temperature to a higher steady-state value. Examples of this anticipated behavior are seen for samples 1.4, 1.8, 3.2, and 3.9, where the high-power setting has been adjusted to produce cold-wall heat flux of $\sim 185 \text{ W cm}^{-2}$ and all four specimens settle to a steady-state surface temperature near 2110 K. Similar behavior is seen for sample 2.10 when the cold-wall heat flux is raised from 57 to 152 W cm^{-2} . Although the temperature measurement shows large fluctuations, it varies around a mean steady-state temperature of about 2400 K under the higher power conditions.

However, five of the SiC-containing specimens – 1.5, 1.6, 1.7, 3.3 and 3.5 – showed a very different behavior. In addition to the temperature rise expected from the increased Plasmatron power, each specimen underwent a further spontaneous surface temperature jump of several hundred degrees. The times at which these temperature jumps initiated are indicated by open triangles on the temperature plots of Fig. 3. Because these temperature jumps occurred under constant Plasmatron operating conditions, they must be associated with a changing energy balance at the surface, not an increase in the freestream enthalpy.

Figure 4 provides an expanded view of the temperature jump region for the two different SiC-containing formulations; two specimens have been removed from each panel for clarity. The cold-wall heat flux for samples 1.5 and 3.3 under the high-power setting was $\sim 202 \text{ W cm}^{-2}$, just 17 W cm^{-2} higher than for samples 1.8 and 3.9. Figure 4 shows that both samples 1.5 and 3.3 approached a new steady-state surface temperature near 2215 K to accommodate this higher heat input. Then, after about 30 to 45 seconds at this temperature, the surface temperature rose sharply by over 400 K within a period of 20 to 30 seconds.

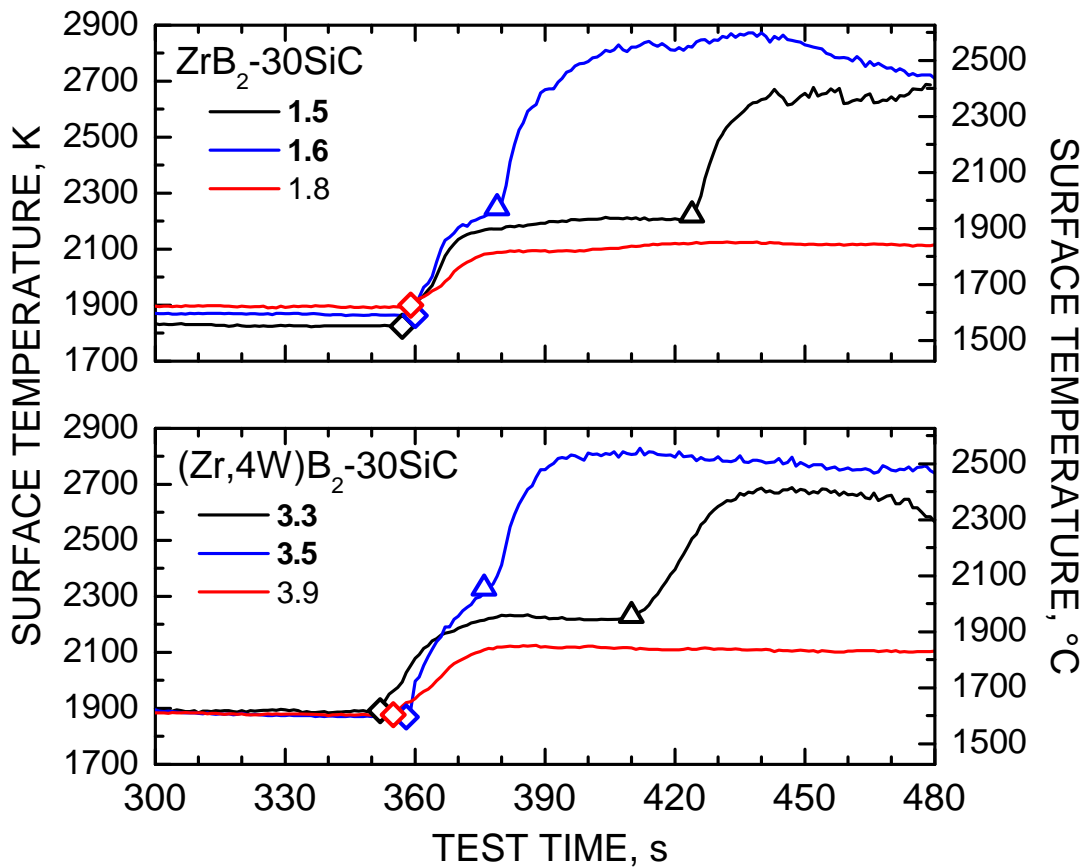


Fig. 4. Surface temperatures in the temperature jump region measured during Plasmatron testing of $\text{ZrB}_2\text{-}30\text{SiC}$ specimens 1.5, 1.6, and 1.8 (top panel) and $(\text{Zr},4\text{W})\text{B}_2\text{-}30\text{SiC}$ specimens 3.3, 3.5, and 3.9 (bottom panel).

Similar behavior is seen for samples 1.6 and 3.5, but with the temperature jump occurring sooner after the switch to high-power conditions. For specimens 1.6 and 3.5, the high-power settings produced cold-wall heat fluxes of 236 and 253 W cm^{-2} , respectively, compared to the $\sim 202 \text{ W cm}^{-2}$ experienced by specimens 1.5 and 3.3. These higher heating conditions cause the temperatures of specimens 1.6 and 3.5 to rise more rapidly to higher levels, and the time to trigger the spontaneous temperature jump is shortened.

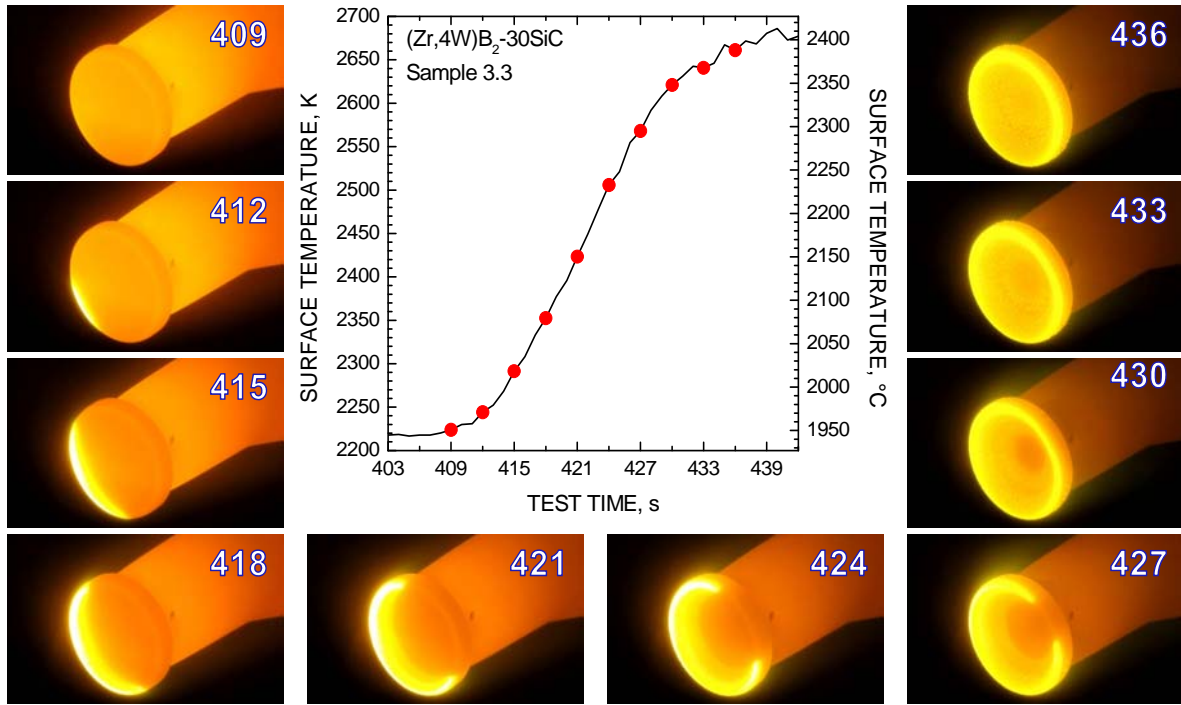


Fig. 5. Still images of the temperature jump on the surface of (Zr,4W) B₂-30SiC specimen 3.3. Images are 3 seconds apart; the measured surface temperatures corresponding to the image times are indicated by red symbols on the plot.

The temperature jump phenomenon was visually evident during testing as a large increase in light emission from the sample surface. Figure 5 shows still images taken from a video of sample 3.3 showing the progression of the temperature jump over the surface. The heat flux is largest near the edges of the test specimen because of the abrupt acceleration of the flow around the specimen, which thins the boundary layer in this region.⁵⁹ The temperature jump initiates on the lower left-hand edge of the specimen and progresses around the edge in both directions, completely encircling the specimen after about 18 seconds and encompassing the entire surface after about 24 seconds. This same progression was observed for the other four specimens that underwent a surface temperature jump, although the times to complete the transition varied.

Note that the camera was in automatic mode, continuously adjusting to accommodate the increased intensity radiating from the sample surface. Thus, the contrast in brightness within each image is a better indication of temperature differences than comparisons of brightness between different images. Since temperature is measured at the center of the specimen face by the two-color pyrometer, the temperature at the specimen edge as the transition progresses is likely higher than the value plotted in Fig. 5.

B. Surface Oxidation

Figure 6 shows post-test optical micrographs of the ZrB_2 -30SiC specimens 1.9, 1.8, 1.5, and 1.6 and $(\text{Zr},4\text{W})\text{B}_2$ -30SiC specimens 3.4, 3.9, 3.3, and 3.5. Samples 1.9 and 3.4 were exposed to low-power conditions only and experienced maximum surface temperatures below 1900 K. Both specimens are blackish in color and have a smooth, shiny surface. Samples 1.8 and 3.9 were exposed to high-power conditions, reaching surface temperatures near 2100 K, but did not undergo a temperature jump. The appearance of their surfaces is very similar to samples 1.9 and 3.4, still relatively smooth, but more grayish in color. Samples 1.5 and 3.3 experienced the temperature jump phenomenon, as have samples 1.6 and 3.5; however the former specimens spent less time at a lower post-jump surface temperature. The specimen surfaces are whitish and rougher, especially around the periphery. The peripheral whitish scale of sample 1.7 became detached after testing. Poor adherence and decreased thermal contact of this peripheral scale to the underlying material may contribute to the higher temperatures at the sample edge after the temperature jump (as indicated by the images in Fig. 5).

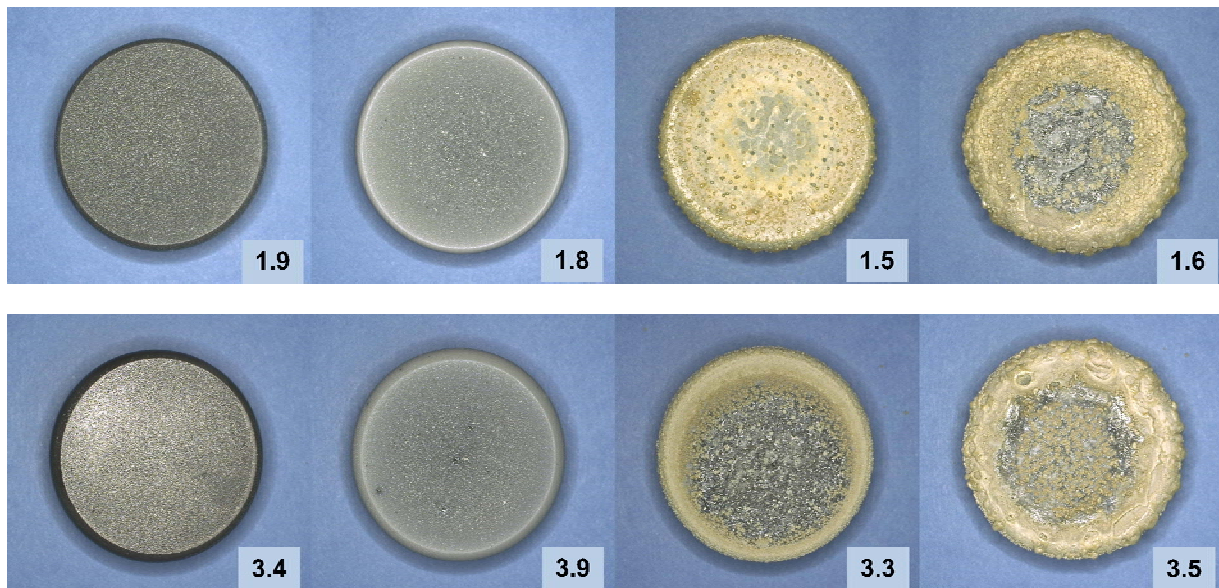


Fig. 6. Optical micrographs of ZrB_2 -30SiC (top panel) and $(\text{Zr},4\text{W})\text{B}_2$ -30SiC (bottom panel) specimens after Plasmatron testing; the specimen diameter is 30 mm.

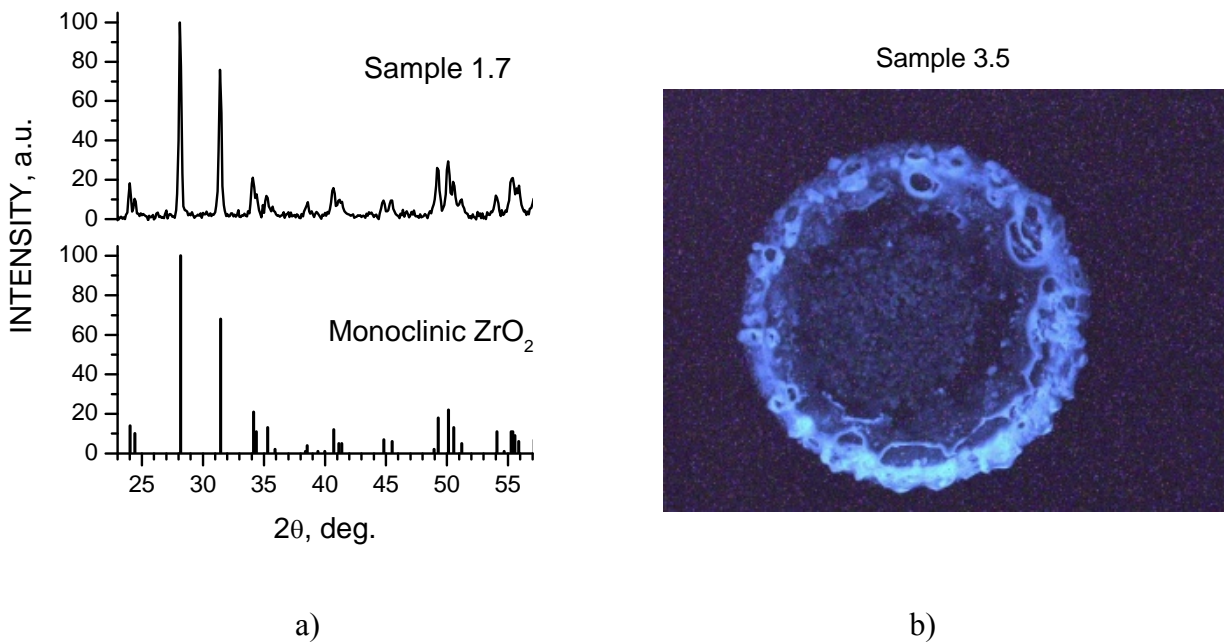


Fig. 7. a) XRD spectrum of the rim of sample 1.7 showing the crystal structure of monoclinic ZrO₂; **b)** phosphorescence of sample 3.5 after exposure to ultraviolet light from a mercury vapor pen light indicating the presence of ZrO₂.

Portions of scale detached from sample 1.7 were used for XRD analysis and elemental analysis for Zr, O, and Si at ATI Wah Chang. XRD analysis confirmed that the whitish scale contains monoclinic zirconia (Fig. 7a), and the elemental composition reported by ATI Wah Chang is consistent with ZrO₂ and residual Si at the 2900 parts-per-million level by mass. The presence of zirconia was also indicated by the observation of phosphorescence after ultraviolet light illumination (Fig. 7b). Phosphorescence is a known property of both ZrO₂⁶⁰⁻⁶¹ and HfO₂.⁶² Finally, EDS analysis showed the presence of Zr, O, and Si in various relative amounts in different regions of the surface.

These analyses indicate that after the temperature jump, the rougher, whitish peripheral oxide scale is mainly composed of ZrO₂ with only minor silica remnants, whereas the oxide scale covering the sample interior is smoother containing ZrO₂ islands in a glassy background. The zirconia rich oxide scale on the sample periphery correlates with the region experiencing the highest aerothermal heating⁵⁹ and the location where the temperature jump begins and propagates (see Fig. 5).

C. Emittance

One possible driving force for the temperature jump is that rapid surface oxidation changes the composition and morphology of the surface in such a way that it lowers the emittance substantially. With a lower emittance, a higher temperature is required to maintain the steady-state energy balance at the surface. The required change in the total hemispherical emittance that

would be necessary to explain the observed temperature jumps for samples 1.5 and 3.3 can be estimated from the expression;

$$\varepsilon_H = [T_L/T_H]^4 \varepsilon_L , \quad (1)$$

where the subscripts L and H indicate values before and after the temperature jump. Equation (1) is derived from the surface energy balance by assuming that the surface heat flux and the conduction losses into the interior are constant: $q_{hw} = \varepsilon_L \sigma T_L^4 + q_{cond} = \varepsilon_H \sigma T_H^4 + q_{cond}$. Plugging in representative temperatures ($T_L = 2206$ K and $T_H = 2642$ K for sample 1.5), we find $\varepsilon_H = 0.49 \varepsilon_L$, indicating that the emittance must decrease by a factor of ~ 2 if it is to account for the observed temperature jump.

While it is not possible to measure the total hemispherical emittance *in situ*, changes in the average directional emittance (over the 0.6-39 μm wavelength range, 47° off the surface normal) can be followed by combining the data of the two-color and the broadband radiometers. This average directional emittance is defined by

$$\varepsilon(T, \Delta\lambda_{0.6-39}, 47^\circ) = \frac{L'_{0.6-39}}{L_{0.6-39}} = \frac{\int_{0.6}^{39} \varepsilon(T, \lambda, 47^\circ) E_b(T, \lambda) d\lambda}{\int_{0.6}^{39} E_b(T, \lambda) d\lambda} , \quad (2)$$

where $L'_{0.6-39}$ is the measured radiance, $L_{0.6-39}$ is the ideal blackbody radiance, and $E_b(T, \lambda)$ is the Planck blackbody function. The broadband radiometer provides a direct measurement of $L'_{0.6-39}$, while $L_{0.6-39}$ is computed by integrating the Planck function over the 0.6-39 μm wavelength range at the surface temperature measured by the two-color radiometer.

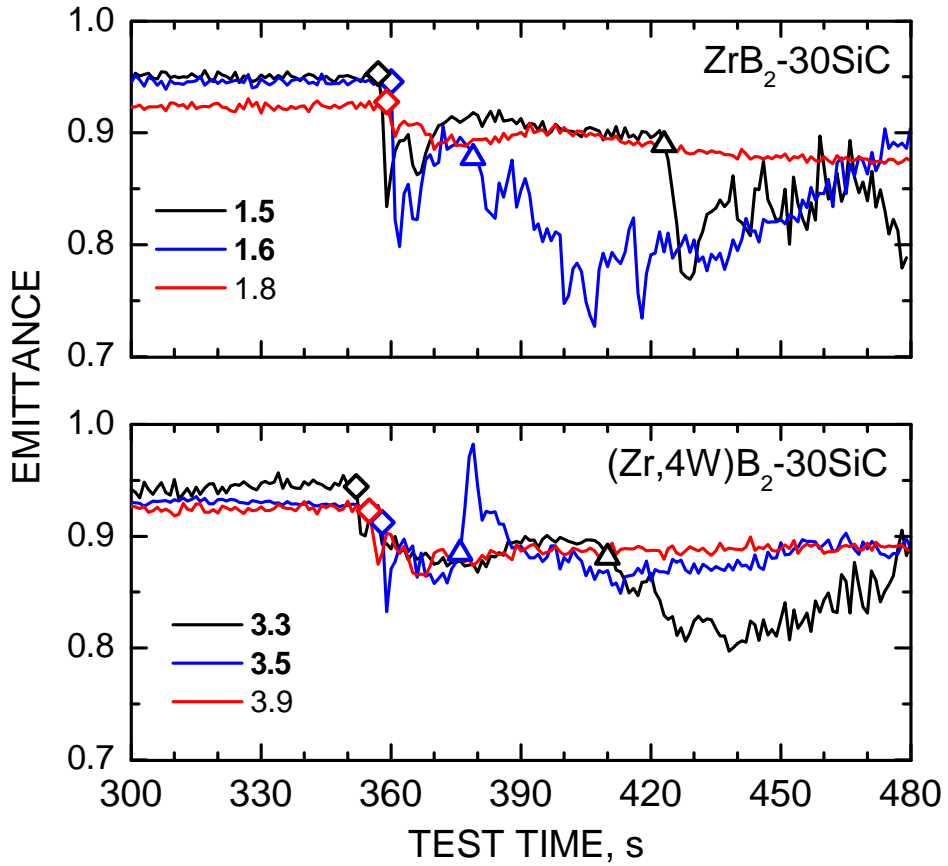


Fig. 8. Directional emittance in the temperature jump region measured during Plasmatron testing of $\text{ZrB}_2\text{-}30\text{SiC}$ specimens 1.5, 1.6, and 1.8 (top panel) and $(\text{Zr},4\text{W})\text{B}_2\text{-}30\text{SiC}$ specimens 3.3, 3.5, and 3.9 (bottom panel).

The 0.6-39 μm wavelength range contains more than 96% of the total emissive power for any surface temperature in the 1000-3000 K range, therefore $L'_{0.6-39}$ and $L_{0.6-39}$ are very good approximations for total spectral values. For dielectric surfaces (e.g., oxides) with refractive indices between 1 and 4, electromagnetic theory predicts differences of no more than $\sim 5\%$ between hemispherical and normal emittance, and between normal emittance and any directional emittance less than 50 degrees off-normal.⁶³ While surface roughness may cause deviations from these predictions, the measured average directional values are still the best approximations currently available for the total hemispherical emittance of the UHTC specimens during testing.

Figure 8 shows the directional emittance derived in the above manner for the same specimens and test time interval as in Fig. 4. The emittance prior to switching to the high-power condition is very high, between 0.9 and 0.95 for all specimens. Such high emittances are consistent with estimates made by Monteverde and Savino during arc-jet testing of $\text{ZrB}_2\text{-}15\text{SiC}$ materials using a similar technique,⁴¹ as well as reflectance measurements performed on $\text{ZrB}_2\text{-}30\text{SiC}$ specimens after Plasmatron tests in which sample temperatures remained below 1900 K.⁴⁶ After the switch

Table 2 Initial specimen mass and mass change.

Sample	m_i , g	Δm , g
1.4	32.485	-0.040
1.5	33.003	-0.742
1.6	33.097	-1.518
1.7	33.310	-1.046
1.8	32.762	-0.043
1.9	32.759	+0.010
2.4	39.773	+0.125
2.6	39.281	-0.616
2.10	41.692	-0.418
2.11	41.594	+0.053
3.2	34.669	-0.020
3.3	34.623	-0.503
3.4	33.970	+0.021
3.5	33.540	-0.801
3.9	33.507	-0.018

to high power, the emittance settles to a slightly lower value between 0.85 and 0.9 for specimens 1.8 and 3.9, which did not undergo a temperature jump.

For specimens 1.5 and 3.3, the emittance stabilizes near 0.9 after the switch to high power and before the temperature jump. After the temperature jump, the emittance decreases and shows greater fluctuation, however it never falls below 0.75, and for the most part remains higher than 0.8. This result argues strongly against decreasing emittance as the driving force for the temperature jump phenomenon, since a much lower post-jump emittance would be required; i.e., $\varepsilon_H = 0.49 \times 0.9 = 0.44$. Similar conclusions can be drawn from the pre- and post-jump emittances of samples 1.6 and 3.5.

D. Mass Changes

The changes in sample mass after Plasmatron testing are listed in Table 2. Most specimens lost mass, but several gained mass, most prominently, samples 2.4 and 2.11.

The oxidation of ZrB_2 to ZrO_2 and B_2O_3 results in mass increases of 70% if both oxides remain and of 9.2% if B_2O_3 completely volatilizes. The oxidation of $(\text{Zr},4\text{W})\text{B}_2$ to ZrO_2 , WO_3 , and B_2O_3 results in mass increases of 69% if all oxides remain, 9.5% if all B_2O_3 volatilizes, and 1.5% if both WO_3 and B_2O_3 volatilize. The observed positive mass change for samples 2.4 and 2.11 (which reached temperatures of ~ 2130 K and ~ 1990 K, respectively) is consistent with oxidation experiments performed on the same $(\text{Zr},4\text{W})\text{B}_2$ composition in air at 1873 K.¹⁹⁻²⁰ The large mass loss observed for specimens 2.6 and 2.10 cannot be accounted for by oxide volatilization alone and must be due to the mechanical loss of oxide scale (i.e., spallation of ZrO_2) under more aggressive heating conditions.

The oxidation of $\text{ZrB}_2\text{-}30\text{SiC}$ to ZrO_2 , SiO_2 , B_2O_3 , and CO(gas) results in a mass change of +67% if all oxides remain, +16.5% if all B_2O_3 volatilizes, and -10.5% if both SiO_2 and B_2O_3 volatilize. Thus an oxidation-driven net mass loss can occur with sufficient volatilization of the silica rich oxide scale at high temperatures. Similar behavior is calculated for the $(\text{Zr},4\text{W})\text{B}_2\text{-}30\text{SiC}$ composition.

The SiC-containing specimens tested at the lowest temperatures, 1.9 and 3.4, show small mass gains, while those reaching higher temperatures without undergoing a temperature jump – samples 1.4, 1.8, 3.2, and 3.9 – show small mass losses. This result is consistent with previous Plasmatron tests of the $\text{ZrB}_2\text{-}30\text{SiC}$ material that showed no net mass loss below 1873 K,⁴⁶ and indicates that the production of a SiO_2 oxide scale exceeds the rate of SiO_2 volatilization below

this temperature. All specimens that underwent a temperature jump – specimens 1.5, 1.6, 1.7, 3.3, and 3.5 - show significantly higher mass loss. While some of this is probably due to mechanical removal of surface oxides, significant volatilization of SiO₂ is likely when temperatures exceed 2500 K as they have here.

E. Evidence of Volatilization

Emission spectroscopy of electronically excited B, Si, and W atoms was used to track the appearance and evolution of volatilized products in the gas phase. These atoms serve as convenient signatures, as they can only originate from the test article and have sharp spectral features that make them stand out from background molecular band emissions. The spectrometer channels centered at 249.92 nm, 288.16 nm, and 400. 99 nm were used to follow the B (²S_{1/2} → ²P_{1/2,3/2}^o), Si (P₁^o → ¹D₂) and W (⁷P₄^o → ⁷S₃) transitions.⁶⁴ The surface temperatures and raw signal intensities at these three emission wavelengths are shown together in Fig. 9 for the tests of specimens 1.5 and 3.3. Raw signal intensities are plotted over identical ranges in all panels and a logarithmic scale is used to highlight low intensity features.

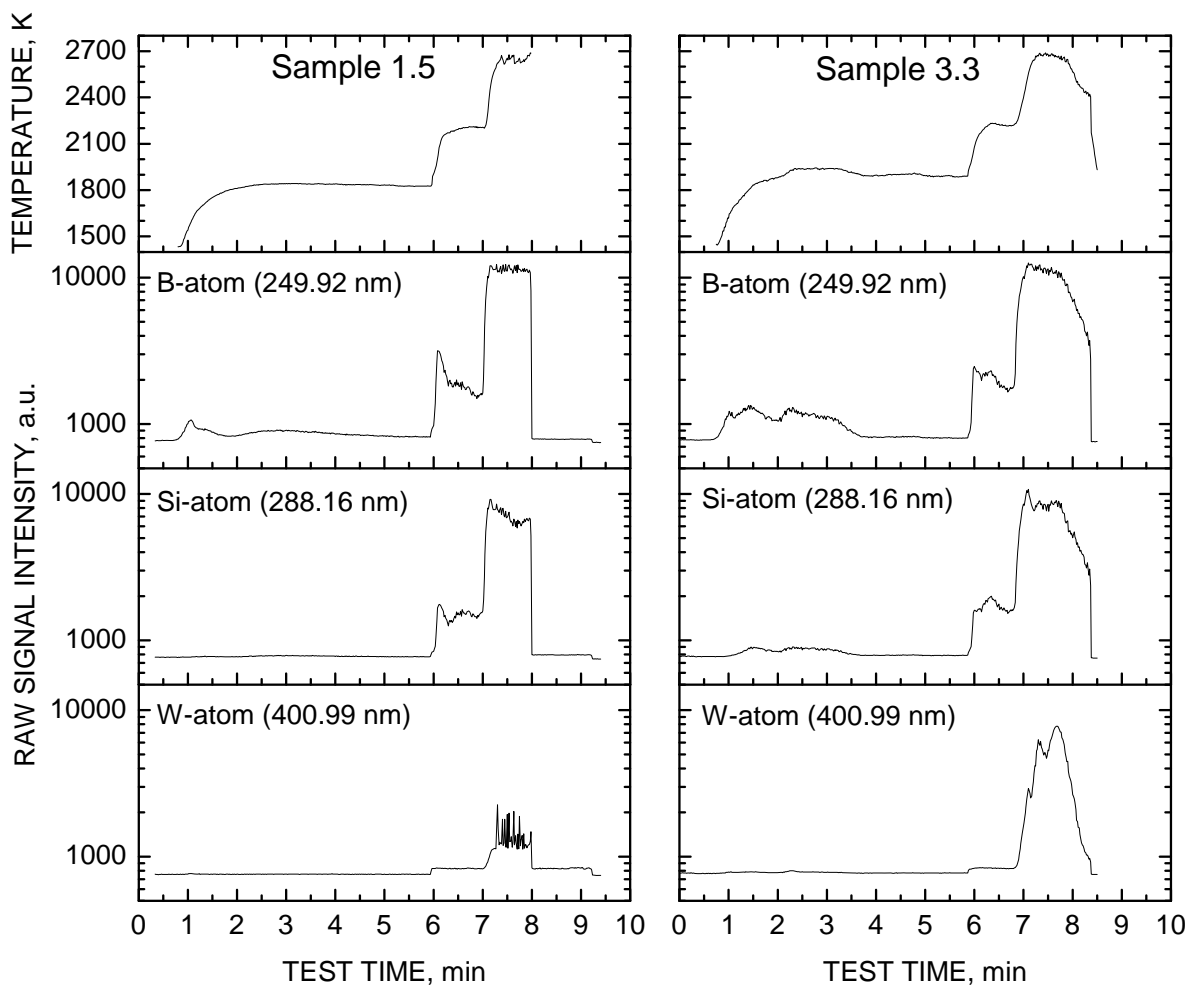


Fig. 9. Surface temperature and raw signal intensity for characteristic emission lines of boron, silicon, and tungsten atoms: ZrB₂-30SiC specimen 1.5 (left-hand panel) and (Zr,4W)B₂-30SiC specimen 3.3 (right-hand panel).

During the initial heating phase at low power, the rise and the eventual decay of the boron emission signal is observed for both specimens 1.5 and 3.3. This type of emission transient was seen before in Plasmatron testing of ZrB₂-30SiC⁶⁵ and is consistent with a simple model of oxide scale development that begins with B₂O₃ formation at low temperatures followed by boron oxide volatilization and silica scale growth at higher temperatures.⁶⁶ No Si atom emissions were observed in these previous tests. Here, a trace of Si emission can be detected for sample 1.5 and a very clear Si emission signal is seen for sample 3.3. Sample 3.3 reaches temperatures above 1900 K during the initial heat up phase, whereas sample 1.5 remains below 1850 K. No tungsten atom emissions are detected for sample 1.5 (as expected) and only a trace can be seen for sample 3.3.

Upon switching to the high-power condition, the emission intensities at the boron and silicon wavelengths rise sharply by a factor of 2 to 3. The increased boron and silicon emission intensity

is consistent with increased B_2O_3 and SiO_2 volatilization rates as the samples approach a higher steady-state surface temperature around 2215 K in response to the new freestream conditions. A small step change in intensity at the tungsten wavelength is seen for both specimens. Inspection of individual spectra indicates a baseline intensity offset between the low-power and high-power test conditions at this wavelength, not the presence of tungsten atom emission.

An additional factor of 2 to 3 increase in the B and Si wavelength emission intensity is observed as the temperature jump occurs on each sample. The signal intensity at the W wavelength also rises for both samples. In the case of sample 3.3, the presence of atomic tungsten is confirmed by an abundance of strong tungsten atom lines in individual emission spectra. These characteristic tungsten features are missing in the spectra of sample 1.5, and the measured emission at 400.99 nm is due to a strongly fluctuating background. These emission data confirm substantially increased oxide volatilization coinciding with the temperature jump phenomenon, which is coincident with the substantial mass loss measured for these specimens.

After roughly 30 seconds around 2660 K, the surface temperature of sample 3.3 decays steadily, and the B, Si, and W atom emissions follow suit. Similar temperature decays were seen for samples 1.6 and 1.7 (see Fig. 3), and similarly coincident decreases in Si and B emission intensity were observed.

Computational Results

The computed gas composition at the boundary layer edge is shown in Fig. 10 for the low- and high-power test conditions experienced by specimens 1.5, 1.6, 1.8, 3.3, 3.5, and 3.9. Oxygen is essentially fully dissociated at all Plasmatron powers used in this study, but the level of nitrogen dissociation increases between the low-power and high-power settings. The mole fractions of O_2 and NO are always less than 0.1% and 1%, respectively, and are effectively absent from Fig. 10. The O-atom mole fraction remains relatively constant around 30 – 35%, while the N_2 and N mole fractions change substantially between the low- and high-power conditions. The gas density will increase as the hot gas boundary layer edge gas approaches the cooler specimen surface, and both O-atom and N-atom mole fractions will decrease between the boundary layer edge and the sample surface because of gas-phase and surface recombination reactions.

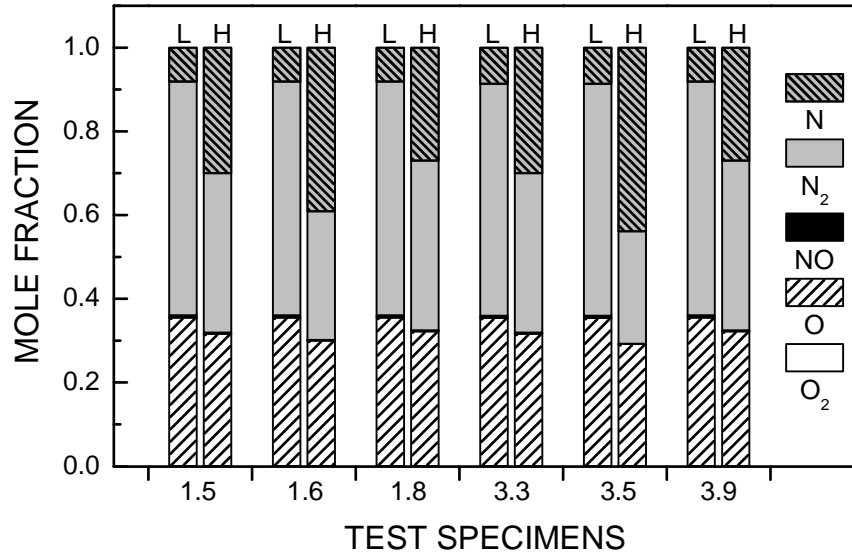


Fig. 10. Boundary layer edge gas composition for low (L) and high (H) power test conditions for specimens 1.5, 1.6, 1.8, 3.3, 3.5, and 3.9.

The heating conditions for test specimens 1.5, 1.6, 1.8, 3.3, 3.5, and 3.9 are listed in Table 3. The second and third columns of this table list the Plasmatron power and the measured cold-wall heat flux; the final three columns list average values of the surface temperature, emittance, and hot-wall heat flux for 30 second intervals characteristic of the low power, high power, and post-temperature jump conditions. The surface temperature and hot-wall heat flux values are used to locate each test on the heat flux abacus computed by the Boundary Layer Code, as described in Section IV. Table 4 shows the derived recombination coefficients, the ratio of hot-wall to fully-catalytic heat flux, and the computed air species number densities at the specimen surface for each test specimen under low- and high-power conditions.

Table 3 UHTC heating conditions.

Sample	Power, kW	q_{cw} , W cm $^{-2}$	T_w , K	ε	q_{hw}^{\dagger} , W cm $^{-2}$
1.5	200	109	1826	0.949	59.8
	353	202	2206	0.901	121
			2642	0.842	233
1.6	205	109	1865	0.946	65.0
	387	236	2841	0.791	292
1.8	212	109	1893	0.924	67.3
	292	185	2102	0.898	99.5
3.3	224	111	1889	0.946	68.4
	339	202	2223	0.891	123
			2669	0.830	239
3.5	203	111	1872	0.929	64.6
	402	253	2803	0.870	305
3.9	211	109	1877	0.925	65.1
	295	185	2119	0.886	101

† From $q_{hw} = \varepsilon\sigma T_w^4 + q_{cond}$, with $q_{cond} = 0$.

Table 4 Catalytic efficiencies, the ratios of hot-wall to fully-catalytic heat flux, and the species number densities at the surface.

Sample	γ	q_{hw}/q_{fc}	Number Density, $\times 10^{22} \text{ m}^{-3}$				
			[N ₂]	[N]	[O]	[O ₂]	[NO]
1.5	0.0031	0.48	23.90	1.174	14.16	0.358	0.088
	0.0099	0.47	16.28	5.333	10.83	0.313	0.093
	0.24	0.94	17.15	0.046	2.283	5.918	2.030
1.6	0.0051	0.52	23.90	0.608	13.52	0.691	0.177
	0.32	0.95	15.80	0.077	1.895	5.551	2.175
1.8	0.0063	0.54	23.67	0.403	13.02	0.929	0.245
	0.0062	0.43	16.88	5.816	11.49	0.217	0.060
3.3	0.0062	0.54	23.64	0.504	13.13	0.855	0.222
	0.0106	0.48	16.32	5.084	10.75	0.337	0.102
	0.37	0.96	17.02	0.027	1.432	6.499	2.167
3.5	0.0047	0.51	23.58	0.826	13.58	0.567	0.143
	0.16	0.89	15.84	0.274	3.890	4.081	1.758
3.9	0.0052	0.53	23.73	0.574	13.39	0.716	0.185
	0.0067	0.44	16.91	5.578	11.41	0.235	0.065

The recombination coefficients for the low-power conditions range from $3.1 - 6.3 \times 10^{-3}$, slightly higher but of the same magnitude as previously reported for the $\text{ZrB}_2\text{-}30\text{SiC}$ composition for temperatures around 1850 K.⁶⁷ Recombination coefficients for samples 1.8 and 3.9 under high-power conditions are near the top end of this same range. Somewhat higher recombination coefficients of $\sim 1 \times 10^{-2}$ are derived for samples 1.5 and 3.3 in the high-power region before the temperature jump. Under all of these conditions, the observed hot-wall heat flux is in the range of 43-54% of the fully-catalytic heat flux.

After the temperature jump, extremely high catalytic efficiencies, ranging from 0.16 to 0.37, are necessary to reproduce the observed hot-wall heat fluxes. The observed hot-wall heat flux is upwards of 89% of the fully-catalytic value. Because of these large increases in catalytic efficiency, the computed gas composition at the sample surface after the temperature jump is very different from that before the temperature jump (see Table 4). For sample 1.5, the N-atom number density drops by a factor of ~ 115 and the O-atom concentration by a factor of ~ 5 . Similarly, for sample 3.3, the N-atom number density drops by a factor of ~ 190 and the O-atom concentration by a factor of ~ 7.5 .

Discussion

In this section, we examine the sensitivity of our conclusion that the temperature-jump corresponds to a large increase in the chemical heating component of heat flux; then we discuss exothermic oxidation reactions as sources of additional chemical heating at the surface. Finally, we comment on UHTC arc-jet and ICP test conditions in the context of published SiC oxidation experiments in partially-dissociated oxygen.

A. The Temperature Jump and Increased Chemical Heating

A heat flux abacus for the high-power conditions experienced by samples 1.5 and 3.3 is shown in Fig. 11. The dashed vertical arrows between zero and the $\gamma = 0$ contour indicate the convective heating component and the solid vertical lines arrows between the $\gamma = 0$ contour and the observed hot-wall heat flux indicate the chemical heating component. It is evident that within the present computational model the experimental post-temperature-jump temperature and heat flux can only be explained by a large increase in the chemical component of heating.

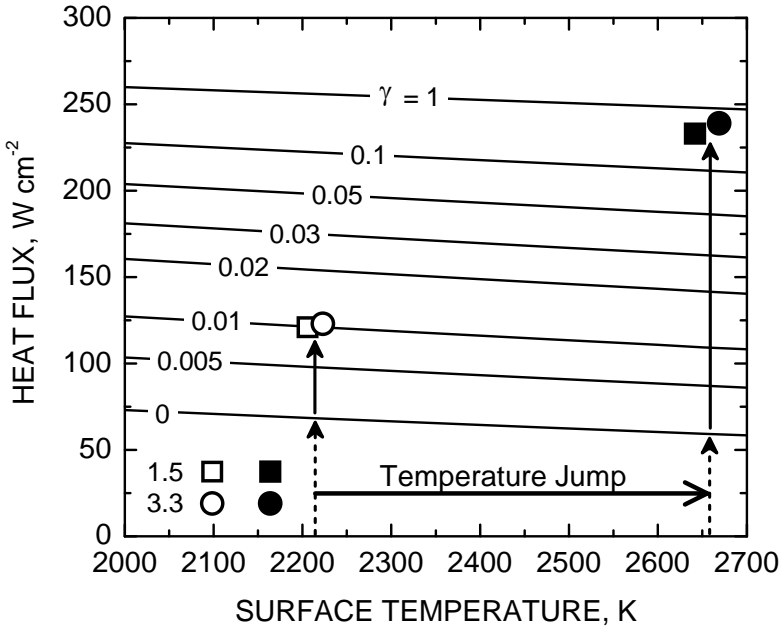


Fig. 11. Heat flux abacus for $P_{stat} = 10 \text{ kPa}$ and $H_e = 18.6 \text{ MJ kg}^{-1}$. The horizontal arrow indicates the temperature jump for specimens 1.5 and 3.3; the dashed and solid vertical arrows show the convective and chemical contributions to the computed heat flux, respectively.

Several factors can influence the location of the experimental (T_w, q_{hw}) point on the heat flux abacus. An error in surface temperature measured by the two-color radiometer can move the experimental point to the right or left on the abacus, but this does not change the magnitude of the chemical heating component necessary to reproduce the increased heat flux. An error in the radiance measured by the broad-band radiometer will shift the experimental heat flux (computed as $q_{hw} = q_{rad}$) up or down on the abacus, but this error is unlikely to exceed 5%, and does not change the result that the chemical heating contribution must increase at least threefold. Neglecting heat conduction loss in the estimate of hot-wall heat flux implies that the point (T_w, q_{hw}) is actually lower on the abacus than it should be. If the conduction loss exceeded 6% of the radiative heat flux, the true (T_w, q_{hw}) point would be above the fully catalytic ($\gamma = 1$) boundary for both samples 1.5 and 3.3 in Fig. 11.

The abacus itself is dependent on the edge conditions rebuilt using the calorimeter measurements. The largest uncertainty here is the catalytic efficiency assigned to the copper calorimeter surface; we have used a value of $\gamma = 0.01$. Krassilchikoff et al.⁶⁸ developed a combined experimental/computational procedure to derive appropriate catalytic recombination efficiencies for a cold copper surface and found values between 0.014 and 0.067. In general, as the calorimeter catalytic efficiency is increased, the rebuilt boundary layer edge enthalpy decreases, and a higher sample catalytic efficiency is required to reproduce an experimental (T_w, q_{hw}) point. A sensitivity study performed for the high heat flux conditions of sample 1.5

showed that any reference catalytic efficiency greater than 0.015 would place the experimental post-temperature jump (T_w, q_{hw}) point above the fully catalytic boundary. Obviously, this would also be the case if the common assumption of a fully catalytic copper surface were made.

While the outlined combination of experimental uncertainties, computational limitations, and analysis assumptions makes the extraction of accurate numerical values for surface reaction energetics problematic, they do not alter the conclusion that a very large increase in chemical heating is required to explain the temperature jump. Moreover, it seems probable that analysis corrections would tend to increase (rather than decrease) the already large estimates of chemical heating necessary to explain the temperature jump.

B. Oxidation and Volatilization

We emphasize that the boundary-layer computations used to compute the heat flux abacus are limited to 5-species air and that surface chemistry is constrained to a simple model of independent O-atom and N-atom recombination reactions. Clearly additional chemical mechanisms are in play on UHTC surfaces involving the formation and volatilization of silicon and boron oxides.

Surface oxidation processes that transform ZrB_2 and SiC into condensed and volatile oxides are all exothermic and release more energy per oxygen atom consumed than catalytic recombination to molecular oxygen ($\Delta H_r = -256 \text{ kJ mol}^{-1}$). On the other hand, processes that lead to the volatilization of condensed oxides are all endothermic. As an example, consider the four reactions:



These reactions describe, respectively: R1) the passive oxidation of SiC ; R2) the active oxidation of SiC ; R3) the decomposition of SiO_2 at the SiO_2/SiC interface; and R4) the congruent evaporation of SiO_2 . The standard reaction enthalpies listed were computed with the HSC Chemistry program⁶⁹ for 2500 K, but values do not change much with temperature in the 2000 to 3000 K range. Similar reactions can be written for ZrB_2 oxidation and the decomposition and volatilization of boron oxides.

More energy is released (per O-atom consumed) during passive than active SiC oxidation. However, if the SiO_2/SiC interface remains stable and the SiO_2 evaporation rate is low, condensed SiO_2 forms an effective oxygen diffusion barrier, slowing further oxidation, and in turn reducing the rate at which energy is released at the reaction interface. Under such passive oxidation conditions, exothermic oxidation reactions and endothermic evaporation/decomposition reactions have little impact on the heat balance at the surface, and the chemical component of heat flux is dominated by surface catalytic reactions. This situation characterizes the low-power test conditions of this study.

If the sample temperature is raised, the rates of both the oxidation and volatilization reactions increase, and it is possible to achieve a quasi-steady-state where condensed-phase oxide is formed and volatilized at similar rates, and where the net contribution of these reactions to the chemical heat flux remains largely neutral. This regime may describe the behavior of samples 1.4, 1.8, 3.2, and 3.9 under the high-power test conditions. These samples all lost some mass, but the derived recombination coefficients (for samples 1.8 and 3.9) do not differ much from samples tested under the low-power condition.

In contrast, under the high-power test conditions of samples 1.5 and 3.3, emission spectroscopy demonstrates that the silicon and boron species volatility is high prior to the temperature jump and increases even further after the temperature jump. A plausible scenario is that the existing borosilicate oxide scale is steadily eroded during the pre-temperature jump induction period by decomposition reactions at the scale/substrate interface and/or evaporative processes at the scale surface. Once the oxide scale is sufficiently eroded – whatever the mechanism(s) – the scale no longer limits oxygen diffusion effectively causing exothermic oxidation reactions to accelerate. Consequently, their contributions to the chemical heat flux will increase and the surface temperature will rise. The oxidation reaction rates will increase further with rising temperature, and this process can “run away” until a new steady-state is reached where oxidation produces primarily ZrO_2 and gaseous silicon and boron oxides, and where the higher chemical heating rate is again balanced by radiation losses.

In this scenario, the observation of a temperature jump is directly related to existence of a well developed silica-rich oxide scale that retards the response time of the UHTC specimen to the switch from low-power to high-power heating conditions, the latter of which favors active over passive oxidation. The time required for the existing oxide scale to decompose/volatilize would be shorter for larger power increases, consistent with the results for samples 1.6, 1.7, and 3.5 versus samples 1.5 and 3.3. If a sample were exposed directly to a high-power condition favoring active oxidation, no temperature jump would be expected, since the sample would transition smoothly into the active oxidation regime during heating. This latter scenario may also explain why no temperature jump was observed for the $(Zr,4W)B_2$ samples and why they reached higher surface temperatures than the ZrB_2 -30SiC and $(Zr,4W)B_2$ -30SiC specimens under similar low-power conditions; under the low-power conditions of this study boron oxide volatilization is already substantial enough that no oxidation protection is afforded by a condensed B_2O_3 scale, allowing active exothermic oxidation reactions (for example, $O + 1/5ZrB_2(s) = 1/5ZrO_2(s) + B_2O_3; \Delta H_r = -574 \text{ kJ mol}^{-1}$) to operate effectively.

It is certainly possible that, in addition to oxidation reactions, other exothermic surface and gas-phase reactions help sustain the high surface temperatures observed after the temperature jump. One possible heat source is enhanced O-atom and N-atom surface recombination on zirconia versus silica. Balat-Pichelin et al.⁵⁸ have measured the O-atom recombination coefficient on zirconia surfaces and found values on the order of 0.1-0.2 between 2000 K and 2400 K. (The recombination coefficient for N atoms on zirconia has apparently never been measured.) Increased N-atom recombination on SiC versus SiO_2 was used by Herdrich et al.³⁶ to explain part of the increased heat flux to the surface after temperature jumps associated with the

PA transition on SiC. A further possibility is that volatilized Si or B species react exothermically with O or N in the boundary-layer. For example, Hald⁷⁰ has suggested a catalytic cycle involving the exothermic gas-phase reactions $\text{Si} + \text{N} \rightarrow \text{SiN}$ followed by $\text{SiN} + \text{N} \rightarrow \text{N}_2 + \text{Si}$ to explain high surface temperatures after temperature jumps observed for C/SiC materials. Such a mechanism would raise the temperature of the boundary layer and hence the convective component of heating to the surface. Unraveling these different possibilities will require the development of appropriate materials response and CFD models that include all relevant gas-phase and surface chemistries.

C. Test Conditions and the PA Transition

The transition boundary between the passive and the active oxidation regimes of SiC is typically discussed as a function of temperature and oxygen pressure. Even in molecular oxygen, the precise location of this boundary varies significantly between different researchers. Laboratory tests by Balat³¹⁻³² and Rosner and Allendorf³³ in low-pressure partially dissociated flows suggest that the boundary is pushed to lower oxygen pressures at a given temperature; i.e., that the temperature-pressure parameter space for passive oxidation is larger in the presence of atomic oxygen.

Rosner and Allendorf³³ conducted experiments in $\text{N}_2\text{-Ar}$ at a low total pressure (~133 Pa) and O-atom partial pressures on the order of 0.1 to 1 Pa. Balat³² conducted experiments in partially-dissociated air at total pressures of 600 to 5000 Pa and O-atom partial pressures in the range 20 to 2000 Pa. Our test conditions are closer to those of Balat than those of Rosner and Allendorf. The computed O-atom partial pressures at the sample surface are about 3300 to 3600 Pa for all our pre-temperature jump test conditions. After the switch to high power, samples 1.4, 1.8, 3.2 and 3.9 reached temperatures near 2110 K and remained stable, whereas samples 1.5 and 3.3 reached temperatures near 2215 K and eventually underwent the temperature jump. A transition temperature near 2150 K for our computed O-atom pressures is consistent with the transition boundary published by Balat³² for tests on CVD SiC, but is significantly higher (by ~300 K) than the transition boundary for sintered SiC published by the same author.

Previous tests of the $\text{ZrB}_2\text{-30SiC}$ composite were conducted in the VKI Plasmatron facility using the same mass flow and static pressure, but at lower powers and on flat faced samples held in the standard ESA 50 mm stagnation point test fixture.⁴⁶⁻⁴⁷ Maximum sample temperatures remained below 1900 K in these tests and no temperature jumps were observed. This result is also consistent with Balat's transition boundary for CVD SiC.

It is difficult to compare other previous UHTC tests with predicted SiC PA transition boundaries because the oxygen partial pressures at the specimen surface are not determined.

The example cited by Glass,³⁹ of a sudden temperature jump during UHTC arc-jet testing for the SHARP B1 program,⁴⁰ occurred over about 15 seconds with the temperature rising from 2360 to 2810 K. The arc-jet operating conditions and the $\text{ZrB}_2\text{-SiC}$ composition were not specified, but the temperature profile, the temperature at which the jump initiated, and the magnitude of the temperature jump are all very similar to those observed for samples 1.6 and 3.5 in this study.

Monteverde, Savino, and colleagues have tested ZrB_2 -15SiC and ZrB_2 -20SiC composites in the form of hemispheres and cones in the arc-jet facility at the University of Naples using stepwise increases in power resulting in stepwise increases in measured surface temperature.⁴¹⁻⁴⁴ Surface temperatures approached ~ 2200 K under subsonic atmospheric pressure conditions⁴¹ and ~ 2100 K in supersonic low pressure flows,⁴²⁻⁴⁴ but no evidence of a temperature jump is found in published experimental temperature profiles.

Zhang et al.⁴⁵ have tested flat-faced ZrB_2 -20SiC specimens in an arc-jet environment at cold-wall heat fluxes of 170 W cm^{-2} and 540 cm^{-2} . Specimens reached peak temperatures of ~ 1930 K and 2603 K under these conditions, respectively, and no temperature jump is seen in their heating profiles. However, the two maximum temperatures lie below and above the ~ 2200 K level where we observe the phenomenon in our experiments, and it is possible that the temperature jump is simply part of the initial temperature rise under the high heat flux condition.

Gasch et al.⁷¹ have heated HfB_2 -20SiC specimens in an arc-jet to temperatures near 2100 K, and documented a slow but steady rise in surface temperature starting after about 6 minutes. This temperature rise was on the order of 300 to 400 K over several minutes, and was attributed to the slow volatilization of silica from the scale leaving a residual HfO_2 surface of lower emittance, higher catalycity, and lower thermal conductivity.

The temperature jump phenomenon is likely a function of multiple material and environmental parameters: the composition of the UHTC material, the temperature, pressure, and composition of the gas-phase, sample configuration and freestream flow characteristics that determine reactant and product transport, etc. More systematic studies that isolate and vary specific parameters are required for a better understanding of the conditions and mechanisms that trigger the temperature jump. Since heat and mass transfer at the gas-surface interface result from the coupled transport and thermochemistry occurring in the boundary layer at the reacting surface, it is difficult to evaluate various potential contributions until the candidate chemical mechanisms and rate coefficients are incorporated into the computational tools used to simulate the experiment.

Summary and Conclusion

The experimental observations can be summarized as follows. The ZrB_2 -30SiC and $(\text{Zr},4\text{W})\text{B}_2$ -30SiC UHTC specimens heat up and oxidize as they are exposed to the high-enthalpy air flow in the Plasmatron. Below a certain Plasmatron power level, the specimens reach a steady-state temperature at which they form a stable surface oxide that slows progressive oxidation. Some volatilization of boron and silicon can be detected by emission spectroscopy, but net sample mass changes are small and the oxides scales retain a relatively smooth, homogeneous surface. Above a certain Plasmatron power, specimens reach a temperature at which their oxide scale is no longer protective or stable. For the current tests, conducted at a static pressure of 10 kPa, oxides at steady-state surface temperatures around 2100 K remained stable, while those heated to 2200 K became unstable after a short induction period. The $(\text{Zr},4\text{W})\text{B}_2$ specimens reached higher surface temperatures than the ZrB_2 -30SiC and $(\text{Zr},4\text{W})\text{B}_2$ -

30SiC materials for similar Plasmatron powers and did not exhibit a temperature jump phenomenon.

Emission spectroscopy during testing of ZrB₂-30SiC and (Zr,4W)B₂-30SiC materials shows a significant increase in boron and silicon atom emissions when the Plasmatron power is switched from the low- to high-power conditions, reflecting increased oxide volatility above 2100 K. A further large increase in emission intensity is observed as the temperature jump occurs. Video images show that the temperature jump initiates at a point on the specimen edge, and then progresses around the circumference and fills to the center of the specimen face.

By combining the measurements of the two-color and broadband radiometer, the total emittance is shown to decrease slightly when the temperature jump occurs, however this change in emittance is not sufficient to be the driving force for the temperature jump. Aerothermal heating computations based on the rebuilt freestream conditions for the high-power Plasmatron tests indicate that the observed temperature jumps require a large increase in the chemical contribution to heat flux to reproduce the experimental combination of surface temperature and heat flux.

Taken in aggregate, the experimental observations and computational analysis support the hypothesis that the temperature jump is associated with a transition in surface chemistry involving the Si-containing compounds – the silica-rich oxide scale and the silica former SiC – and is likely related to the passive-to-active oxidation transition observed for other SiC-containing composites in aerothermal test environments. A deeper understanding of the temperature jump phenomenon in UHTC materials will require additional testing to span a wider temperature, pressure, and composition parameter space, and the development of appropriate materials response and CFD models to capture observed oxidation transition behavior in dissociated gas flows.

Acknowledgments

This research was supported by the High-Temperature Aerospace Materials Program of the Air Force Office of Scientific Research through contracts F49550-08-C-0049 (Marschall and Pejaković) and FA9550-08-1-0414 (Panerai and Chazot). Support was also provided by the US Air Force Office of Scientific Research (Dr. Ali Sayir) and NASA (Dr. Anthony Calomino) under the National Hypersonics Science Center for Materials and Structures (Fahrenholtz and Hilmas through AFOSR Contract No. FA9550-09-1-0477). The authors would like to thank Jordi Perez for help in performing optical microscopy.

References

¹Fuller, J., Blum, Y., and Marschall, J., "Topical Issue on Ultra-High-Temperature Ceramics," *Journal of the American Ceramic Society*, Vol. 91, No. 5, 2008, pp. 1397-1502.

²Fuller, J., Hilmas, G., Fahrenholtz, W., Corral, E., and Riegel, L., "Special Issue: Aerospace Materials for Extreme Environments," *Journal of the European Ceramic Society*, Vol. 30, No. 11, 2010, pp. 2145-2418.

³Fuller, J. and Sacks, M., "Special Section: Ultra-High Temperature Ceramics," *Journal of Materials Science*, Vol. 39, No. 19, 2004, pp. 5885-6066.

⁴Fahrenholtz, W.G., Hilmas, G.E., Talmy, I.G., and Zaykoski, J.A., "Refractory Diborides of Zirconium and Hafnium," *Journal of the American Ceramic Society*, Vol. 90, No. 5, 2007, pp. 1347-1364.

⁵Rizzo, H.F., "Oxidation of Boron at Temperatures Between 400 and 1300 °C in Air," in *Boron - Synthesis, Structure, and Properties*, edited by J. A. Kohn and W. F. Nye, (Plenum Press, New York, 1968), p. 175-189.

⁶Kaufman, L., Clougherty, E.V., and Berkowitz-Mattuck, J.B., "Oxidation Characteristics of Hafnium and Zirconium Diboride," *Transactions of the Metallurgical Society of AIME*, Vol. 239, 1967, pp. 458-466.

⁷Berkowitz-Mattuck, J.B., "High-Temperature Oxidation III. Zirconium and Hafnium Diborides," *Journal of the Electrochemical Society*, Vol. 113, 1966, pp. 908-914.

⁸Fahrenholtz, W.G., "The ZrB₂ Volatility Diagram," *Journal of the American Ceramic Society*, Vol. 88, No. 12, 2005, pp. 3509-3512.

⁹Tripp, W.C. and Graham, H.C., "Thermogravimetric Study of the Oxidation of ZrB₂ in the Temperature Range of 800 to 1500 C," *Journal of the Electrochemical Society*, Vol. 118, No. 7, 1971, pp. 1195-1199.

¹⁰Kuriakose, A.K. and Margrave, J.L., "The Oxidation Kinetics of Zirconium Diboride and Zirconium Carbide at High Temperatures," *Journal of the Electrochemical Society*, Vol. 111, No. 7, 1964, pp. 827-831.

¹¹Tripp, W.C., Davis, H.H., and Graham, H.C., "Effect of an SiC Addition on the Oxidation of ZrB₂," *Ceramic Bulletin*, Vol. 52, No. 8, 1973, pp. 612-616.

¹²Clougherty, E.V., Pober, R.L., and Kaufman, L., "Synthesis of Oxidation Resistant Metal Diboride Composites," *Transactions of the Metallurgical Society of AIME*, Vol. 242, 1968, pp. 1077-1082.

¹³Monteverde, F. and Bellosi, A., "Oxidation of ZrB₂-Based Ceramics in Dry Air," *Journal of the Electrochemical Society*, Vol. 150, No. 11, 2003, pp. B552-B559.

¹⁴Monteverde, F. and Scatteia, L., "Resistance to Thermal Shock and to Oxidation of Metal Diborides-SiC Ceramics for Aerospace Application," *Journal of the American Ceramic Society*, Vol. 90, No. 4, 2007, pp. 1130-1138.

¹⁵Karlsdottir, S.N., Halloran, J.W., and Henderson, C.E., "Convection Patterns in Liquid Oxide Films on ZrB₂-SiC Composites Oxidized at a High Temperature," *Journal of the American Ceramic Society*, Vol. 90, No. 9, 2007, pp. 2863-2867.

¹⁶Rezaie, A., Fahrenholtz, W.G., and Hilmas, G.E., "Evolution of Structure During the Oxidation of Zirconium Diboride-Silicon Carbide in Air up to 1500 °C," *Journal of the European Ceramic Society*, Vol. 27, 2007, pp. 2495-2501.

¹⁷Rezaie, A., Fahrenholtz, W.G., and Hilmas, G.E., "Oxidation of Zirconium Diboride-Silicon Carbide at 1500 °C at a Low Partial Pressure of Oxygen," *Journal of the American Ceramic Society*, Vol. 89, No. 10, 2006, pp. 3240-3245.

¹⁸Opeka, M.M., Talmy, I.G., and Zaykoski, J.A., "Oxidation-Based Materials Selection for 2000 °C+ Hypersonic Aerosurfaces: Theoretical Considerations and Historical Experience," *Journal of Materials Science*, Vol. 39, No. 19, 2004, pp. 5887-5904.

¹⁹Zhang, S.C., Hilmas, G.E., and Fahrenholtz, W.G., "Improved Oxidation Resistance of Zirconium Diboride by Tungsten Carbide Additions," *Journal of the American Ceramic Society*, Vol. 91, No. 11, 2008, pp. 3530-3535.

²⁰Zhang, S.C., Hilmas, G.E., and Fahrenholtz, W.G., "Oxidation of Zirconium Diboride with Tungsten Carbide Additions," *Journal of the American Ceramic Society*, Vol. 94, No. 4, 2011, pp. 1198-1205.

²¹Eakins, E., Jayaseelan, D.D., and Lee, W.E., "Toward Oxidation-Resistant ZrB₂-SiC Ultra High Temperature Ceramics," *Metallurgical and Materials Transactions* Vol. 42A, 2011, pp. 878-887.

²²Jacobson, N.S. and Myers, D.L., "Active Oxidation of SiC," *Oxidation of Metals*, Vol. 75, No. 1-2, 2011, pp. 1-25.

²³Hinze, J.W. and Graham, H.C., "The Active Oxidation of Si and SiC in the Viscous Gas-Flow Regime," *Journal of the Electrochemical Society*, Vol. 123, 1976, pp. 1066-1073.

²⁴Wang, J., Zhang, L., Zeng, Q., Vignoles, G.L., and Guette, A., "Theoretical Investigation for the Active-Passive Transition in the Oxidation of Silicon Carbide," *Journal of the American Ceramic Society*, Vol. 91, No. 5, 2008, pp. 1665-1673.

²⁵Schneider, B., Guette, A., Naslain, R., Cataldi, M., and Costecalde, A., "A Theoretical and Experimental Approach to the Active-to-Passive Transition in the Oxidation of Silicon Carbide," *Journal of Materials Science*, Vol. 33, 1998, pp. 535-547.

²⁶Narushima, T., Goto, T., Iguchi, Y., and Hirai, T., "High-Temperature Active Oxidation of Chemically Vapor-Deposited Silicon Carbide in an Ar-O₂ Atmosphere," *Journal of the American Ceramic Society*, Vol. 74, 1991, pp. 2583-2586.

²⁷Vaughn, W.L. and Maahs, H.G., "Active-to-Passive Transition in the Oxidation of Silicon Carbide and Silicon Nitride in Air," *Journal of the American Ceramic Society*, Vol. 73, No. 6, 1990, pp. 1540-1543.

²⁸Goto, T. and Homma, H., "High-Temperature Active/Passive Oxidation and Bubble Formation of CVD SiC in O₂ and CO₂ Atmospheres," *Journal of the European Ceramic Society*, Vol. 22, 2002, pp. 2749-2756.

²⁹Wagner, C., "Passivity During the Oxidation of Silicon at Elevated Temperatures," *Journal of Applied Physics*, Vol. 29, 1958, pp. 1295-1297.

³⁰Narushima, T., Goto, T., Yokoyama, Y., Hagiwara, J., Iguchi, Y., and Hirai, T., "High-Temperature Active Oxidation and Active-to-Passive Transition of Chemically Vapor-Deposited Silicon Nitride in N₂-O₂ and Ar-O₂ Atmospheres," *Journal of the American Ceramic Society*, Vol. 77, No. 9, 1994, pp. 2369-2375.

³¹Balat, M., Flamant, G., Male, G., and Pichelin, G., "Active to Passive Transition in the Oxidation of Silicon Carbide at High Temperature and Low Pressure in Molecular and Atomic Oxygen," *Journal of Materials Science*, Vol. 27, 1992, pp. 697-703.

³²Balat, M.J.H., "Determination of the Active-to-Passive Transition in the Oxidation of Silicon Carbide in Standard and Microwave-Excited Air," *Journal of the European Ceramic Society*, Vol. 16, 1996, pp. 55-62.

³³Rosner, D.E. and Allendorf, H.D., "High Temperature Kinetics of the Oxidation and Nitridation of Pyrolytic Silicon Carbide in Dissociated Gases," *Journal of Physical Chemistry*, Vol. 74, 1970, pp. 1829-1839.

³⁴Laux, T. and Auweter-Kurtz, M., "Untersuchung Des Passive-Aktiv-Übergangs an SiC in Sauerstoffplasmen."

³⁵Laux, T., Herdrich, G., and Auweter-Kurtz, M., "Oxidation Behavior of Sintered Silicon Carbide in Various Plasma Wind Tunnels," in *Hot Structures and Thermal Protection Systems for Space Vehicles, Proceedings of the 4th European Workshop held 26-29 November, 2002 in Palermo, Italy.*; Vol. ESA SP-521, edited by A. Wilson, (European Space Agency, Paris, 2003), p. 377-379.

³⁶Herdrich, G., Fertig, M., Löhle, S., Pidan, S., and Augweter-Kurtz, M., "Oxidation Behavior of Siliconcarbide-Based Materials by Using New Probe Techniques," *Journal of Spacecraft and Rockets*, Vol. 42, No. 5, 2005, pp. 817-824.

³⁷Panerai, F., Chazot, O., and Helber, B., "Gas/Surface Interaction Study on Ceramic Matrix Composite Thermal Protection System in the VKI Plasmatron Facility," AIAA Paper 2011-3642, June 2011.

³⁸Lacombe, A. and Lacoste, M., "Investigation of C/SiC "Breaking Point" Under Arc Jet Environment at NASA - J.S.C.," *High Temperature Chemical Processes*, Vol. 3, 1994, pp. 285-296.

³⁹Glass, D.E., "Physical Challenges and Limitations Confronting the Use of UHTCs on Hypersonic Vehicles," AIAA Paper 2011-2304, April 2011.

⁴⁰Kolodziej, P., Bull, J., Salute, J., and Keese, D.L., "First Flight Demonstration of a Sharp Ultra-High Temperature Ceramic Nosecone," NASA TM-112215, December 1997.

⁴¹Monteverde, F. and Savino, R., "Stability of Ultra-High Temperature ZrB₂-SiC Ceramics Under Simulated Atmospheric Re-Entry Conditions," *Journal of the European Ceramic Society*, Vol. 27, 2007, pp. 4797-4805.

⁴²Monteverde, F., Savino, R., and De Stefano Fumo, M., "Dynamic Oxidation of Ultra-High Temperature ZrB₂-SiC Under High Enthalpy Supersonic Flows," *Corrosion Science*, Vol. 53, 2011, pp. 922-929.

⁴³Monteverde, F., Savino, R., De Stefano Fumo, M., and Di Maso, A., "Plasma Wind Tunnel Testing of Ultra-High Temperature ZrB₂-SiC Composites Under Hypersonic Re-Entry Conditions," *Journal of the European Ceramic Society*, Vol. 30, No. 11, 2010, pp. 2313-2321.

⁴⁴Savino, R., De Stefano Fumo, M., Paterna, D., Di Maso, A., and Monteverde, F., "Arc-Jet testing of Ultra-High-Temperature-Ceramics," *Aerospace Science and Technology*, Vol. 14, 2010, pp. 178-187.

⁴⁵Zhang, X., Hu, P., Han, J., and Meng, S., "Ablation Behavior of ZrB₂-SiC Ultra High Temperature Ceramics under Simulated Atmospheric Re-Entry Conditions," *Composites Science and Technology*, Vol. 68, 2008, pp. 1718-1726.

⁴⁶Marschall, J., Pejakovic, D.A., Fahrenholtz, W.G., Hilmas, G.E., Zhu, S.M., Ridge, J., Fletcher, D.G., Asma, C.O., and Thomel, J., "Oxidation of ZrB₂-SiC Ultrahigh-Temperature Ceramic Composites in Dissociated Air," *Journal of Thermophysics and Heat Transfer*, Vol. 23, No. 2, 2009, pp. 267-278.

⁴⁷Playez, M., Fletcher, D.G., Marschall, J., Fahrenholtz, W.G., Hilmas, G.E., and Zhu, S.M., "Optical Emission Spectroscopy During Plasmatron Testing of ZrB₂-SiC Ultrahigh-Temperature Ceramic Composites," *Journal of Thermophysics and Heat Transfer*, Vol. 23, No. 2, 2009, pp. 279-285.

⁴⁸Bottin, B., Carbonaro, M., Zemsch, S., and Degrez, G., "Aerothermodynamic Design of an Inductively Coupled Plasma Wind Tunnel," AIAA Paper 1997-2498, June 1997.

⁴⁹Bottin, B., Paris, S., Van Der Haegen, V., and Carbonaro, M., "Experimental and Computational Determination of the VKI Plasmatron Operating Envelope," AIAA Paper 1999-3607, June 1999.

⁵⁰Barbante, P.F. and Chazot, O., "Flight Extrapolation of Plasma Wind Tunnel Stagnation Region Flowfield," *Journal of Thermophysics and Heat Transfer*, Vol. 20, No. 3, 2006, pp. 493-499.

⁵¹Barbante, P.F., Degrez, G., and Sarma, G.S.R., "Computation of Nonequilibrium High-Temperature Axisymmetric Boundary-Layer Flows," *Journal of Thermophysics and Heat Transfer*, Vol. 16, No. 4, 2002, pp. 490-497.

⁵²Magin, T., Vanden Abeele, D.P., and Degrez, G., "An Implicit Multiblock Solver for Inductive Plasma Flows," AIAA Paper 2000-2480, June 2000.

⁵³Vanden Abeele, D.P. and Degrez, G., "Numerical Model of High-Pressure Air Inductive Plasma Under Thermal and Chemical Non-Equilibrium," AIAA Paper 2000-2416, June 2000.

⁵⁴Bottin, B., Vanden Abeele, D.P., Carbonaro, M., Degrez, G., and Sarma, G.S.R., "Thermodynamic and Transport Properties for Inductive Plasma Modeling" *Journal of Thermophysics and Heat Transfer*, Vol. 13, No. 3, 1999, pp. 343-350.

⁵⁵Dunn, M.G. and Kang, S.-W., "Theoretical and Experimental Studies of Reentry Plasmas," NASA CR-2232 National Aeronautics and Space Administration, Washington D.C., April 1973.

⁵⁶Chazot, O., "Experimental Studies on Hypersonic Stagnation Point Chemical Environment," RTO-EN-AVT-142, *RTO/AVT/VKI Lecture Series*, von Karman Institute for Fluid Dynamics, Rhode-St-Genèse, Belgium, February 6-10, 2006.

⁵⁷Bedra, L. and Balat-Pichelin, M., "Comparative Modeling Study and Experimental Results of Atomic Oxygen Recombination on Silica-Based Surfaces at High-Temperature," *Aerospace Science and Technology*, Vol. 9, 2005, pp. 318-328.

⁵⁸Balat-Pichelin, M., Passarelli, M., and Vesel, A., "Recombination of Atomic Oxygen on Sintered Zirconia at High Temperature in Non-Equilibrium Air Plasma," *Materials Chemistry and Physics*, Vol. 123, pp. 40-46.

⁵⁹Gorshkov, A.B., "Numerical Investigation of Heat Transfer on the Surface of Experimental Models in the Test Chamber of an Induction Plasmatron," *High Temperature*, Vol. 48, No. 3, 2010, pp. 427-435.

⁶⁰Chang, S.-C. and Su, C.-S., "Relationship Between Ultraviolet Radiation Induced Thermoluminescence and Crystalline Structure of ZrO₂," *Radiation Effects and Defects in Solids*, Vol. 127, No. 2, 1993, pp. 207-213.

⁶¹Harrison, D.E., Melamed, N.T., and Subbarao, E.C., "A New Family of Self-Activated Phosphors," *Journal of the Electrochemical Society*, Vol. 110, No. 1, 1963, pp. 23-28.

⁶²Pejaković, D.A., "Studies of the Phosphorescence of Polycrystalline Hafnia," *Journal of Luminescence*, Vol. 130, No. 6, 2010, pp. 1048-1054.

⁶³Modest, M.E., *Radiative Heat Transfer*, McGraw-Hill, Inc., New York, 1993.

⁶⁴Sansonettia, J.E. and Martin, W.C., "Handbook of Basic Atomic Spectroscopic Data," *Journal of Physical and Chemical Reference Data*, Vol. 34, No. 4, 2005, pp. 1559-2259.

⁶⁵Playez, M., Fletcher, D.G., Marschall, J., Fahrenholtz, W.G., Hilmas, G.E., and Zhu, S., "Optical Emission Spectroscopy during Plasmatron Testing of ZrB₂-SiC Ultra-High Temperature Ceramic Composites," *Journal of Thermophysics and Heat Transfer*, Vol. 23, No. 2, 2009, pp. 279-285.

⁶⁶Marschall, J. and Fletcher, D.G., "High-Enthalpy Test Environments, Flow Modeling and *in situ* Diagnostics for Characterizing Ultra-High Temperature Ceramics," *Journal of the European Ceramic Society*, Vol. 30, No. 11, 2010, pp. 2323-2336

⁶⁷Marschall, J., Pejaković, D.A., Fahrenholtz, W.G., Hilmas, G.E., Zhu, S., Ridge, J., Fletcher, D.G., Asma, C.O., and Thömel, J., "Oxidation of ZrB₂-SiC Ultra-High Temperature Ceramic Composites in Dissociated Air," *Journal of Thermophysics and Heat Transfer*, Vol. 23, No. 2, 2009, pp. 267-278.

⁶⁸Krassilchikoff, H., Chazot, O., and Thömel, J., "Procedure for the Determination of Cold Copper Recombination Efficiency," 2nd European Conference for Aerospace Sciences, July 2007.

⁶⁹Roine, A., *HSC Chemistry for Windows, Version 5.11*, Outokumpu Research Oy, Pori, Finland, 2006.

⁷⁰Hald, H., "Operational Limits for Reusable Space Transportation Systems Due to Physical Boundaries of C/SiC Materials," *Aerospace Science and Technology*, Vol. 7, No. 7, 2003, pp. 551-559.

⁷¹Gasch, M., Ellerby, D., Irby, E., Beckman, S., Gusman, M., and Johnson, S., "Processing, Properties, and Arc Jet Oxidation of Hafnium Diboride/Silicon Carbide Ultra High Temperature Ceramics," *Journal of Materials Science*, Vol. 39, No. 19, 2004, pp. 5925-5937.

APPENDIX 2

Thermal and Electrical Transport Properties of Spark Plasma Sintered HfB₂ and ZrB₂ Ceramics*

Luning Zhang, Dušan A. Pejaković, and Jochen Marschall
Molecular Physics Laboratory
SRI International, Menlo Park, California 94025

Matthew Gasch
Thermal Protection Materials & Systems Branch
NASA Ames Research Center, Moffett Field, California 94035

Abstract

The thermal and electrical transport properties of various spark-plasma-sintered HfB₂- and ZrB₂-based polycrystalline ceramics were investigated experimentally over the 300–700 K temperature range. Measurements of thermal diffusivity, electrical resistivity, and Hall coefficient are reported, as well as the derived properties of thermal conductivity, charge carrier density, and charge carrier mobility. Hall coefficients were negative confirming electrons as the dominant charge carrier, with carrier densities and mobilities in the $3\text{--}5 \times 10^{21} \text{ cm}^{-3}$ and $100\text{--}250 \text{ cm}^2 \text{ V}^{-1} \text{ s}^{-1}$ ranges, respectively. Electrical resistivities were lower, and temperature coefficients of resistivity higher, than those typically reported for HfB₂ and ZrB₂ materials manufactured by conventional hot-pressing. A Wiedemann-Franz analysis confirms the dominance of electronic contributions to heat transport. The thermal conductivity was found to decrease with increasing temperature for all materials. Results are discussed in terms of sample morphology and compared to data previously reported in the scientific literature.

I. Introduction

Ultra-high temperature ceramic (UHTC) composites based on HfB₂ and ZrB₂, together with minor silica forming constituents such as SiC, Si₃N₄, TaSi₂, and MoSi₂, are under investigation for use in aerothermal heating environments as sharp leading edge components on future generations of hypersonic reentry vehicles.^{1–3} Transition metal diborides have mechanical properties and brittle fracture behavior typical of ceramics, and yet their electrical and thermal conductivities are more characteristic of a metal.⁴ The ability to effectively conduct heat is a desirable property for sharp-leading-edge components, as it improves their thermal shock resistance by reducing temperature gradients and thermal stresses within the material, and

* This Appendix is an edited version of the manuscript published in The Journal of the American Ceramic Society, Vol. 94(8), 2011, pp. 2562–2570.

transports energy away from the stagnation point over a larger component surface area from which it can be efficiently radiated back to the environment.⁵

As typical of polycrystalline materials, the effective thermal and electrical conductivities of UHTC materials are affected by factors such as chemical composition, grain size, and porosity. The densification of pure ZrB_2 and HfB_2 materials by the conventional hot pressing of compound powders is difficult because of their hardness and very high melting points. Additives such as SiC , B_4C , and carbon can aid the sintering process, however extreme conditions of pressure and temperature are generally required. Moreover, processing times can still reach hours which encourages grain growth, undesirable from a mechanical property perspective. More recently, spark-plasma-sintering of elemental and compound powders, in which a pulsed DC current is applied during pressing, has been shown to produce dense ZrB_2 and HfB_2 composites at less extreme temperature and pressure conditions, and in shorter (tens of minutes) processing times.⁶⁻⁸

Here we investigate the thermal and electrical transport properties of nine spark-plasma-sintered (SPS) HfB_2 - and ZrB_2 -based polycrystalline ceramics over the 300–700 K temperature range. Thermal diffusivity, electrical resistivity, Hall Effect measurements, and microscopy are performed on the same specimen of each ceramic. Thermal conductivity, charge carrier density, and charge carrier mobility are derived from the measured data. The measurement of both thermal and electrical properties allows the analysis of electron and phonon contributions to thermal transport.

II. Experimental Procedure

(1) Materials and Processing

Specimens from nine different UHTC billets were tested; seven billets were HfB_2 -based materials and two were ZrB_2 -based materials. We have grouped the nine samples into three characteristic groups. Group (A) consists of nominally pure diboride materials; group (B) consists of the composites prepared with excess elemental constituents: B1 (HfB_2 -1% Ir), B2 (HfB_2 -4% Hf or $HfB_{1.9}$), and B3 (HfB_2 -2.5% B or $HfB_{2.1}$); group (C) consists of composites with SiC additions: C1 (HfB_2 -5% SiC), C2 (HfB_2 -5% SiC), and C3 (ZrB_2 -20% SiC). Volume percentages are used throughout this paper. Sample labels, target compositions, and processing identifiers are summarized in the second and third columns of Table 1.

The diboride phase was produced from the reaction of elemental metal (Hf or Zr) and boron in all but two billets (C1 and C3) which were produced from milled diboride powders. The following raw powders were used: HfB_2 (-325 mesh, 99.5%, CERAC, Milwaukee, WI), ZrB_2 (-325 mesh, 99.5%, CERAC), Hf (-325 mesh, 99.8%, CERAC), Zr (-325 mesh, 99.7%, CERAC), B (amorphous, -325 mesh, 99%, Alpha Aesar, Ward Hill, MA), SiC (UF-05, 99.8%, H. C. Starck, Newton, MA), and Ir (-325 mesh, 99.95%, Surepure Chemetals, Florham Park, NJ).

All elemental powders were used as-purchased without additional milling. Powders were combined in desired proportions and hand mixed prior to pressing, either on the bench top or within a glove box to minimize humidity (processing method “dry#” in Table 1). SiC powder

was also used as-purchased when combined with elemental powders, as for specimen C2. For the billets made using diboride powders (processing method “/c-1” in Table 1), the raw diboride and SiC powders were weighed and combined in the desired volumetric ratio, and then wet-milled in cyclohexane with WC milling media in a planetary mill (Fritsch Pulverisette 5, Germany). The milled powders were carefully dried to prevent phase segregation between the SiC and the denser diboride components.

Table I. Sample groups, target volumetric compositions, processing methods, densities (experimental, theoretical, and their ratio), mean intercept length ($\bar{L} \pm \sigma$) from log-normal fitting, and grain boundary area per unit volume (S_V).

Group ID	Target Composition	Processing ID	ρ_{exp} (g cm ⁻³)	ρ_{the} (g cm ⁻³)	ρ_{exp} / ρ_{the} %	$\bar{L} \pm \sigma$ (μm)	S_V (μm^{-1})
A1	HfB ₂	TC1/ ---	11.0	11.21	98.1	10.7 ± 4.9	0.205
A2	HfB ₂	TC3/ dry4	10.3	11.21	91.9	5.5 ± 3.2	0.386
A3	ZrB ₂	TC6/ dry2	5.66	6.12	92.5	5.6 ± 3.2	0.368
B1	HfB ₂ -1%Ir	TC5/ ---	11.1	11.33	98.0	10.3 ± 4.2	0.200
B2	HfB ₂ -4%Hf †	TC7/ dry1	11.0	11.29	98.1	10.0 ± 5.1	0.218
B3	HfB ₂ -2.5%B †	TC8/ dry1	11.1	10.99	101.0	10.9 ± 5.8	0.191
C1	HfB ₂ -5%SiC	TC2/ c-1	10.7	10.81	99.0	5.4 ± 2.2	0.387
C2	HfB ₂ -5%SiC	TC4/ dry1	11.0	10.81	101.8	5.5 ± 3.3	0.415
C3	ZrB ₂ -20%SiC	TC9/ c-1	5.50	5.54	99.3	A: 10.2 ± 5.5 B: 3.9 ± 1.9	AA: 0.215 AB: 0.206 Total: 0.421

† HfB₂-4%Hf = HfB_{1.9} and HfB₂-2.5%B = HfB_{2.1}

A: ZrB₂, B: SiC

All billets were consolidated by spark-plasma sintering (Model SPS-1050, Sumitomo Heavy Industries Ltd., Japan) at the University of California Davis. Powders were packed into 20 mm diameter graphite dies, loaded to 105-135 MPa, and densified at temperatures from 1700 to 1900°C, with hold times of 5–10 minutes. Heating rates during the SPS process were 100 to 300°C per minute. After pressing, test specimens were diamond-machined from the billets into 1 mm thick, 12.7 mm diameter disks. The thermal and electrical property measurements were performed on the same specimen from each billet.

(2) Sample Characterization

The densities of the test specimens were measured using the Archimedes method. The specimen crystal structure was characterized using an X-ray diffraction (XRD) apparatus (Phillips Electronics, New York, NY) with a Cu $K\alpha$ source and a Ge monochromator. After the completion of all thermal and electrical property testing, specimens were polished to a 1- μm

finish (Struers, RotoPol-31, Germany), chemically etched with molten potassium hydroxide (99.99%, Alpha Aesar, Ward Hill, MA) and fractured into smaller specimens. The microstructure of both the etched and fractured specimen surfaces were characterized using a JEOL 6100 high-resolution field-emission scanning electron microscope (JEOL Ltd., Tokyo, Japan) with accompanying setup (EDAX, Mahwah, NJ) for elemental analysis by energy dispersive spectroscopy (EDS).

Grain size analysis was performed on scanning electron microscope (SEM) images using the ImageJ program with the Concentric Circles plug-in.⁹ Two circles of known radius were superimposed on each SEM image and the arc length crossing each grain was determined by measuring the central angle of the arc and converting it into an intercept length, L . This procedure is similar to those found in ASTM standard E 112-96.¹⁰ Typically, 200-300 intercept length measurements were obtained for each etched specimen. From these measurements an intercept length probability density histogram with $1\mu\text{m}$ binning was constructed for each sample, and the histogram was fit by a log-normal distribution function:

$$f(L) = \frac{1}{\sigma L \sqrt{2\pi}} \exp\left[-\frac{(\ln L - \mu)^2}{2\sigma^2}\right], \quad (1)$$

where the fitting parameters μ and σ are the mean and standard deviation of $\ln L$. The mean and standard deviation of L are calculated from μ and σ by:

$$\bar{L} = \exp\left(\mu + \frac{1}{2}\sigma^2\right) \quad (2)$$

$$\sigma_L = \exp\left(\mu + \frac{1}{2}\sigma^2\right) \sqrt{\exp(\sigma^2) - 1} \quad (3)$$

The mean grain size \bar{D} is of similar magnitude to the mean intercept length \bar{L} , and various geometric approximations are available to make this conversion if desired.¹¹

The grain boundary interface area per volume, S_V , was also calculated for each specimen from the stereological relationship $S_V = 2N_{GB}/L_{tot}$, where N_{GB} is the total number of grain boundaries intersected by the two circles and L_{tot} is the sum of the two circle circumferences.¹²

(3) Thermal Diffusivity Measurements

Thermal diffusivity was measured using a photothermal radiometry technique in which the front face of a thin disk was periodically heated using a laser and the harmonic back-face temperature response was recorded and modeled to extract the thermal diffusivity. Photothermal techniques have been extensively developed and are widely used to measure the thermal properties of bulk and composite materials.¹³⁻¹⁵ The experimental arrangement used in our measurements is shown in Fig. 1.

The UHTC specimen was mounted by its edge in a cylindrical aluminum holder fit with a band heater capable of heating specimens to about 450°C . Specimen temperature was measured

by a type K thermocouple in direct contact with the specimen surface. A Synrad Firestar F400 CO₂ laser (output wavelength 10.6 μm), coupled to a Stanford Research Systems DG535 digital delay and pulse generator for output modulation, was used to irradiate the front face of the sample. A 3 \times beam expander (Haas Laser Technologies, Flanders, NJ) was used to expand the infrared beam diameter from about 3.5 mm at the laser exit to about 11 mm on the sample surface. This expansion made the Gaussian-like laser beam diameter much larger than the 1 mm sample thickness, assuring that heat transfer between the front and back faces of the sample was quasi one-dimensional near the center of the disk. Thermal emission originating from the center of the back face was focused by a CaF₂ lens onto a liquid-nitrogen cooled InSb detector (Infrared Laboratories Inc, Model ND-2). The detector output voltage was processed by a Stanford Research Systems SR830 lock-in amplifier to extract its amplitude and phase shift as a function of laser modulation frequency. Since the amplitude of the harmonic temperature component, δT_b , was small (~ 0.1 K), the detected emissive power variations were essentially linearly proportional to δT_b , as can be verified from a blackbody radiation analysis.

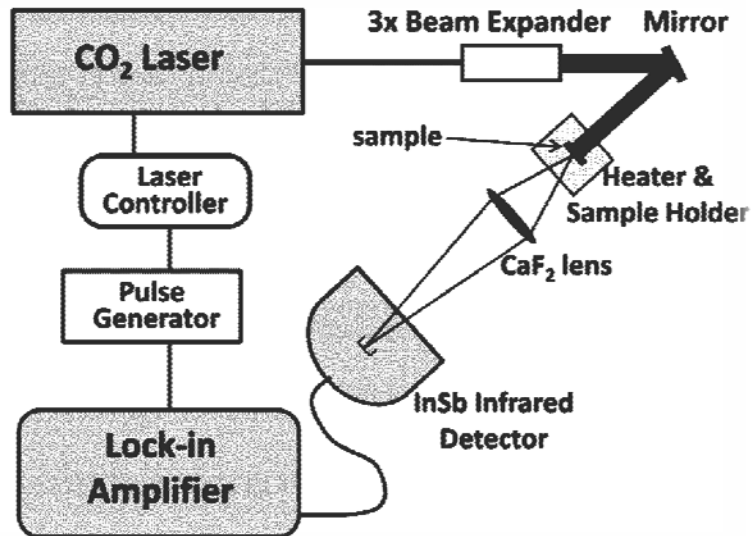


Fig. 1. Schematic of the photothermal radiometry setup for thermal diffusivity measurement.

A one-dimensional heat conduction model was used to determine the thermal diffusivity of the test specimens from the measured thermal emission. The harmonic component of the back-face temperature response to periodic front face heating is given by the complex expression¹⁵

$$\delta T_b = \frac{A}{\alpha} \frac{\exp(i\omega t)}{\sigma[\exp(\sigma d) - \exp(-\sigma d)]}, \quad (4)$$

where α is the thermal diffusivity, d is the sample thickness, t is time, and $\omega = 2\pi f$ with f the laser heating frequency in Hz. In Eq. (4), $\sigma = [1 + i]\sqrt{\omega/2\alpha}$ and the leading constant $A = I_0(1 - R)/\rho c_p$, where I_0 is the laser intensity, R is the reflectance of the illuminated

surface, ρ is the sample density and c_p is the sample heat capacity. Through algebraic manipulation of Eq. (4) the magnitude and phase shift of the harmonic temperature response are respectively

$$|\delta T_b| = \frac{A}{\sqrt{2\alpha\omega\pi}} \left[\frac{1}{P^2(M-N)^2 + Q^2(M+N)^2} \right] \quad (5)$$

and

$$\Phi = \tan^{-1} \left[-\frac{P(M-N) + Q(M+N)}{D(M-N) - Q(M+N)} \right] \quad (6)$$

with $M = \exp(d\sqrt{\omega\pi/\alpha})$, $N = \exp(-d\sqrt{\omega\pi/\alpha})$, $P = \cos(d\sqrt{\omega\pi/\alpha})$, and $Q = \sin(d\sqrt{\omega\pi/\alpha})$.

Equations (5) and (6) can be used to derive the thermal diffusivity by fitting the measured magnitude and phase shift of the detected thermal emission as a function of laser modulation frequency. Use of Eq. (5) requires two fitting parameters, A and α , while Eq. (6) requires only α . In practice we find phase shift fitting to be more reliable and reproducible than amplitude fitting because the amplitude of the harmonic temperature response becomes very small at high heating frequencies and is more susceptible to drifts in laser power and convective heat losses. Therefore, we report thermal diffusivity values derived by phase shift fitting. Based on the repeatability of measurements and fitting uncertainties, we estimate that reported thermal diffusivity values have uncertainties of about 5%. A standard graphite material, IG-110 nuclear grade from Toyo Tanso USA, was used to verify the performance of our photothermal radiometry setup. Disc samples with thicknesses of 1 and 2 mm were used. The measured thermal diffusivity at about 299 K was $1.02 \pm 0.03 \text{ cm}^2 \text{ s}^{-1}$, in very good agreement with the literature value of $1.03 \text{ cm}^2 \text{ s}^{-1}$ at the same temperature.¹⁶⁻¹⁷

(4) Electrical Property Measurements

Figure 2 shows the experimental arrangements used for the electrical resistivity and the Hall coefficient measurements. Both measurements use a standard four-terminal van der Pauw geometry¹⁸⁻¹⁹ in which a current is driven between two terminals while a voltage is measured between the remaining two terminals. A DC power supply (Global Specialties Instruments, model 1302B) was used as a constant current source and a multimeter (Keithley, model 2000) was used to measure voltages. Silver paint was used to form the electrical contacts between the lead wires and the disk samples. The Hall mobility measurements were performed in a custom-built electromagnet with a magnetic induction of 0.50 Tesla (as measured using a Bell 600 Gaussmeter, F. W. Bell Inc.). The electrical resistivity was measured as a function of temperature by placing the specimen on an electrically-isolated heating stage. Sample temperatures were measured with a type K thermocouple.

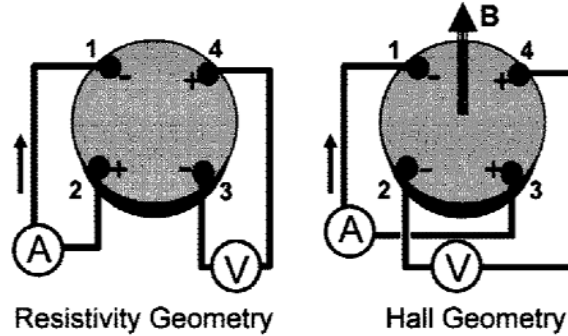


Fig. 2. Experimental geometries for electrical property measurements; the arrows indicate the direction of current flow for a particular test.

The sheet resistance for a van der Pauw measurement is $R_{ijkl} = V_{kl} / I_{ij}$, where the first two indices denote the positive (i) and negative (j) leads of the current input and the second two indices denote the positive (k) and negative (l) leads of the voltmeter. Figure 2 shows the van der Pauw geometry for measuring R_{2143} . In total, twenty-four measurements were made on each sample at each temperature. These consisted of three different current levels in the range of 1-2 A for each of the permutations $ijkl = 1234, 3412, 2143, 4321, 2341, 4123, 3214$, and 1432 . The three sheet resistances for each permutation were averaged and the electrical resistivity, r , was obtained by numerically solving the relation¹⁸⁻¹⁹

$$\exp\left(-\frac{\pi d(R_{1234} + R_{3412} + R_{2143} + R_{4321})}{4r}\right) + \exp\left(-\frac{\pi d(R_{2341} + R_{4123} + R_{3214} + R_{1432})}{4r}\right) = 1. \quad (7)$$

The performance of our setup was verified by making electrical resistivity measurements on thin sheets of nickel (0.125mm, Aldrich) and Constantan[®] (0.25 mm, Goodfellow). Our measured room temperature resistivities for nickel ($7.18 \mu\Omega \cdot \text{cm}$) and Constantan[®] ($50.4 \mu\Omega \cdot \text{cm}$) are within a few percent of literature values.²⁰⁻²¹

The Hall coefficient for a particular configuration is defined by $R_{H,ijkl}^{+/-} = V_{kl} d / I_{ij} B$, where the superscript (+ or -) defines the direction of the magnetic field perpendicular to the sample disk; the Hall geometry $R_{H,3142}^+$ is shown in Fig. 2. We fixed the current input and measured the voltage with the magnetic field turned off and on. In total, eight measurements were performed at a fixed current level (between 1 and 2 A) on each specimen: the permutations $ijkl = 1324, 3142, 2431$ and 4213 for each of the two magnetic field directions (+0.5 T and -0.5 T). The Hall coefficient was then computed as the average

$$R_H = (R_{1324}^+ + R_{3142}^+ + R_{2431}^+ + R_{4213}^+ + R_{1324}^- + R_{3142}^- + R_{2431}^- + R_{4213}^-) / 8. \quad (8)$$

The bulk carrier density and Hall mobility were computed as $n_e = 1/q_e R_H$ and $\mu_e = |R_H|/r$, respectively, where $q_e = -1.602 \times 10^{-19} \text{ C}$ is the charge of an electron.

III. Experimental Results

(1) Microstructure and Composition

Theoretical densities were computed from the target volume fractions and the following pure component densities (in g cm⁻³): $\rho_{HfB_2} = 11.212$ ⁴, $\rho_{ZrB_2} = 6.085$ ⁴, $\rho_{Hf} = 13.10$ ²², $\rho_B = 2.34$ ²², $\rho_{Ir} = 22.65$ ²², and $\rho_{SiC} = 3.214$ ²³. The experimental and theoretical densities are listed in the fourth and fifth columns of Table I. The sixth column of Table I shows that most specimens reached at least 98% of their theoretical density; the two exceptions are A2 (pure HfB₂) and A3 (pure ZrB₂), both of which are around 92% theoretical density. Two samples, B3 (HfB_{2.1}) and C2 (HfB₂-5%SiC) have densities higher than their theoretical values. The measured density of B3 is 1% higher than the theoretical value, suggesting that the final boron content did not reach the targeted 2.5% excess (or HfB_{2.1} composition). The measured density of C2 is ~2% greater than the theoretical value, indicating that the actual SiC content is lower than the target 5% volume fraction.

The sample analysis by XRD shows the characteristic sharp diffraction peaks of crystalline ZrB₂ and HfB₂, as well as a variety of weaker peaks associated with impurities and minor constituents, as shown in Fig. 3. Diffraction peaks associated with HfO₂ are found for most HfB₂-based specimens. Diffraction peaks associated with HfC can be clearly identified for A2 (HfB₂), C1 (HfB₂-5%SiC), and C2 (HfB₂-5%SiC) and ZrC peaks can be identified for A3 (ZrB₂). No XRD peaks related to Ir (B1: HfB₂-1%Ir) or Hf (B2: HfB₂-5%Hf) were found. Diffraction peaks associated with SiC were observed for sample C3 (ZrB₂-20%SiC), but could not be clearly identified for samples C1 and C2 containing nominally 5% SiC.

Consistent with XRD results, SEM/EDS specimen characterization confirmed the presence of oxygen and carbon containing grains in most materials, and could not identify any Ir-containing grains or pure Hf grains in samples B1 and B2, respectively. A small population of boron particles was found in specimen C3 (ZrB₂-20%SiC), which was likely inadvertently introduced during the manufacturing process. SiC grains were sparse but clearly identifiable in sample C1. However, no SiC grains were found in sample C2. Instead, a variety of distinct HfC and carbon-rich grains were identified. This surprising finding is consistent with the presence of the strong HfC lines in the XRD spectrum (Fig. 3), as well as the aforementioned discrepancy between the measured density and theoretical density for this specimen. Specimen C2 was manufactured using elemental Hf and B powders, and the reaction $Hf + SiC \rightarrow Si + HfC$, which could lead to the loss of SiC, is thermodynamically favored.²⁴ However EDS was unable to detect any Si-containing grains in sample C2.

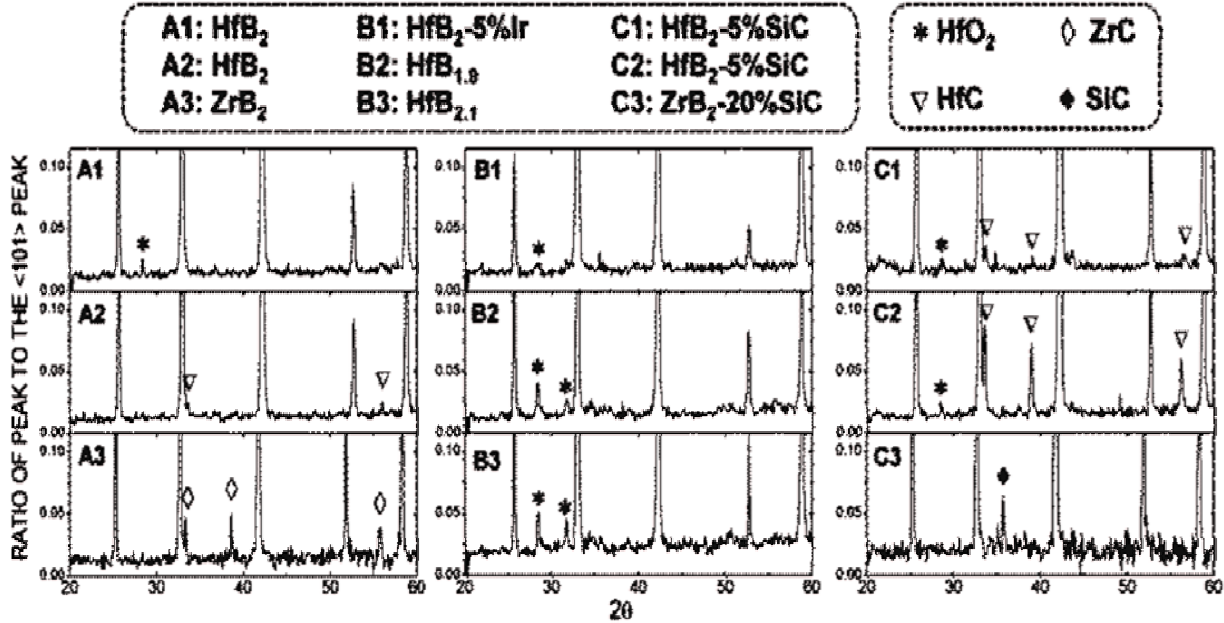


Fig. 3. X-ray diffraction scattering intensity versus scanning angle 2θ ; intensities have been normalized to the $<101>$ peak intensity.

Grain size analyses are presented in Fig. 4 as histograms with superimposed log-normal curve fits. The log-normal function provides a reasonable approximation to the experimental histograms. The values of \bar{L} and σ_L derived from these fits are listed in Table I, along with the derived grain boundary interface areas per unit volume. Values of \bar{L} fall into two groups: one group around $5.5 \mu\text{m}$ and another around $10.5 \mu\text{m}$. The samples with $\bar{L} \approx 5.5 \mu\text{m}$ have roughly twice the grain boundary interface area per volume than those with $\bar{L} \approx 10.5 \mu\text{m}$. The grain composition was not considered during grain size analysis of samples C1 and C2. For sample C3, we have differentiated the two grain boundary interfaces of ZrB_2 - ZrB_2 and ZrB_2 - SiC during analysis, and the individual and total interfacial areas of C3 are listed in Table I.

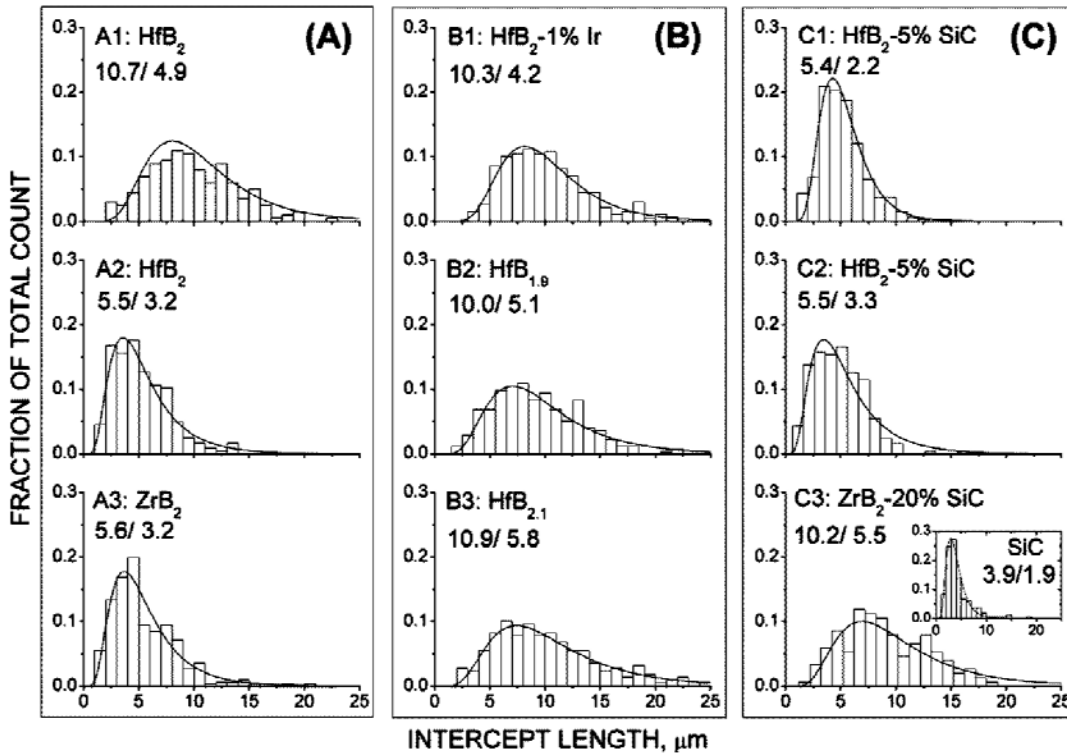


Fig. 4. Grain size distributions obtained from the analysis of SEM images; the mean and standard deviations of the intercept lengths are indicated in each panel.

(2) Thermal Properties

The measured thermal diffusivities are plotted in Fig. 5 over the 298-700 K temperature range. The thermal diffusivity of all materials decreases with increasing temperature. The Ir-containing HfB₂ composite B1 has the highest thermal diffusivity and the pure HfB₂ material A2 has the lowest thermal diffusivity over this temperature range; this difference is about a factor of 1.5 at room temperature and 1.2 at 700 K.

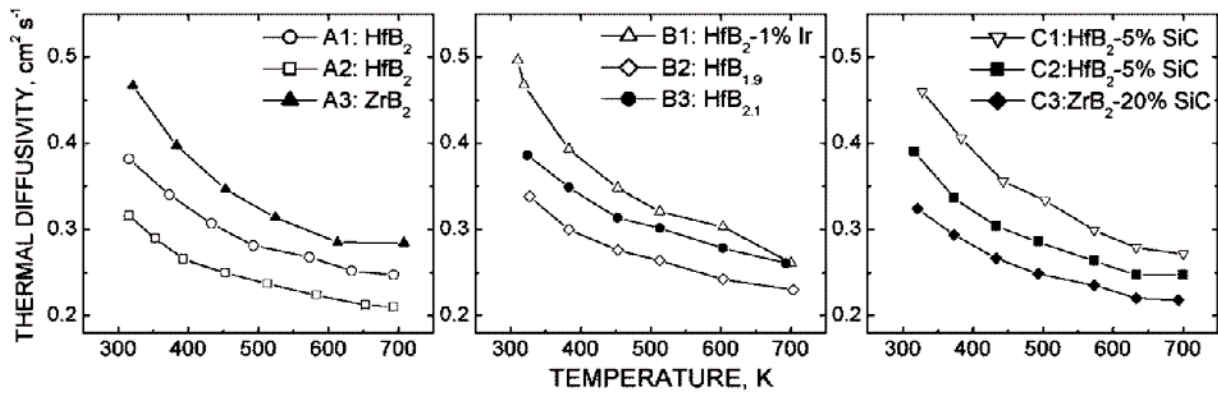


Fig. 5. Thermal diffusivities as a function of temperature.

Figure 6 shows thermal conductivity values computed from the measured thermal diffusivity data using the relation $\lambda = \alpha\rho c_p$. We have used the measured room-temperature densities of each sample, considering thermal expansion over the 298-700 K temperature range insignificant. Specific heat values for pure components were computed as a function of temperature using the expression

$$c_p(T) = A + BT + CT^{-2} + DT^2 \quad (9)$$

with coefficients derived from the HSC Chemistry database²⁴; these coefficients are listed in Table II. For composite samples, specific heat values were mass-averaged using theoretical densities and nominal volume fractions. We estimate that the uncertainty in our computed specific heat values does not exceed 10%. The thermal conductivity of all materials also decreases over this temperature range, although not as strongly as the thermal diffusivity.

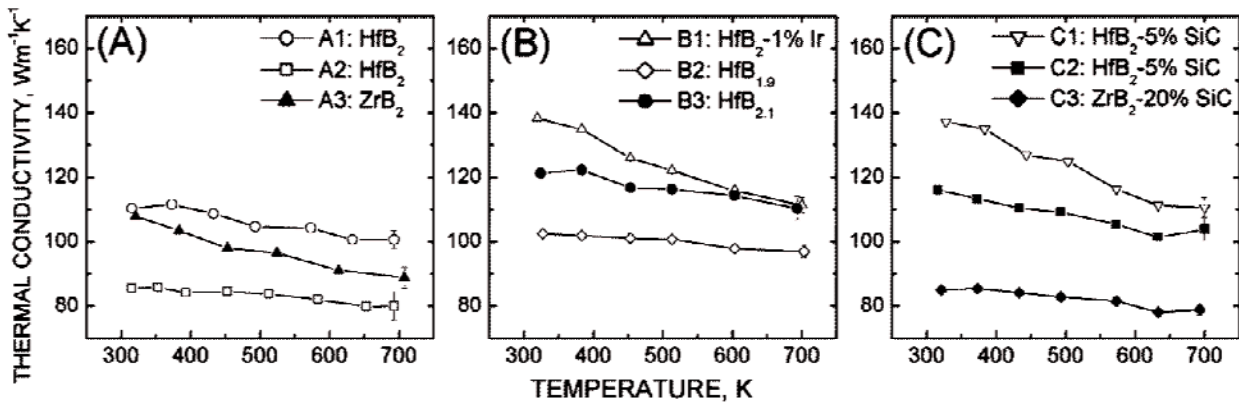


Fig. 6. Thermal conductivities calculated from the measured thermal diffusivities.

Table II. Specific heat function parameters of Equation (9).²⁴

	A	B	C	D
HfB ₂	366.52	0.03910	-1.150×10 ⁷	0
ZrB ₂ (<600K)	-34.70	2.068	-4.830×10 ⁵	-1.737×10 ⁻³
ZrB ₂ (>600K)	583.45	0.06455	-1.417×10 ⁷	5.131×10 ⁻⁶
Hf	127.23	0.04645	2.527×10 ⁵	1.681×10 ⁻⁹
B	1483.16	1.193	-7.003×10 ⁷	-2.992×10 ⁻⁴
Ir	118.58	0.03218	2.091×10 ⁵	-1.0×10 ⁻⁹
SiC	824.55	0.5819	-2.786×10 ⁷	-1.884×10 ⁻⁴

(4) Electrical Properties

Figure 7 shows the results of electrical resistivity measurements. Electrical resistivity increases linearly with increasing temperature for all samples. The data for each sample were fit by the equation

$$r = r_{298} [1 + \bar{\alpha}(T - 298)] . \quad (10)$$

The resulting values of the room temperature resistivity r_{298} and average temperature coefficient of resistivity, $\bar{\alpha}$, are listed in Table III. The values of r_{298} and $\bar{\alpha}$ for eight of the nine samples fall within the ranges $6\text{-}9 \mu\Omega\cdot\text{cm}$ and $3.5\text{-}4.3 \times 10^{-3} \text{ K}^{-1}$, respectively. The only exception is sample C3 which has a considerably higher room temperature resistivity ($17.0 \mu\Omega\cdot\text{cm}$) and lower average temperature coefficient of resistivity ($2.12 \times 10^{-3} \text{ K}^{-1}$) than all the other samples because of its high SiC content. The electrical resistivity of SiC is very high compared to the diborides, on the order of $10 \Omega\cdot\text{cm}$ for undoped material.²⁵

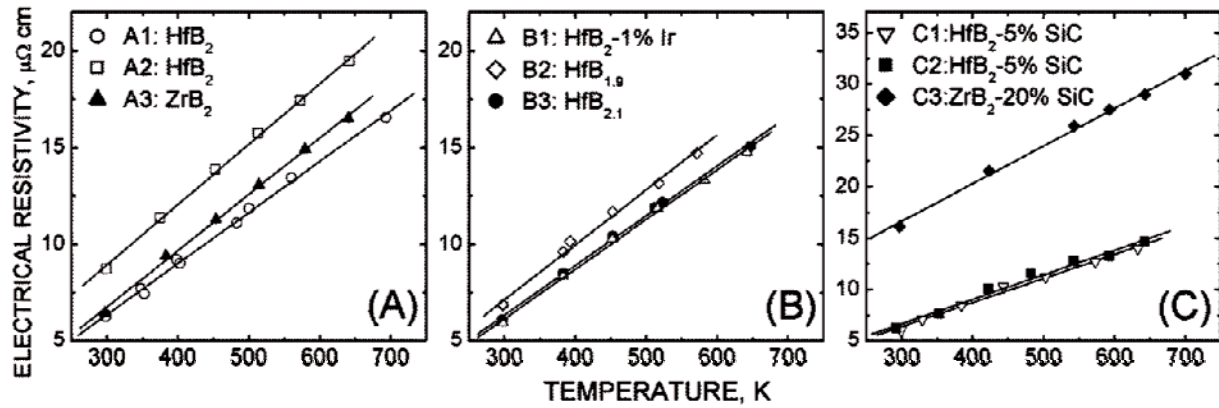


Fig. 7. Temperature dependence of the electrical resistivity; lines represent linear fits using Eq. (10).

The final three columns of Table III list the measured Hall coefficient and the derived charge carrier density and Hall mobility for each sample. The measured Hall coefficients are all negative confirming that electron transport dominates charge flow in these materials. All Hall coefficients fall between -1.3×10^{-3} and $-1.9 \times 10^{-3} \text{ cm}^3\text{C}^{-1}$, with C2 having the lowest value and C3 the highest value. The carrier densities are in the range $3.3\text{-}4.8 \times 10^{21} \text{ cm}^{-3}$ and Hall mobilities in the range $100\text{-}220 \text{ cm}^2\text{V}^{-1}\text{s}^{-1}$. Samples A1 and C1 have the highest Hall mobility. Sample C2 has the highest carrier concentration, while C3 has the lowest values of both Hall mobility and carrier concentration.

Table III. Electrical properties: resistivity at 298 K (r_{298}), temperature coefficient of resistivity ($\bar{\alpha}$), Hall coefficient (R_H), bulk carrier density (n_e), and Hall mobility (μ_e).

Group ID	r_{298} ($\mu\Omega\cdot\text{cm}$)	$\bar{\alpha}$ ($\times 10^{-3} \text{ K}^{-1}$)	R_H ($\times 10^{-3} \text{ cm}^3 \text{ C}^{-1}$)	n_e ($\times 10^{21} \text{ cm}^{-3}$)	μ_e ($\text{cm}^2 \text{ V}^{-1} \text{ s}^{-1}$)
A1	6.32	4.18	-1.60	3.9	220
A2	8.90	3.50	-1.64	3.8	170
A3	6.71	4.34	-1.55	4.0	200
B1	6.10	4.21	-1.76	3.5	250
B2	7.07	4.03	-1.63	3.8	200
B3	6.28	4.10	-1.46	4.3	210
C1	6.37	3.68	-1.55	4.0	220
C2	6.63	3.60	-1.30	4.8	180
C3	17.0	2.12	-1.89	3.3	100

(5) Electronic Contributions to Thermal Transport

The low electrical resistivity and the relatively high carrier density and Hall mobility of these diboride-based materials imply that electronic transport contributes substantially to heat transport. If the total thermal conductivity is taken as the sum of electronic and phonon contributions, $\lambda = \lambda_e + \lambda_{ph}$, and the electronic contribution is approximated by the Wiedemann-Franz relationship, it is possible to estimate the contribution of λ_e and λ_{ph} from the following:

$$\lambda_{ph}(T) = \lambda_{exp}(T) - \lambda_e(T) = \lambda_{exp}(T) - \frac{L_o T}{r_{298} [1 + \bar{\alpha}(T - 298)]} \quad (11)$$

The results of this estimation are shown in Fig. 8 where the ideal Lorenz Number, $L_o = 2.45 \times 10^{-8} \text{ W } \Omega \text{ K}^{-2}$, is used. Table IV list the room-temperature thermal and electrical conductivities along with the room-temperature Wiedemann-Franz ratio ($\lambda_e/\lambda_{exp} = 298\sigma L_o/\lambda_{exp}$) which is higher than 0.8 for all materials except C3. Because Eq. (11) is based on a number of physical simplifications, and additionally propagates the experimental uncertainties associated with both our thermal and electrical property measurements, the absolute numerical values of $\lambda_{ph}(T)$ have a large uncertainty. Nevertheless, it is evident from Table IV and Fig. 8, that in 300-700 K temperature range, electronic contributions to the thermal conductivity dominate over phonon contributions.

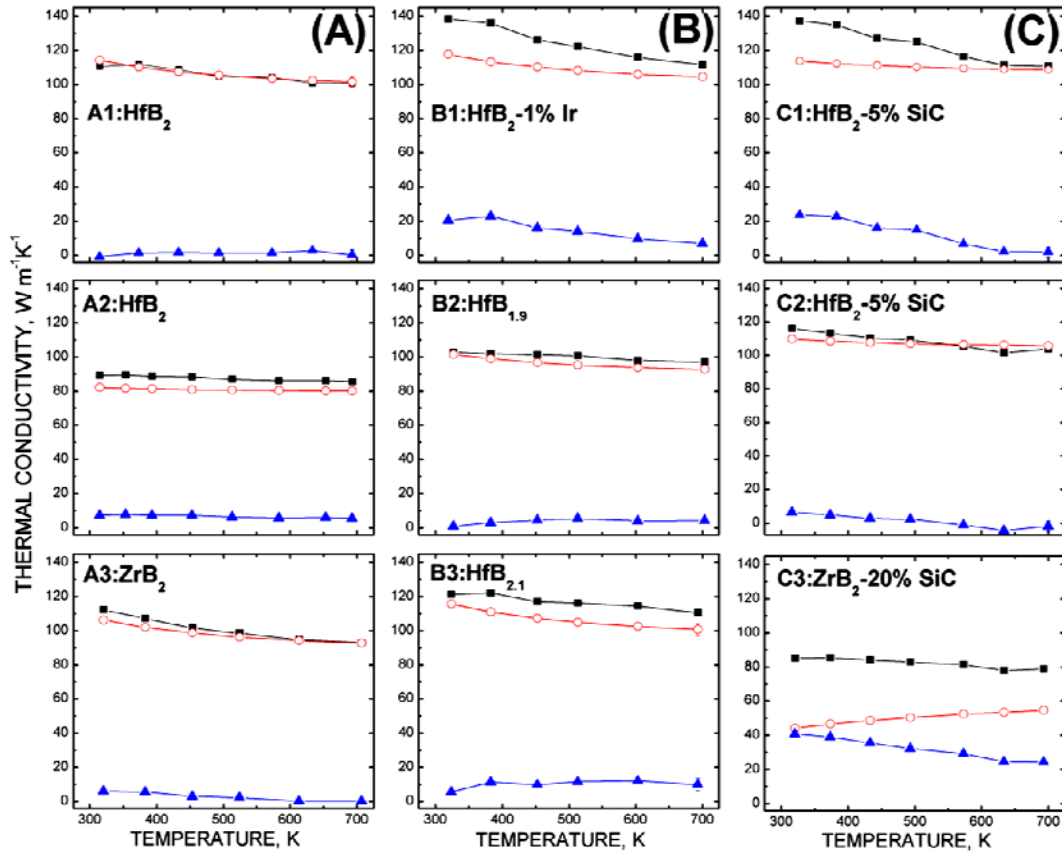


Fig. 8. Total (solid square), electronic (open circle), and phonon (solid triangle) thermal conductivities versus temperature; the electronic and phonon contributions are calculated from Eq. (11).

Table IV. Values of thermal conductivity (extrapolated), electrical conductivity, and the Wiedemann-Franz ratio at 298 K.

Group ID	λ_{298} (W m ⁻¹ K ⁻¹)	σ_{298} ($\times 10^7$ S m ⁻¹)	$\lambda_e / \lambda_{exp}$
A1	112	1.58	1.0
A2	89	1.12	0.92
A3	108	1.48	1.0
B1	138	1.62	0.86
B2	103	1.40	0.99
B3	125	1.58	0.92
C1	137	1.55	0.83
C2	118	1.50	0.93
C3	87	0.60	0.50

IV. Discussion

The measured thermal conductivities are in the upper range of values reported for polycrystalline materials with similar composition, both pure diborides and their mixtures with SiC.²⁶⁻²⁸ The effective (measured) thermal and electrical conductivities of polycrystalline ceramics depend on the individual constituent conductivities and the additional resistance to transport due to porosity and grain boundaries. Insight into these contributions can be gained through simple analytic models: the Brick Layer Model (BLM)²⁹ for interface resistance and the Effective Medium Approximation (EMA)³⁰ for averaging constituent properties. The BML formula approximates the effect of interface resistance on thermal conductivity by

$$\lambda = \left(\frac{1}{\lambda_{int}} + \frac{R_\lambda}{a} \right)^{-1}, \quad (12)$$

where R_λ is the thermal boundary resistance, a is the brick (grain) length, and λ_{int} is the intrinsic thermal conductivity. The EMA approach mixes constituent conductivities according to the implicit relationship

$$\sum_i v_i \frac{\lambda_i - \lambda_{eff}}{\lambda_i + 2\lambda_{eff}} = 0, \quad (13)$$

where v_i is the constituent volume fraction. Analogous equations apply for electrical conductivity.

For a composite in which porosity is isolated in a polycrystalline matrix of one major constituent, the two analytic models can be combined, with the BLM used to model the effect of grain boundary resistance on the matrix conductivity and the EMA model used to incorporate the effect of porosity.³⁰⁻³² The “intrinsic” thermal and electrical conductivities of ZrB₂ and HfB₂ are not known, but based on the measurements of Kinoshita et al.³³ for single crystal ZrB₂, reasonably representative values are $\lambda_{int} = 140 \text{ W m}^{-1} \text{ K}^{-1}$ and $\sigma_{int} = 2.17 \times 10^7 \text{ S m}^{-1}$. With these values fixed, setting $a = \bar{L}$, and the porosity $\varepsilon = 1 - \rho_{exp}/\rho_{the}$, the interfacial resistances can be adjusted until the computed effective conductivity matches the measured conductivity for the nominally pure diboride materials.

For the HfB₂ materials A1 and A2, the experimental room-temperature conductivities (Table IV) are matched with thermal interface resistances of 1.63×10^{-8} and $1.50 \times 10^{-8} \text{ m}^2 \text{ K W}^{-1}$, and electrical interface resistances of 1.65×10^{-13} and $1.77 \times 10^{-13} \text{ m}^2 \text{ S}$, respectively. Since these interface resistances vary little between A1 and A2, the reduced thermal and electrical conductivities of A2 can be satisfactorily explained by its higher porosity and higher grain boundary area per volume. A similar analysis of A3 gives lower thermal and electrical interface resistances of $0.60 \times 10^{-8} \text{ m}^2 \text{ K W}^{-1}$ and $0.76 \times 10^{-13} \text{ m}^2 \text{ S}$. The influence of grain size distribution on effective conductivity can be incorporated into the bricklayer model by setting $a = \bar{L} \exp(2.5(\sigma/\bar{L})^2)$.³⁴ The factor σ/\bar{L} lies within the range 0.4-0.6 for all our materials; making this substitution for a increases the derived interface resistances by factors of 1.67, 2.32,

and 2.25, for A1, A2, and A3, respectively. Typical thermal grain boundary resistances in polycrystalline ceramics fall in the range 10^{-7} to $10^{-9} \text{ m}^2 \text{ K W}^{-1}$ ^{29; 35-36}.

BLM/EMA analyses can also be performed for materials with additional constituents (e.g., Ir, SiC, excess Hf, excess B). Although “intrinsic” property inputs multiply, such modeling nevertheless suggests that the high thermal conductivities of C1 (HfB₂-5%SiC) and B1(HfB₂-1%Ir) are better explained by lower thermal boundary resistances than as the result of high thermal conductivity second phases.

It is interesting to compare samples B2, A1, and B3, which were manufactured from elemental powders mixed to the stoichiometries HfB_{1.9}, HfB₂, and HfB_{2.1}, respectively. All three samples have similar grain sizes and grain boundary area per volume. Sample B2 has the lowest thermal and electrical conductivities of the group, while B3 has a highest. However, enhanced electronic heat transport alone does not account for the entire difference in thermal conductivity between samples B2 and B3; the phonon contribution to thermal conductivity is also augmented in the higher boron content material (see Fig. 8 and Table IV.) A similar observation can be made for samples C1 and B1; their high thermal conductivities seem to derive in part from additional phonon contributions to heat transport, not from enhanced electronic contributions (Fig. 8 and Table IV.). The addition of minor constituents to diboride materials can exert a large influence on sintering behavior and chemistry at grain boundaries. We speculate that such additions, and the interface modifications they introduce, may influence the efficiency of electrical and phonon heat transport across grains boundaries in different ways.

Table V summarizes some published electrical property data for HfB₂- and ZrB₂-based materials. Similar to other investigators, we find high carrier mobilities for the diborides, with slightly lower Hall coefficients and slightly higher carrier densities for our SPS UHTC materials than typical in Table V. Our measured electrical resistivities are lower than most literature values for polycrystalline diborides manufactured by conventional hot-pressing methods. As shown in Fig. 8 and Table IV, a Wiedemann-Franz analysis for these SPS materials indicates that more than 80% of their total room-temperature thermal conductivity can be attributed to electronic contributions, except for sample C3 (ZrB₂-20%SiC) in which the contribution is 50%. Similar analyses presented in the literature vary widely. Zimmermann et al.²⁷ find electronic contributions of 50-60% for ZrB₂ and ZrB₂-30%SiC; Samsonov et al.³⁷ report ~65% for ZrB₂ and HfB₂; Tye and Clougherty²⁸ derive contributions ranging from 40 to 90% for a variety of HfB₂ and ZrB₂ materials.

The Wiedemann-Franz relationship also predicts an increasing electronic contribution to thermal conductivity with increasing temperature if the temperature coefficient of resistivity is below $\bar{\alpha} < 0.003356 \text{ K}^{-1}$ (i.e., $<1/298 \text{ K}$; see Eq. 11.) We measure $\bar{\alpha} < 0.003356 \text{ K}^{-1}$ for all our SPS samples except C3, whereas $\bar{\alpha} < 0.003356 \text{ K}^{-1}$ for most materials in Table V. Both increasing ($d\lambda/dT > 0$) and decreasing ($d\lambda/dT < 0$) thermal conductivities with increasing temperature are reported in the literature for ZrB₂- and HfB₂-based materials.^{26-27; 37-40} We find $d\lambda/dT < 0$ for all of our SPS UHTC materials. Researchers who have measured $d\lambda/dT > 0$ and have also made temperature-dependent resistivity measurements report $\bar{\alpha} < 0.003356$.^{27; 37} However, others have found $\bar{\alpha} < 0.003356$ together with $d\lambda/dT < 0$ ²⁸, as in our data for sample

C3. Since the phonon conductivity always decreases with increasing temperature, an additional mechanism is required to explain $d\lambda/dT > 0$. Gasch et al. have examined the closing of microcracks with increasing temperature as a possibility, but have found that an unsatisfactory explanation for various polycrystalline HfB_2 materials.²⁶ It seems that $\bar{\alpha} < 0.003356$ may be a necessary but insufficient condition for a diboride to exhibit increasing thermal conductivity with increasing temperature.

Table V. Published electrical property measurements for HfB_2 - and ZrB_2 -based materials: resistivity at 298 K (r_{298}), temperature coefficient of resistivity ($\bar{\alpha}$), Hall coefficient (R_H), bulk carrier density (n_e), and Hall mobility (μ_e).

Material	r_{298} ($\mu\Omega\cdot\text{cm}$)	$\bar{\alpha}$ ($\times 10^{-3} \text{ K}^{-1}$)	R_H ($\times 10^{-3} \text{ cm}^3 \text{ C}^{-1}$)	n_e^* ($\times 10^{21} \text{ cm}^{-3}$)	μ_e^* ($\text{cm}^2 \text{ V}^{-1} \text{ s}^{-1}$)	Ref.
(Polycrystalline)						
HfB_2	15.8	---	-1.7	3.7	110	41
HfB_2	16.6 [†]	---	-1.70	3.7	102	42
HfB_2	10.4	3.29	-1.80	3.5	170	43
HfB_2 -5%SiC	12.4	3.37	---	---	---	28
ZrB_2	7	---	-2.0	3.1	290	41
ZrB_2	16.6 [†]	---	-1.76	3.6	106	42
ZrB_2	7.8	1.3	---	---	---	44
ZrB_2	9.6	2.21	-1.90	3.3	200	43
ZrB_2	11.9	2.72	---	---	---	28
ZrB_2 (90% dense)	11.0	3.73	---	---	---	28
ZrB_2	22	2.06	---	---	---	27
ZrB_2 -20%SiC	10.3	4.42	---	---	---	28
ZrB_2 -30%SiC	24	2.52	---	---	---	27
(Single Crystal)						
ZrB_2	2.9 - 3.2 [†]	---	-1.2 ^{//} , -2.3 [⊥]	---	---	45
ZrB_2	4.6 [†]	---	---	---	---	33

* Computed from the tabulated r_{298} and R_H values assuming electrons are the charge carriers.

† Room temperature value, not from fitting.

$^{/\!/ \perp}$ parallel and perpendicular to hexagonal crystal axis

V. Conclusion

We investigated the thermal and electrical transport properties of spark-plasma-sintered HfB_2 - and ZrB_2 -based polycrystalline ceramics with different microstructures and minor additives, in the 300-700 K temperature range. The materials have high carrier mobilities, with somewhat lower Hall coefficients and higher carrier densities than values typically reported for diboride-based polycrystalline materials. The measured electrical conductivities are higher than most literature values for diboride ceramics manufactured by conventional hot-pressing methods. The thermal conductivities are in the upper range of values typically reported for pure diboride and diboride-SiC compositions and all show decreasing conductivity with increasing temperature. A Wiedemann-Franz analysis indicates that thermal conductivity is dominated by the electronic contribution to thermal transport. The variations in thermal and electrical conductivities between different HfB_2 samples are explained by their different porosities and grain boundary areas per volume. The high thermal conductivities of HfB_2 -5%SiC and HfB_2 -1%Ir samples are attributed to their low thermal boundary resistances. In samples of $\text{HfB}_{1.9}$, HfB_2 , and $\text{HfB}_{2.1}$, which have very similar microstructures, both thermal and electrical conductivities increase with boron content, a finding that deserves further investigation.

Acknowledgements

The authors thank Prof. Zuhair Munir of the University of California at Davis for performing the SPS processing in support of this work.

References

¹J. Fuller, Y. Blum, and J. Marschall, "Topical Issue on Ultra-High-Temperature Ceramics," *J. Am. Ceram. Soc.*, **91**[5] 1397-502 (2008).

²J. Fuller, G. Hilmas, W. Fahrenholtz, E. Corral, and L. Riegel, "Special Issue: Aerospace Materials for Extreme Environments," *Journal of the European Ceramic Society*, **30**[11] 2145-418 (2010).

³J. Fuller and M. Sacks, "Special Section: Ultra-High Temperature Ceramics," *J. Mater. Sci.*, **39**[19] 5885-6066 (2004).

⁴W. G. Fahrenholtz, G. E. Hilmas, I. G. Talmy, and J. A. Zaykoski, "Refractory Diborides of Zirconium and Hafnium," *J. Am. Ceram. Soc.*, **90**[5] 1347-64 (2007).

⁵T. H. Squire and J. Marschall, "Material Property Requirements for Analysis and Design of UHTC Components in Hypersonic Applications" *Journal of the European Ceramic Society*, **30**[11] 2239-51 (2010).

⁶U. Anselmi-Tamburini, Y. Kodera, M. Gasch, C. Unuvar, Z. A. Munir, M. Ohyanagi, and S. M. Johnson, "Synthesis and Characterization of Dense Ultra-High Temperature Thermal Protection Materials Produced by Field Activation through Spark Plasma Sintering (SPS): I. Hafnium Diboride," *J. Mater. Sci.*, **41** 3097-104 (2006).

⁷S.-Q. Guo, T. Nishimura, Y. Kagawa, and J.-M. Yang, "Spark Plasma Sintering of Zirconium Diborides," *J. Am. Ceram. Soc.*, **91**[9] 2848-55 (2008).

⁸R. Licheri, R. Orrù, C. Musa, and G. Cao, "Combination of SHS and SPS Techniques for Fabrication of Fully Dense ZrB₂-ZrC-SiC Composites," *Materials Letters*, **62** 432-35 (2008).

⁹W. S. Rasband, "ImageJ." in. National Institutes of Health, Bethesda, MD, 2008.

¹⁰Anon., "Standard Test Methods for Determining Average Grain Size." in. ASTM International, 1996.

¹¹J.-H. Han and D.-Y. Kim, "Analysis of the Proportionality Constant Correlating the Mean Intercept Length to the Average Grain Size," *Acta Metallurgica et Materialia*, **43**[8] 3185-88 (1995).

¹²C. S. Smith and L. Guttman, "Measurement of Internal Boundaries in Three-Dimensional Structures by Random Sectioning," *Transactions of the Metallurgical Society of AIME*, **197** 81- (1953).

¹³D. P. Almond and P. M. Patel, "Photothermal Science and Techniques." Chapman & Hall: New York, (1996).

¹⁴A. Salazar and A. Sánchez-Lavega, "Thermal Diffusivity Measurements Using Linear Relations from Photothermal Wave Experiments," *Review of Scientific Instruments*, **65**[9] 2896-900 (1994).

¹⁵A. Salazar, A. Sánchez-Lavega, and J. M. Terrón, "Effective Thermal Diffusivity of Layered Materials Measured by Modulated Photothermal Techniques," *J. Appl. Phys.*, **84**[6] 3031-41 (1998).

¹⁶M. Akoshima and T. Baba, "Thermal Diffusivity Measurements of Candidate Reference Materials by the Laser Flash Method," *International Journal of Thermophysics*, **26**[1] 151-63 (2005).

¹⁷M. Akoshima and T. Baba, "Study on a Thermal-Diffusivity Standard for Laser Flash Method Measurements," *International Journal of Thermophysics*, **27**[4] 1189-203 (2006).

¹⁸L. J. van der Pauw, "A Method of Measuring the Resistivity and Hall Coefficient of Lamellae of Arbitrary Shape," *Philips Technical Review*, **20** 220-24 (1958/1959).

¹⁹L. J. van der Pauw, "A Method of Measuring Specific Resistivity and Hall Effect of Disks of Arbitrary Shape," *Philips Research Reports*, **13**[1] 1-9 (1958).

²⁰B. Sundqvist, "Electrical Resistance of Nickel in the range 300-725K and 0-2GPa," *Physical Review B*, **38**[17] 12283-89 (1988).

²¹J. R. Davis, "ASM Specialty Handbook: Copper and Copper Alloys." in. ASM International, Materials Park, OH, 2001.

²²R. C. Weast, "CRC Handbook of Chemistry and Physics." in, **Vol. 60**. CRS Press, Inc., Boca Raton, FL, 1979-80.

²³R. G. Munro, "Material Properties of a Sintered α -SiC," *J. Phys. Chem. Ref. Data*, **26**[5] 1195-203 (1997).

²⁴A. Roine, "HSC Chemistry for Windows, Version 5.11." in. Outokumpu Research Oy, Pori, Finland, 2006.

²⁵W. D. Kingery, H. K. Bowen, and D. R. Uhlmann, "Introduction to Ceramics." John Wiley & Sons: New York, (1976).

²⁶M. Gasch, S. Johnson, and J. Marschall, "Thermal Conductivity Characterization of Hafnium Diboride-Based Ultra High Temperature Ceramics," *J. Am. Ceram. Soc.*, **91**[5] 1423-32 (2008).

²⁷J. W. Zimmermann, G. E. Hilmas, W. G. Fahrenholtz, R. B. Dinwiddie, W. D. Porter, and H. Wang, "Thermophysical Properties of ZrB_2 and ZrB_2 -SiC Ceramics," *J. Am. Ceram. Soc.*, **91**[5] 1405-11 (2008).

²⁸R. P. Tye and E. V. Clougherty, "The Thermal and Electrical Conductivities of Some Electrically Conducting Compounds," *Proceedings of the Fifth Symposium on Thermophysical Properties* 396-401 (1970).

²⁹D. S. Smith, S. Fayette, S. Grandjean, and C. Martin, "Thermal Resistance of Grain Boundaries in Alumina Ceramics and Refractories," *J. Am. Ceram. Soc.*, **86**[1] 105-11 (2003).

³⁰R. Landauer, "The Electrical Resistance of Binary Metallic Mixtures," *J. Appl. Phys.*, **23**[7] 779-84 (1952).

³¹C. Poulier, D. S. Smith, and J. Absi, "Thermal Conductivity of Pressed Powder Compacts: Tin Oxide and Alumina," *Journal of the European Ceramic Society*, **27** 475-78 (2007).

³²B. Nait-Ali, K. Haberko, H. Vesteghem, J. Absi, and D. S. Smith, "Thermal Conductivity of Highly Porous Zirconia," *Journal of the European Ceramic Society*, **26** 3567-74 (2006).

³³H. Kinoshita, S. Otani, S. Kamiyama, H. Amano, I. Akasaki, J. Suda, and H. Matsunami, "Zirconium Diboride (0001) as an Electrically Conductive Lattice-Matched Substrate for Gallium Nitride," *Japanese Journal of Applied Physics*, **40**[12A] L1280-L82 (2001).

³⁴Z.-Y. Deng, J. M. F. Ferreira, Y. Tanaka, and Y. Isoda, "Microstructure and Thermal Conductivity of Porous ZrO₂ Ceramics," *Acta Mater*, **55** 3663-69 (2007).

³⁵S. Fayette, D. S. Smith, A. Smith, and C. Martin, "Influence of Grain Size on the Thermal Conductivity of Tin Oxide Ceramics," *Journal of the European Ceramic Society*, **20** 297-302 (2000).

³⁶H.-S. Yang, G.-R. Bai, L. J. Thompson, and J. A. Eastman, "Interfacial Thermal Resistance in Nanocrystalline Yttria-Stabilized Zirconia," *Acta Mater*, **50** 2309-17 (2002).

³⁷G. V. Samsonov, B. A. Kovenskaya, T. I. Serebryakova, and E. Y. Tel'nikov, "Thermal Conductivity of Diborides of Group IV-VI Transition Metals," *High Temperature*, **10**[6] 1193-95 (1972).

³⁸M. M. Opeka, I. G. Talmy, E. J. Wuchina, J. A. Zaykoski, and S. J. Causey, "Mechanical, Thermal, and Oxidation Properties of Refractory Hafnium and Zirconium Compounds," *Journal of the European Ceramic Society*, **19** 2405-14 (1999).

³⁹M. Gasch, D. Ellerby, E. Irby, S. Beckman, M. Gusman, and S. Johnson, "Processing, Properties, and Arc Jet Oxidation of Hafnium Diboride/Silicon Carbide Ultra High Temperature Ceramics," *J. Mater. Sci.*, **39**[19] 5925-37 (2004).

⁴⁰F. Monteverde and L. Scatteia, "Resistance to Thermal Shock and to Oxidation of Metal Diborides-SiC Ceramics for Aerospace Application," *J. Am. Ceram. Soc.*, **90**[4] 1130-38 (2007).

⁴¹H. J. Juretschke and R. Steinitz, "Hall Effect and Electrical Conductivity of Transition-Metal Diborides," *Journal of Physics and Chemistry of Solids*, **4**[1-2] 118-27 (1958).

⁴²S. N. L'vov and V. F. Nemchenko, "Application of One-Band Concepts to the Diborides of Group IV Transition Metals," *Russian Physics Journal*, **11**[1] 36-38 (1968).

⁴³G. V. Samsonov, B. A. Kovenskaya, and T. I. Serebryakova, "Some Physical Characteristics of the Diborides of Transition Metals of Groups IV and V," *Russian Physics Journal*, **14**[1] 11-14 (1971).

⁴⁴M. Rahman, C. C. Wang, W. Chen, and S. A. Akbar, "Electrical Resistivity of Titanium Diboride and Zirconium Diboride," *J. Am. Ceram. Soc.*, **78** 1380-82 (1995).

⁴⁵J. Piper, "Galvanomagnetic Effects in Single-Crystal ZrB₂," *Journal of Physics and Chemistry of Solids*, **27** 1907-15 (1966).

APPENDIX 3

High-Enthalpy Test Environments, Flow Modeling and *in situ* Diagnostics for Characterizing Ultra High Temperature Ceramics*

Jochen Marschall

Molecular Physics Laboratory

SRI International, Menlo Park, California 94025

Douglas G. Fletcher

Mechanical Engineering

University of Vermont, Burlington, Vermont 05405

Abstract

Ultra-high temperature ceramic materials and composites under development as nose-tip and wing leading edge components for hypersonic flight vehicles must operate in extreme aerothermal heating environments. The performance of ultra-high temperature ceramics for this application is ultimately evaluated using high-enthalpy, long duration flow facilities that simulate the reactive gas environment encountered in hypersonic flight. In this paper, we describe the test environments generated by two types of these ground test facilities – subsonic inductively-coupled plasma tunnels and supersonic arc-jet tunnels – and discuss the important roles of computational fluid dynamics modeling and *in situ* optical diagnostics for interpreting test results from a materials science perspective.

1. Introduction

Transition metal borides and carbides, as well as their composites with various sintering aids and glass formers, are collectively known as ultra high temperature ceramics (UHTCs). The field of UHTC research has expanded substantially over the last decade, motivated by the unique potential of these ceramics for applications in extreme high-temperature, reactive environments.^{1,2} A central driver for UHTC research is the need for sharp leading edge and control surface components for future generations of hypersonic flight vehicles.³⁻⁵ Sharp leading edges enable vehicles with flight performance at hypersonic speeds (e.g., maneuverability, extended cross-range capability) that cannot be achieved with blunt body designs.^{6,7} The main hurdle for sharp vehicle designs is the severe aerothermal heating environment that acts on sharp leading edges. The concentrated combination of high

* This Appendix is an edited version of the manuscript published in The Journal of the European Ceramic Society, Vol. 30, 2010, pp. 2323-2336.

temperature and aggressive chemistry causes most materials to fail by melting, vaporization/sublimation, oxidation, ablation, spalling, or some combination of these processes.

While a battery of conventional mechanical and thermal tests aid in the development of UHTC materials, the performance of UHTCs intended for leading edge applications must ultimately be demonstrated in a representative aerothermal test environment. Such test environments are provided by arc-jet or inductively-coupled plasma (ICP) wind tunnels which expose test articles to high-enthalpy reactive gas flows. Tests of UHTC materials in arc-jet facilities have been reported in the scientific literature by Kaufman³, Metcalfe et al.⁸, Wuchina and Opeka⁹, Opila et al.¹⁰, Gasch et al.¹¹, Chamberlain et al.¹², Savino et al.¹³, Monteverde and Savino¹⁴, and Zhang et al.¹⁵ Tests of UHTC materials in ICP facilities have been reported by Ito et al.¹⁶, Marschall et al.¹⁷, and Playez et al.¹⁸

In this paper we discuss the test environments provided by these two types of plasma wind tunnel facilities. We highlight the coupling between the high-enthalpy reactive flow stream and the test specimen in determining UHTC material response to these environments. The importance of computational fluid dynamics (CFD) modeling of the free-stream and boundary layer flows is discussed, and the value of *in situ* diagnostics for documenting test conditions and monitoring UHTC evolution during testing is emphasized.

2. High-Enthalpy Test Environments

2.1. Plasma Wind Tunnel Facilities

The need for long-duration, high-enthalpy gas flows for the characterization and qualification of thermal-protection system (TPS) materials and components led to the development of plasma wind tunnel facilities for aerospace applications.¹⁹ A variety of different designs have been investigated and implemented for plasma wind tunnels but in general all facilities consist of an electrical power supply, an input gas supply, an arc-discharge or inductively-coupled heater section, a test section, and an exit gas handling system.

Arc discharge devices in which a current passes directly through a flowing gas were developed extensively in the USA because of their large energy deposition rates. Stable arc discharges are achieved in large length-to-diameter ratio heaters constructed of segmented metal elements and fitted with magnetically-spun electrodes. Various arc-jets are now in operation around the world, including facilities in the USA, Europe, and Asia.¹⁹ Direct-arc heating facilities can typically operate with large test gas mass flows and with pressures on the order of 1-2 MPa within the heater, enabling supersonic flow conditions in the test section. Most constricted-arc plasma facilities use conical nozzles to produce supersonic flows and can operate stably for long test times. The United States Air Force (USAF) arc-jet facilities have been developed to simulate aero-heating for ballistic atmospheric trajectories, while the National Aeronautics and Space Administration (NASA) arc-jet facilities have been tailored to simulate lower pressure trajectories associated with upper atmospheric and planetary entry.¹⁹

In ICP devices energy is coupled into the test gas flow inductively using high-frequency, high-power, high-voltage electrical supplies. Gases flow through a quartz tube (typically) in the

heater section and direct contact between the gas stream and hot metal surfaces is avoided. One advantage of the ICP design for materials science studies is that the free-stream is usually free of metal contaminants (e.g. copper) often found in arc-jet flows. Such contaminants may interfere with important chemical processes like oxidation, reactive volatilization and surface catalysis, or change important surface properties like the emittance. Although these devices were investigated in the USA,²⁰ they were developed extensively in Russia and large-scale ICP facilities are now also in operation in Europe and Asia.¹⁹ These devices can generate either subsonic or supersonic flows, however because of their more limited capability for supporting high gas pressures in the heater section, most ICP testing is done in the subsonic regime.

The test environments generated by these two types of facilities differ in significant ways, both from each other and from actual flight environments. No ground facility can reproduce all features of hypersonic flight accurately, because of physical constraints and operating envelope limitations. Choices for test conditions are usually made to match particularly important trajectory parameters like the anticipated peak heat flux, peak pressure, maximum heat load, etc. The extrapolation of ground test conditions to flight environments is an on-going area of concern and research^{21,22} and will not be addressed further here. Rather, we focus on differences between supersonic arc-jet and subsonic ICP environments as they impact TPS materials testing in general and UHTC testing in particular.

2.2. Test Conditions

Each plasma facility has its unique envelope of operation that limits the range of free-stream enthalpies that can be obtained. Together with the model size, shape, and chemical composition, the available free-stream enthalpy determines the heat flux that can be applied to a test specimen. Typically, the power delivered to the heater, the mass flow rate of the test gas, and the test section static pressure can be adjusted within prescribed ranges. The stagnation point conditions achieved for a particular combination of facility settings are then measured using a calibration probe (or probes) of the same geometry as the test sample, but fitted with a calorimeter to measure heat flux and a Pitot gauge to measure pressure. These calibration probes are usually made of copper and are water cooled.

Figure 1 illustrates the salient features of the flow interactions with a test specimen for the each type of facility. An important difference between supersonic arc-jet and subsonic ICP flows is the thermochemical state of the gas approaching the test article. Because of the relative fluid dynamic and chemical relaxation time scales in arc-jet facilities, gases exiting the nozzle and flowing into the test chamber are typically in a chemically frozen or non-equilibrium state. This means that the chemical composition of the free-stream gas may differ considerably from the thermodynamic equilibrium composition associated with the translational gas temperature. In supersonic arc-jet flows the interaction of the free-stream with the test article produces a bow shock in which the gas undergoes adiabatic compression. High energy intermolecular collisions heat the gas, depositing energy into a manifold of excited electronic, vibrational, and rotational states, and driving ionization and molecular dissociation processes. Behind the shock front, where the flow is subsonic, the residence time is now longer than typical chemical reaction times

and gases undergo thermal and chemical relaxation as they approach the boundary layer edge.²³ The gas temperature at the boundary layer edge may be 1000's of degrees hotter than the surface of the test specimen. As the gas flow passes through the boundary layer edge to the surface, chemical reactions change the gas composition further. However, the chemical and flow time scales in the boundary layer may be such that the gas interacting directly with the specimen is not in chemical equilibrium at the surface temperature.

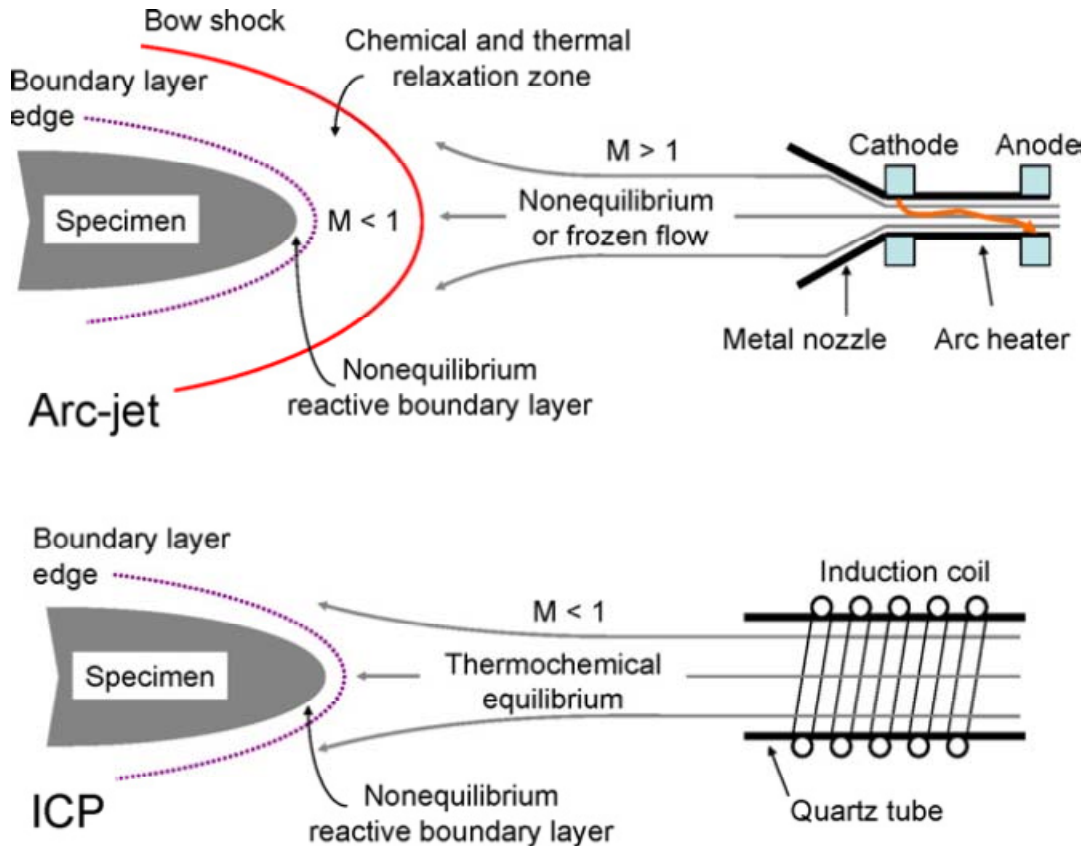


Fig. 1. Flow features for arc-jet and ICP free-streams interacting with a test specimen.

In contrast, in ICP facilities the flow path and timescales are typically such that gases can relax towards their thermochemical equilibrium state in the free-stream before reaching the boundary layer edge at the test article, making the prediction of the boundary layer edge composition much more straight forward.²² In a subsonic ICP flow, no bow shock is produced when the flow encounters the test specimen, but a reactive boundary layer is still formed. There is still a large temperature difference between the boundary layer edge and the specimen, and similar drivers for chemical non-equilibrium in the gases at the surface exist.²⁴

In supersonic arc-jet flows the pressure at the stagnation point of a test article is largely determined by the dynamic pressure of the flow stream, while in subsonic ICP flows the

stagnation pressure is largely determined by the static pressure in the test section because the dynamic pressure of the flow stream is small. The aerodynamic shear stresses exerted on model surfaces can be much higher in supersonic arc-jet flows than in subsonic ICP flows. While UHTC materials should have sufficient mechanical strength to withstand aerodynamic shear stresses, this may not be true for developing surface oxides. At sufficiently high temperatures in oxygen-bearing environments, many UHTC materials form glassy oxide phases (e.g., B_2O_3 and SiO_2) that permeate and seal porous poly-crystalline oxides (like ZrO_2 and HfO_2) creating a composite scale that acts as an efficient oxygen diffusion barrier.²⁵⁻²⁸ Aerodynamic shear stresses may redistribute low-viscosity glassy phases and alter the formation of such composite oxide scales.

Survey probe heat flux measurements are often reported as part of UHTC test conditions, but it is important to recognize that this heat flux is a *cold wall* heat flux to a *highly catalytic* surface, which is *not the same* as the heat flux delivered to a UHTC test specimen under identical test conditions. The convective heat flux to a specimen is driven by the temperature difference between the specimen surface and the hotter gas at the boundary layer edge. A UHTC surface will reach very high temperatures during an arc-jet or ICP test because it is not actively cooled. Because of the smaller temperature difference, the *hot wall* heat flux to a hot sample surface is always lower than the *cold wall* heat flux measured by a water-cooled survey probe. In addition, a UHTC surface may be less efficient than a copper surface at catalyzing the recombination of atomic species in the flow and will therefore experience less chemical heating from exothermic surface recombination reactions like $O + O \rightarrow O_2$, $N + N \rightarrow N_2$, and $O + N \rightarrow NO$.

The primary utility of cold wall heat flux measurements is to provide experimental calibration data to aid in the reconstruction of the free-stream enthalpy using CFD computations (discussed further below). Cold wall heat flux measurements are also useful for confirming the reproducibility of test conditions, but caution must be used when using free-stream enthalpy or cold wall heat flux to compare test conditions from supersonic arc-jet tests with subsonic ICP tests. Previous investigations have shown that three parameters must be replicated to match stagnation point convective heating conditions in ground test facilities: 1) stagnation point enthalpy; 2) stagnation (or impact) pressure; and 3) velocity gradient at the boundary layer edge.^{22,29} The velocity gradient is the rate that the velocity increases as gas flows around the test article. Thus, the convective heat transfer to the same test specimen exposed to arc-jet and ICP flows with similar free-stream enthalpy and total pressure values can be substantially different, owing to the large difference in velocity gradients between subsonic and supersonic test facilities. When differences in the velocity gradients in the two types of facilities are properly considered (for example, by scaling test article dimensions appropriately) similar boundary layer edge compositions and surface heat flux values can be obtained.^{22,29}

We note that the characterization of high-enthalpy flow test environments remains an active research area and that comparison of flow configurations and boundary layer environments can also be made on the basis of non-dimensional similarity parameters such as the Reynolds, Schmidt, and Damköhler numbers. The use of non-dimensional similarity parameters is a valid approach, but one practical aspect worth mentioning is that (with some work) the

stagnation enthalpy, stagnation pressure; and velocity gradient can be measured more easily than most non-dimensional similarity parameters in arc-jet and ICP test facilities.

From a materials science perspective, and particularly for studies of UHTC oxidation, the most relevant metrics for comparing different tests are the surface temperature, the stagnation point pressure, and the gas composition at the sample surface. This information is vital for associating physical changes in test specimens with specific environmental conditions, and for developing models of thermal and chemical material response. The first two quantities are routinely measured during arc-jet and ICP tests, but the gas composition at the surface – which can be influenced both by chemical and transport kinetics – is not currently experimentally accessible.

3. CFD Modeling

Since the chemical nature of the gas at the test specimen surface is not measured, a combination of facility data, calibration probe measurements and CFD modeling must be used to compute the gas composition at the specimen surface for each test run. This process involves two steps. First, CFD model inputs are adjusted until free-stream flow conditions result in computed heat flux and pressure values consistent with those measured using calibration probes; then the free-stream flow conditions are held fixed and the CFD model is used to compute the temperature drop and the changing gas composition through the boundary layer to the sample surface.

This procedure was described in detail for a recent series of UHTC oxidation tests run in the 1.2 MW Plasmatron facility at the von Karman Institute for Fluid Dynamics (VKI).¹⁷ The CFD codes used for this procedure are the VKI Boundary Layer Code^{24,30} and the VKI ICP Code^{31,32}, both of which use the PEGASE library to perform thermodynamic and transport property calculations.³³ The ICP code solves the time-averaged magneto-hydrodynamic equation at low Mach and low magnetic Reynolds numbers, assuming axisymmetric flow and local thermodynamic equilibrium, to simulate the flow inside the plasma torch and around the test article in the vacuum chamber. The Boundary Layer Code solves the boundary layer equations for an axisymmetric or two-dimensional, steady, laminar flow of chemically reacting gas over a catalytic surface, including thermal and chemical non-equilibrium. The temperature and velocity at the boundary layer edge are adjusted until the computed and measured heat flux agrees.

At NASA Ames Research Center, arc-jet flows are computed using the Data Parallel Line Relaxation (DPLR) code.³⁴ DPLR is a parallel multiblock finite-volume code that solves the Navier-Stokes equations including finite-rate chemistry and the effects of thermal non-equilibrium. The code is used to compute nonequilibrium expanding flow in the arc-jet nozzle and supersonic jet entering the test section, as well as the reacting flow around test articles.³⁵⁻³⁷ Thermodynamic properties are taken from NASA Glenn curve fits³⁸. Transport properties are computed using the self-consistent effective binary diffusion method³⁹ and expressions and mixing rules presented by Gupta et al.⁴⁰, together with collision integrals compiled by Wright et

al.^{41,42} Simulations are typically started at the nozzle throat assuming thermochemical equilibrium flow properties and some radial profile of enthalpy and mass flux. Facility and calibration data include measurements of the chamber pressure, mass flow rate, and test section pressure, calorimeter probe heat flux and pressure measurements. The total enthalpy of the arc-jet flow and its radial distribution are inferred from facility data and previous survey measurements. In the CFD reconstruction, these inferred values and distributions serve as the starting point for iterative adjustments to match computational predictions to the heat flux measured by the calibration probe.

The energy balance at the surface of a test article or calibration probe is the key relationship that couples the gas-phase and the solid material. For an environment free of gas radiation, the energy balance for any non-ablating/non-pyrolyzing material surface can be written as

$$q_{conv} + q_{chem} = q_{rad} + q_{cond} , \quad (1)$$

where the terms on the left hand side account for convective and chemical heating by the gas stream and those on the right hand side represent cooling by radiation and in-depth heat conduction. With some simplifying assumptions (a sensible gas enthalpy convective transfer coefficient representation, independent surface recombination of O and N atoms with equal catalytic efficiencies, negligible gas radiation) this equation can be expanded as

$$C_H [H_e(T_e) - H_s(T_s)] + \gamma'(T_s) \Delta E_{O_2} n_O \sqrt{\frac{RT_s}{8\pi M_O}} + \gamma'(T_s) \Delta E_{N_2} n_N \sqrt{\frac{RT_s}{8\pi M_N}} = \varepsilon \sigma T_s^4 - k(T_s) \frac{dT}{dx} \Big|_s \quad , \quad (2)$$

where C_H is the convective transfer coefficient; H_e and H_s are the gas enthalpies at the boundary layer edge and at the surface; ΔE_{O_2} and ΔE_{N_2} are molecular dissociation energies; n_O and n_N are atom number densities above the surface; M_O and M_N are molar masses; R is the universal gas constant; T is temperature; σ is the Stefan-Boltzmann constant; and x is the coordinate into the surface. Equation (2) also shows how the surface energy balance depends explicitly on temperature-dependant surface and bulk material properties: the total catalytic efficiency γ' , the emittance ε , and the thermal conductivity, k . The total catalytic efficiency is defined as $\gamma' = \gamma\beta$, where γ is the species recombination efficiency (the fraction of collisions with the surface that result in atom loss) and β is the energy accommodation coefficient (the fraction of exothermic reaction energy transferred to the surface).

In calibration measurements the right-hand side of Eq. (2) is measured directly using water-cooled calorimeters. Then CFD inputs are adjusted to reproduce this calibration heat flux measurement, usually with values of γ' fixed at 1 (a fully catalytic surface) and T_s fixed to a low temperature like 300 K (a cold wall). This process derives the convective transfer coefficient C_H and the boundary layer edge temperature T_e for a particular test condition, quantities that are then kept fixed in simulations seeking to reproduce surface temperatures subsequently measured during UHTC tests.

When q_{cond} is negligible, and with C_H , T_e , and T_s fixed, Eq. (2) shows that the energy balance is determined by γ' and ε through the chemical and surface radiation fluxes. (For sharp UHTC test articles, a thermal model of the heat transfer within the UHTC is likely required to evaluate q_{cond} . However for other configurations, like stagnation point testing with disk specimens in a flat-faced cylinder configuration, q_{cond} can be set to zero with minimal error.) If a numerical value is assigned to the surface emittance, the total catalytic efficiency can be adjusted iteratively until Eq. (2) is satisfied, and the gas composition at the surface is computed simultaneously. In practice, it is not straightforward to choose the “correct” value of emittance for a UHTC component at high temperature.¹⁷

As an illustrative example of the process described above, we show some results obtained for a recent series of stagnation point oxidation tests performed in the VKI Plasmatron on UHTC specimens of a hot-pressed ZrB₂ material containing 30 volume percent SiC (termed ZrB₂-30SiC).¹⁷ Tests were performed at static chamber pressures of 10⁴ Pa with an air mass flow rate of 16 g s⁻¹ over a range of Plasmatron powers from 150 to 210 kW.

The upper portion of Fig. 2 shows the cold wall heat flux measured by a calibration probe and the steady-state UHTC sample surface temperature measured using a two-color pyrometer during each test run. Both the cold wall heat flux and the specimen surface temperature increase with Plasmatron power as expected. The lower portion of Fig. 2 shows the hot wall heat flux for each test run computed from $q_{hw} = \varepsilon \sigma T_s^4$ with $\varepsilon = 0.90$ and $\varepsilon = 0.75$, assuming $q_{cond} \approx 0$. Both values of emittance are reasonable estimates for oxidized ZrB₂-SiC composites^{14,17,43}. Without an *in situ* method for determining the high-temperature emittance during testing, such a level of uncertainty (~15%) in emittance is unavoidable. Note that the hot wall heat fluxes are only about half of the corresponding cold wall heat fluxes, which suggests that the surface catalytic efficiencies of the oxidized UHTC surface must be low.

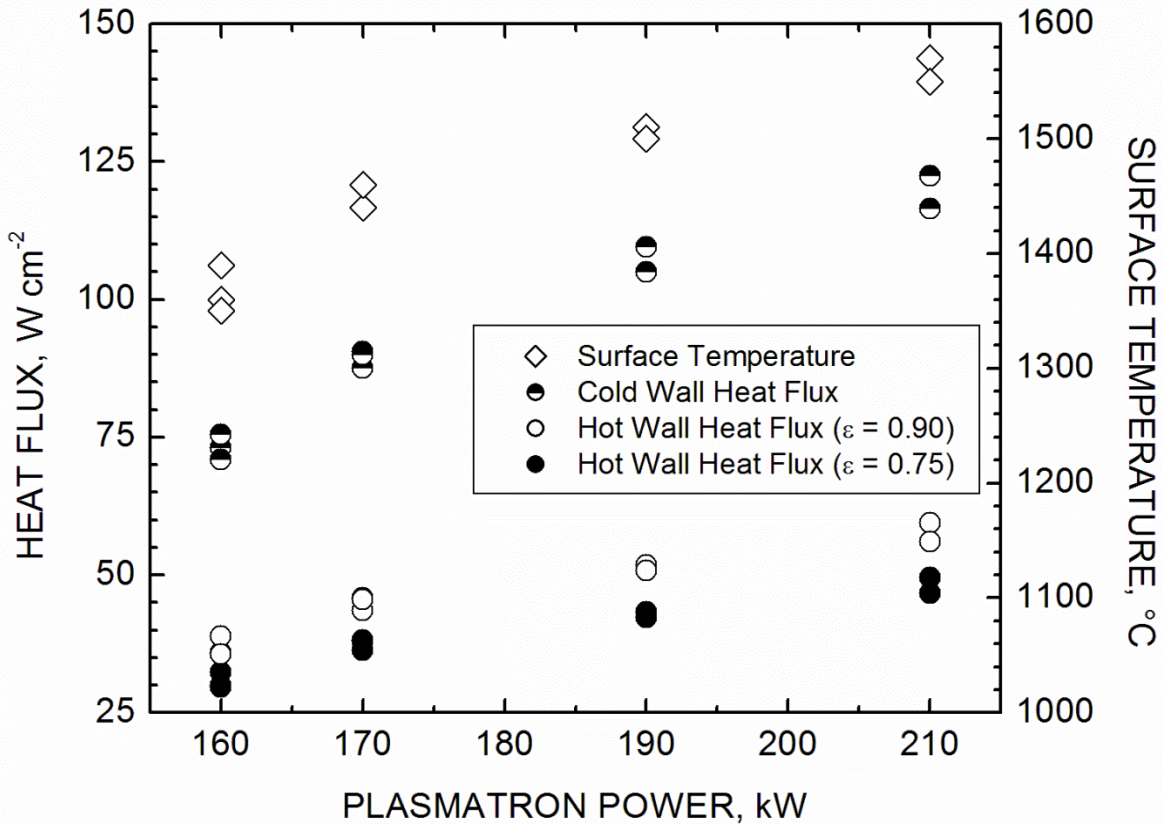


Fig. 2. Heat fluxes and surface temperatures versus Plasmatron power.¹⁷ The cold wall heat flux is measured by a calibration probe and the sample surface temperature is measured by a two-color pyrometer during each test run. The hot wall heat fluxes are estimated from $q_{hw} = \varepsilon \sigma T_s^4$ with $\varepsilon = 0.90$ and $\varepsilon = 0.75$, assuming $q_{cond} \approx 0$.

Figure 3 plots the total catalytic efficiency obtained for each test condition from the surface energy balance constraint, for values of $\varepsilon = 0.90$ and $\varepsilon = 0.75$. The derived catalytic efficiencies are much less than 1 consistent with a surface of low catalytic activity. Catalytic efficiencies derived for $\varepsilon = 0.90$ are 2 to 6 times higher than those for $\varepsilon = 0.75$. Thus uncertainties in emittance become amplified in derived catalytic efficiencies.

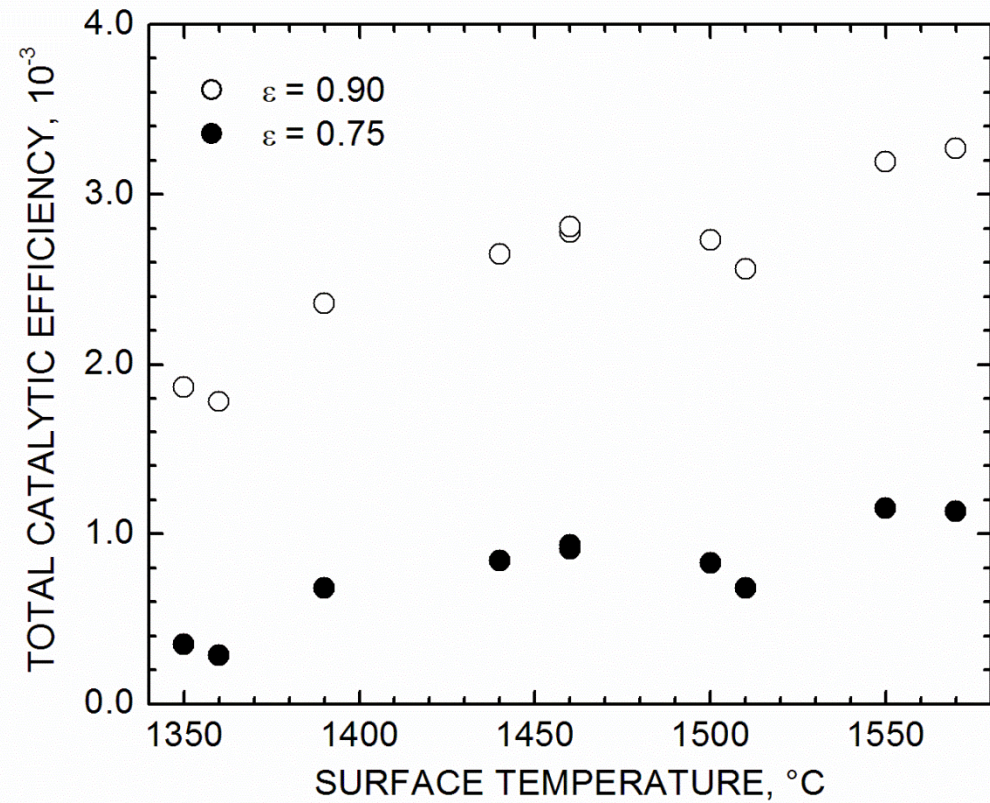


Fig. 3. Recombination efficiency versus surface temperature calculated for surface emittances of 0.75 and 0.90.¹⁷ The total catalytic efficiencies for $O + O$ and $N + N$ are assumed identical.

Figure 4 shows the calculated number densities of O , N , N_2 , O_2 , and NO at the UHTC surface for emittance values of 0.90 and 0.75. N_2 , O and N (in that order) are the dominant species with number densities around 10^{23} molecules per cubic meter; the number densities of O_2 and NO are about 2 orders of magnitude smaller. Atomic oxygen number densities are relatively unaffected by the choice of emittance values, but atomic nitrogen number densities computed for $\epsilon = 0.90$ are only 55 to 75% of the magnitudes computed for $\epsilon = 0.75$. The number densities of the minor species are larger for $\epsilon = 0.90$ than $\epsilon = 0.75$, by factors of about 3 to 7 for O_2 and about 2 to 3.5 for NO .

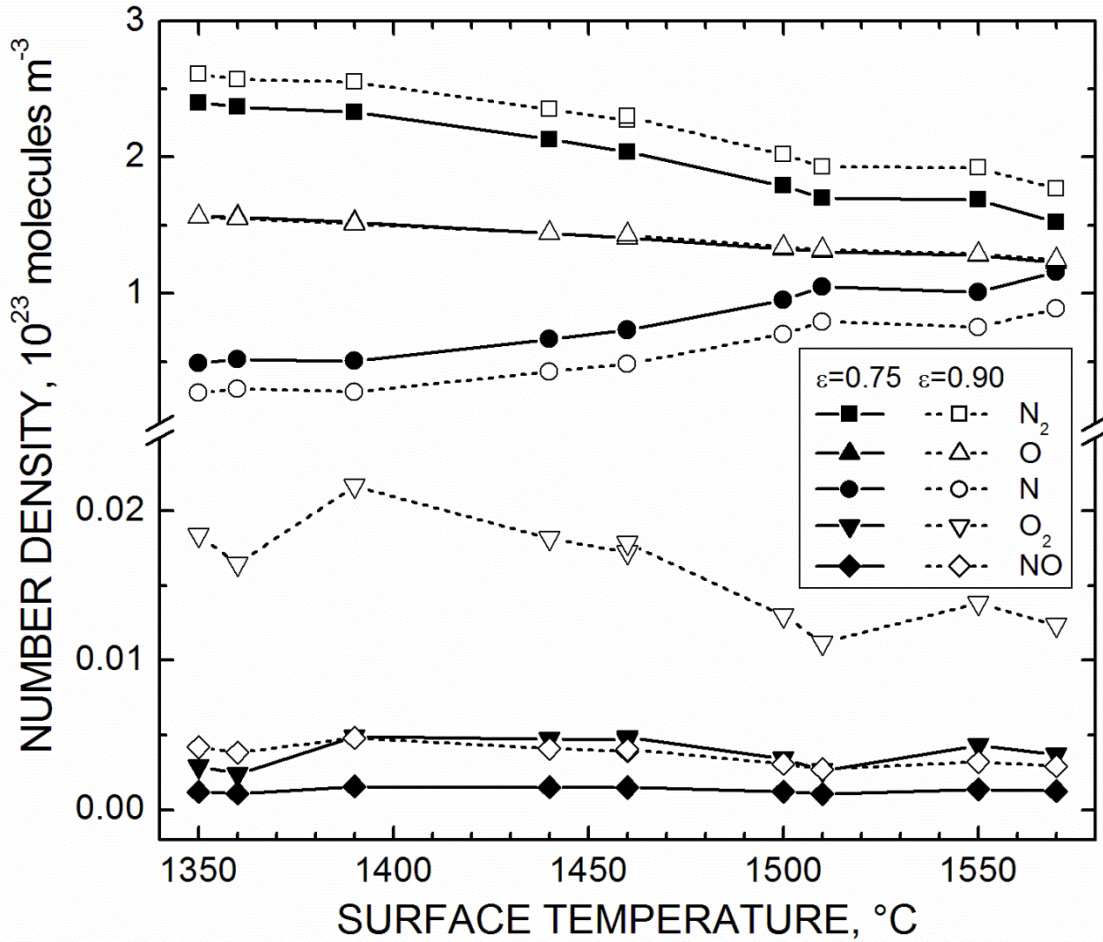


Fig. 4. Number densities at specimen surfaces versus surface temperature, computed for surface emittances of 0.75 and 0.90.

As this example demonstrates, considerable uncertainties can propagate into CFD-derived quantities like catalytic efficiency and surface gas composition, by errors in experimental measurements and material properties. Additional, and hard to quantify, error is also undoubtedly present in the details of the formulations, assumptions, solution procedures, and the chemical, transport and thermodynamic data employed in particular CFD codes. Nevertheless, CFD modeling is a crucial element of UHTC testing, because it offers the best tool currently available for evaluating the state of the gas interacting directly with the test surface specimen. It is also the only practical way to estimate quantities like the surface shear stress or to map out changes in gas composition over the surface of more complex 3-dimensional UHTC test articles.

We note that most published accounts of UHTC testing in arc-jet or ICP facilities have not reported quantitative estimates of the gas composition at the sample surface during testing. From a materials science perspective, this makes the comparison of different experiments problematic and the construction of materials response models more difficult. The value of UHTC arc-jet and ICP test results would be greatly increased if surface gas compositions, and the numerical procedures used to estimate them, were routinely reported. Further benefits would

result from measurements of boundary layer gas compositions and gradients, as discussed in the following section.

4. Optical Diagnostics

In this section we examine different optical techniques for obtaining information about the test environment and the evolution of UHTC specimens exposed to high-enthalpy flows.

4.1. Surface Radiometry

Surface temperature is perhaps the most important quantity required for the interpretation of test results. Surface temperatures are typically measured *in situ* by collecting thermal radiation emitted by the hot specimen using one-color or two-color radiometers. One-color radiometers collect radiation over a single wavelength range, while two-color radiometers collect radiation over two wavelength ranges (which may overlap). Both types of radiometers are calibrated as a function of emission temperature using blackbody radiation sources (special furnaces with an effective normal emittance approaching 1). One-color radiometers require knowledge of the specimen emittance over the detection wavelength range to convert radiation intensity to surface temperature. Two-color radiometers only require that the ratio of emittance values for the two detection ranges be known; for a surface with wavelength-independent emittance this ratio is 1. Typical experimental issues include transmittance losses due to windows, interference by absorbing gases, parasitic collection of reflected light, and geometric limitations for viewing the sample surface. Single-color radiometers typically respond to the average temperature in the field of view, while two-color radiometers tend to reflect the peak temperature in the field of view. Facility geometry usually dictates that specimen surfaces be viewed at non-normal incidence, enlarging the surface area seen by the radiometer. The possibility of non-uniform surface temperatures in the field of view must be considered for UHTC specimens with small stagnation regions like sharp wedges or cones.

Radiometry can also be used to obtain information about the emittance of UHTC specimens at high temperature. Laboratory measurements of UHTC emittance at high temperature are difficult and rare. The emittance measurements of Scatteia et al. on various UHTC composites (ZrB_2 -15SiC, ZrB_2 -15SiC-2MoSi₂, and ZrB_2 -15SiC-10HfB₂) are notable in this regard.^{43,44} Scatteia et al. have also demonstrated how UHTC emittance is influenced by surface finish and oxidation. Because it may be difficult to reproduce oxidized UHTC surfaces in the laboratory that are the same as those formed in the low-pressure, highly-dissociated oxygen environments of arc-jet and ICP flows, *in situ* measurements would be preferred.

If both one- and two-color radiometers are trained on the same surface location, surface temperature can be measured using the two-color instrument and, with the surface temperature known, the *in situ* emittance can be derived from the one-color instrument. Such a procedure was used by Monteverde and Savino¹⁴ to find $\varepsilon \approx 0.9$ for a hot-pressed ZrB_2 -15SiC composite during testing in a 80 kW plasma torch. This type of measurement could in principle be done using a single instrument, by calibrating and collecting both channels of a two-color radiometer.

A further extension of this procedure would be the use of a spectral radiometer to capture wavelength-resolved emission intensity over a broad wavelength range. The captured intensity curve is fit by the Planck blackbody radiation function, $E_b(\lambda, T)$, convoluted with a wavelength-dependent emittance, yielding both surface temperature and emittance values. Spectral radiometers are expensive instruments and their application in arc-jet or ICP testing of UHTC materials has not yet been reported.

Emittance is a function of wavelength, emission direction, and temperature. The surface energy balance requires the total hemispherical emittance – the emittance averaged over all wavelengths and emission directions – as input, where it plays a crucial role in the determination of surface catalytic efficiency and thus the computed gas-phase species concentrations above the surface. The emittance obtained by Monteverde and Savino¹⁴ yields a directional value valid over the wavelength range of their one-color radiometer. The direct use of this value in the surface energy balance implies assumptions of wavelength independence (a gray surface) and directional independence (a diffuse surface) which may not be true. Extension of this method using a spectral radiometer would produce a wavelength-dependant directional emittance that can be averaged over wavelength to yield a total, directional emittance value. However, some assumptions or approximations would still have to be made about the relationship between total directional and total hemispherical emittance before this derived value could be used in the surface energy balance. Since it does not seem possible to make a total hemispherical emittance measurement *in situ*, the best available alternative is probably the extrapolation of *in situ* emittance measurements with the directional and/or spectral dependencies documented in pre- and post-test laboratory measurements.

4.2. Gas Emission Spectroscopy

The radiation emitted by gases in the free-stream or in the near-surface region of test specimens contains information about the species present. Atoms and molecules emit radiation when they transition from higher to lower energy states. Each species has a unique set of energy levels and the energies of emitted photons correspond precisely to differences between these levels. Emission spectroscopy collects this emitted light and disperses it by wavelength, generating spectra with characteristic intensity features (atomic lines and molecular bands) that can be associated with individual species. Emission is a path-integrated measurement technique without spatial resolution along the light collection axis. Reconstruction of the spatial distribution of emission requires measurements along multiple axes and/or assumptions of symmetry together with a mathematical procedure known as an Abel inversion.⁴⁵ Further complications ensue if the gas is optically thick and significant re-absorption of emitted radiation occurs along the collection axis.

During the Plasmatron testing of hot-pressed ZrB₂-30SiC materials described in Section 3 above, prominent bluish-green emissions were observed around the test articles. These emissions first appeared and intensified as the sample temperature increased, then reached a plateau, and finally decreased in intensity at longer test times. Follow-on tests were performed in which emission spectra were collected directly adjacent to the specimen surface as a function

of test time. Light was captured through an aperture, focused onto the end of an optical fiber by a spherical mirror, and transmitted to a spectrometer with a wavelength range of 200 to 1100 nm and a resolution of 0.25 nm. Spectra were collected at 1 Hz during the test.

These measurements confirmed that the visible emission originated from electronically-excited BO and BO₂ molecules, and in addition detected ultraviolet emission associated with atomic boron. An example of these spectra is shown in Fig. 5, which plots background-subtracted raw signal against emission wavelength (background subtraction removes N₂⁺ emissions originating from the Plasmatron free-stream). The band head positions for the BO ($A^2\Pi \rightarrow X^2\Sigma^+$) and BO₂ ($A^2\Pi_u \rightarrow X^2\Pi_g$) systems are from Spalding et al.⁴⁶ and the B ($^2S_{1/2} \rightarrow ^2P_{1/2,3/2}$) doublet was identified from the NIST Atomic Spectra Database.⁴⁷ Since all boron species must originate from ZrB₂, emission spectroscopy in this case provides an *in situ* monitor for the oxidation of the UHTC composite and the volatilization of boron from the resulting oxide scale.

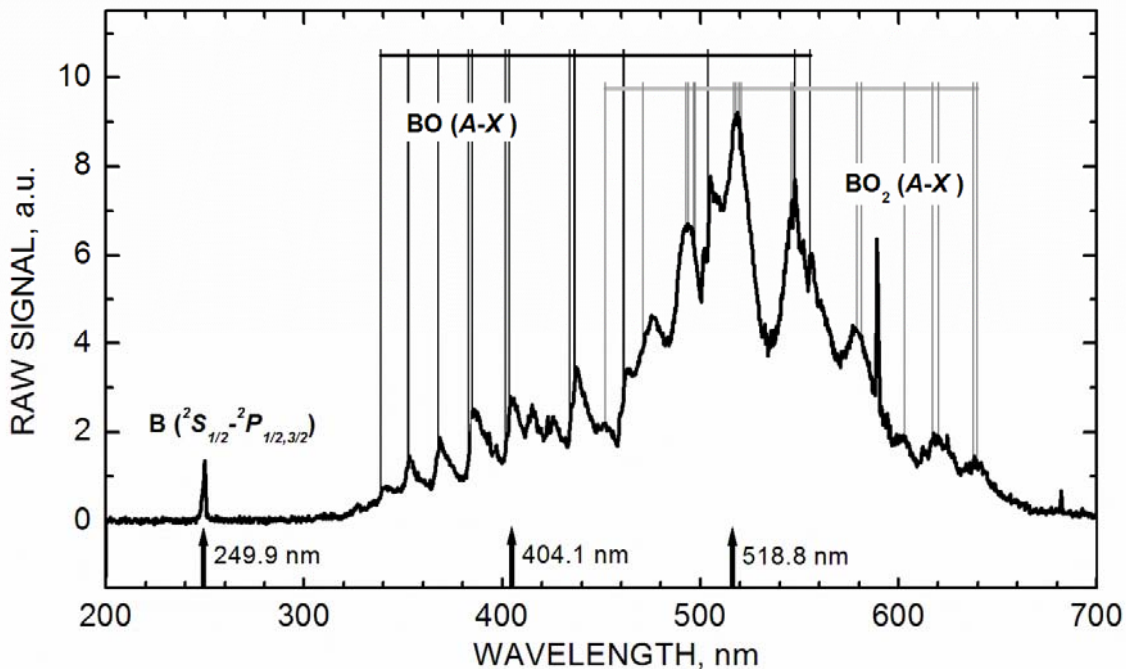


Fig. 5. Raw signal versus emission wavelength 55 seconds after injection of sample into the freestream. Background emissions from the Plasmatron freestream have been subtracted to remove contributions from the N₂⁺ band system. The strong line at 589 nm can be assigned to sodium. The bandhead positions for BO and BO₂ are from Spalding et al.⁴⁶ and atomic lines were identified from the NIST Atomic Spectra Database.⁴⁷ Arrows indicate the wavelengths used to monitor B, BO, and BO₂ as a function of test time.

UHTC composites containing both ZrB₂ and SiC oxidize to form complex oxide scales with an outer glassy layer rich in silica and an inner layer depleted of SiC. The structure of these oxide scales has been extensively investigated with post-test analytic techniques (microscopy, X-

ray diffraction, chemical analysis)^{26,48,49}, and their formation hypothesized in terms of transport processes and thermodynamic arguments.^{27,28}

In dissociated-oxygen environments, the passive oxidation of zirconium diboride forms zirconia and boron oxide, and the passive oxidation of silicon carbide forms silica and carbon monoxide:



The oxidation rate of ZrB_2 at moderate temperatures (below 1000°C) is significantly faster than the oxidation rate of SiC . Therefore the initial oxide scale is expected to be predominantly B_2O_3 . Amorphous B_2O_3 has a very low softening temperature (~560 to 630°C)⁵⁰ and liquid B_2O_3 seals the surface slowing inward oxygen transport. At higher temperatures, the SiC oxidation rate increases and the oxide scale becomes a borosilicate glass. However liquid B_2O_3 has a much larger vapor pressure than silica and boron oxides are predicted to volatilize preferentially from the oxide surface leaving a silica rich glass. As the glassy scale thickens and becomes more silica rich, inward oxygen diffusion slows further and oxygen concentrations at the reaction interface decrease. Under these conditions active SiC oxidation becomes favored over ZrB_2 oxidation, slowing B_2O_3 production and leading to the formation of a porous SiC -depleted sub-layer via:



Gaseous SiO formed at the bottom of the SiC -depleted layer diffuses to the top of that layer where it is thought to condense, augmenting the glassy top scale from below.

In detail, this process is quite complicated, involving heterogeneous media, transitions between different controlling chemistries, the growth of multiple oxide layers, moving interfaces, changing glass compositions, evolving transport properties, etc. However, a simple “shape function” for the expected time variation of boron species volatilization can be constructed based on the premise that boron oxide is formed by reaction (3) at the bottom of the glassy scale and diffuses through the scale to the surface where it evaporates according to a Hertz-Langmuir relationship. The diffusion and evaporation fluxes can be written in terms of the boron oxide concentrations at the reaction interface, $C_{\text{B}_2\text{O}_3,i}$, and the outer surface, $C_{\text{B}_2\text{O}_3,s}$, as

$$J_{B_2O_3,dif} = D_{B_2O_3} \frac{C_{B_2O_3,i} - C_{B_2O_3,s}}{\Delta_{glass}} \quad (6)$$

$$J_{B_2O_3,ev} = \frac{P_{B_2O_3,v}}{\sqrt{2\pi M_{B_2O_3} RT}} \frac{C_{B_2O_3,s}}{[\rho/M]_{glass}} \quad . \quad (7)$$

These expressions can be combined by assuming diffusion and evaporation fluxes are in quasi-steady-state at any time:

$$J_{B_2O_3,ev} = \frac{C_{B_2O_3,i}}{\frac{\sqrt{2\pi M_{B_2O_3} RT} [\rho/M]_{glass}}{P_{B_2O_3,v}} + \frac{\Delta_{glass}}{D_{B_2O_3}}} \quad . \quad (8)$$

Both the vapor pressure and the diffusion coefficient are presumed to follow Arrhenius dependencies on temperature: $P_{B_2O_3,v} \propto \exp(-E_v/RT)$ and $D_{B_2O_3} \propto \exp(-E_D/RT)$. If parabolic scale growth is assumed, $\Delta_{glass} \propto \sqrt{t}$, and if falling boron oxide production with growing scale thickness is approximated by an inverse power law, $C_{B_2O_3,i} \propto t^{-n}$, the following shape function for the temperature and time dependencies of the boron oxide vaporization flux results:

$$J_{B_2O_3,ev} \cong \frac{k_1 t^{-n}}{\sqrt{T} \exp(E_v/RT) + k_2 \sqrt{t} \exp(E_D/RT)} \quad , \quad (9)$$

where k_1 , k_2 , n , E_v , and E_D are constants.

Figure 6 compares the experimental temperature and emission signal history (in the left-hand panel) collected during a Plasmatron test to some representative volatilization profiles (in the right-hand panel) computed by Eq. (9) for a piecewise linear temperature history and several numerical choices of constants. The experimental emission signals were collected at the wavelengths indicated in Fig. 5; the experimental temperature was collected by a radiometer with a low temperature cut-on of $\sim 1100^\circ\text{C}$. E_v was fixed at a low 10 kJ/mole on the premise that boron diffusion in high temperature amorphous or liquid silica is very fast. E_D was adjusted to 320 kJ/mole to reproduce the sharp rise in boron emission signatures observed between 40 and 50 seconds. The activation energy predicted by thermodynamic calculations for the vapor pressure of B_2O_3 over liquid boron oxide is closer to 380 kJ/mole^{25,51}. The decay of the shape

function with time is controlled by the exponent n . Computations are shown for $n = 0, 0.5$ and 1.0 , with k_2 fixed to 10^{14} and k_1 adjusted to maintain similar peak magnitudes for all profiles and to put the shape function on the same (arbitrary) scale as the emission data.

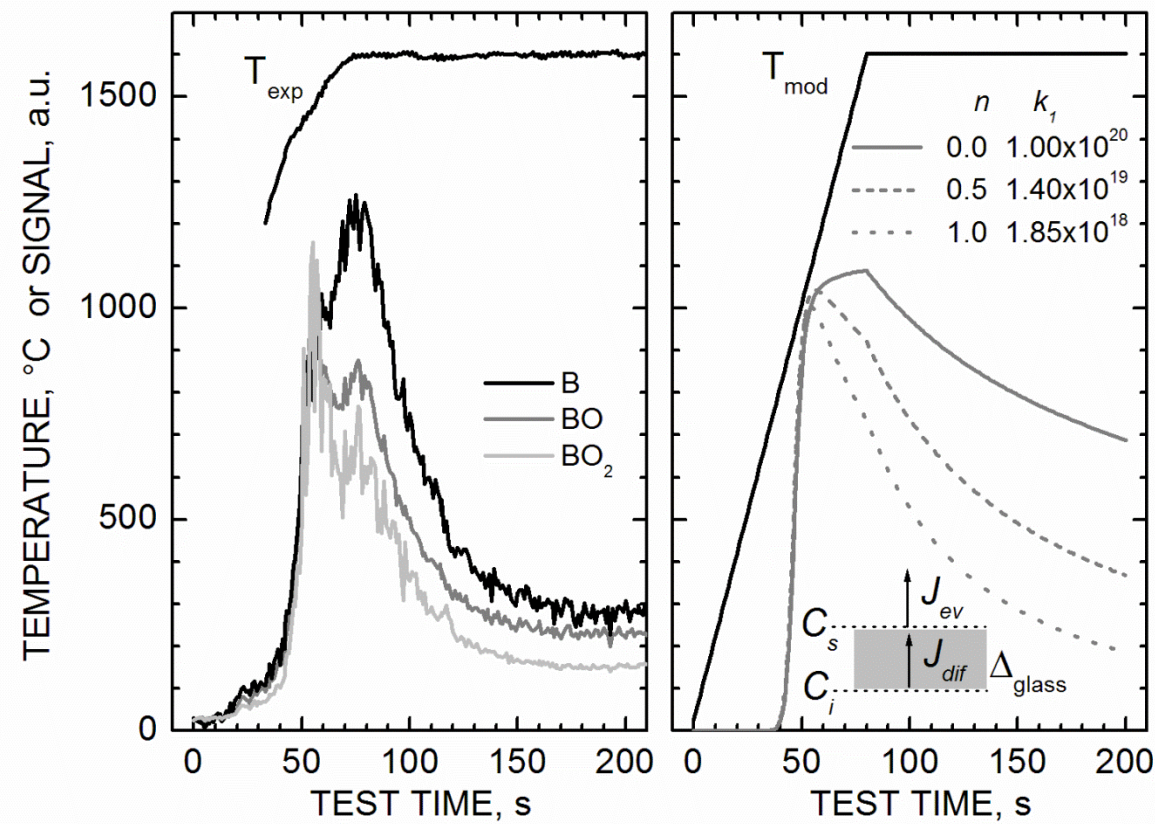


Fig. 6. Experimental temperature and emission signal history collected during a Plasmatron test of a hot-pressed $\text{ZrB}_2\text{-30SiC}$ specimen (left-hand panel) and representative volatilization profiles computed by Eq. (9) (right-hand panel). Emission was collected at the three wavelengths indicated in Fig. 5; the radiometer cut-on temperature was $\sim 1100^{\circ}\text{C}$. The B_2O_3 fluxes and concentrations leading to the shape function model are illustrated in the right-hand panel. Shape functions were computed with $k_2 = 10^{14}$, $E_v = 320$ kJ/mole, and $E_D = 10$ kJ/mole, and the values of n and k_1 listed on the figure.

In general this very simple model captures the qualitative trends seen in the emission data quite well. The largest exponent ($n = 1$) seems to reproduce the relatively steep emission signal decay the best. This is consistent with the idea that the concentration of B_2O_3 produced at the reaction interface should vary inversely with time *at least as fast* as the scale grows and probably faster as the decreasing oxygen pressure at the interface begins to favor active SiC oxidation over ZrB_2 oxidation.

At higher temperatures (above $\sim 1750^{\circ}\text{C}$), the vapor pressure of silica increases significantly and a similar process of volatilization from the UHTC oxide scale should lead to Si-containing species in the gas phase. Hirsch et al.⁵², Altman et al.⁵³, and Jentschke et al.⁵⁴ have monitored Si atom densities in front of C/C-SiC composites exposed to nitrogen-oxygen plasma flows, using high-resolution spectroscopy of Si I multiplet emissions in the 250-253 nm range. Herdrich et al.⁵⁵ observed Si emission near 252 nm and 288 nm while testing SiC specimens in oxygen-nitrogen plasmas, and also captured emission from SiO_2 molecules near 423 nm. Emission from SiO molecules was not reported in any of these studies, which is surprising given that reaction mechanism (5) should have been operating under some of the test conditions reported.

4.3. *Laser Induced Fluorescence*

Laser induced fluorescence (LIF) is a species selective, non-intrusive diagnostic that has been widely applied for the characterization of combustion and plasma environments.^{56,57} A pulsed, tunable laser source is used to generate monochromatic light at a unique atomic or molecular absorption wavelength. The absorbed photon energy excites the target species to a higher electronic energy level, from which it subsequently decays to a lower energy level (or levels) emitting radiation at a characteristic wavelength (or wavelengths).

One advantage of the LIF technique is that ground-state species populations can be probed, whereas emission spectroscopy detects only electronically-excited species. Even at relatively high temperatures, the ground electronic state populations typically predominate over the populations in higher electronic levels. Another advantage of LIF is that spatially resolved measurements are more easily made and interpreted than by emission spectroscopy, since the fluorescence collection optics field-of-view and the excitation laser beam axis can be independently oriented to intersect at a desired location, as shown schematically on the left side of Fig. 7. Generally speaking LIF detection works best for light atoms and diatomic molecules.

Applications of LIF to plasma stream characterization typically involve measurement of three variables: translational temperature, convective velocity, and species concentration. Air and nitrogen plasma species probed by LIF have included O atoms, N atoms, and nitric oxide (NO).⁵⁸⁻⁶² For NO, single-photon excitation in either the ultraviolet γ band ($A \leftarrow X$) or β band ($B \leftarrow X$) is possible. However, the large energy level spacing of the oxygen and nitrogen atoms requires a two-photon excitation scheme, and the excitation cross sections are correspondingly smaller.⁶³⁻⁶⁶ The energy levels involved in common two-photon excitation schemes for atomic oxygen and nitrogen are shown in the center and right side of Fig. 7. Atomic nitrogen is a useful target species for highly dissociated air or nitrogen plasmas, because its concentration is a sensitive indicator of the degree of plasma dissociation.^{58,59} Atomic oxygen number densities are critical for quantifying both passive and active surface oxidation processes. Both atomic species are involved in exothermic surface recombination processes that can contribute substantially aerothermal heating.

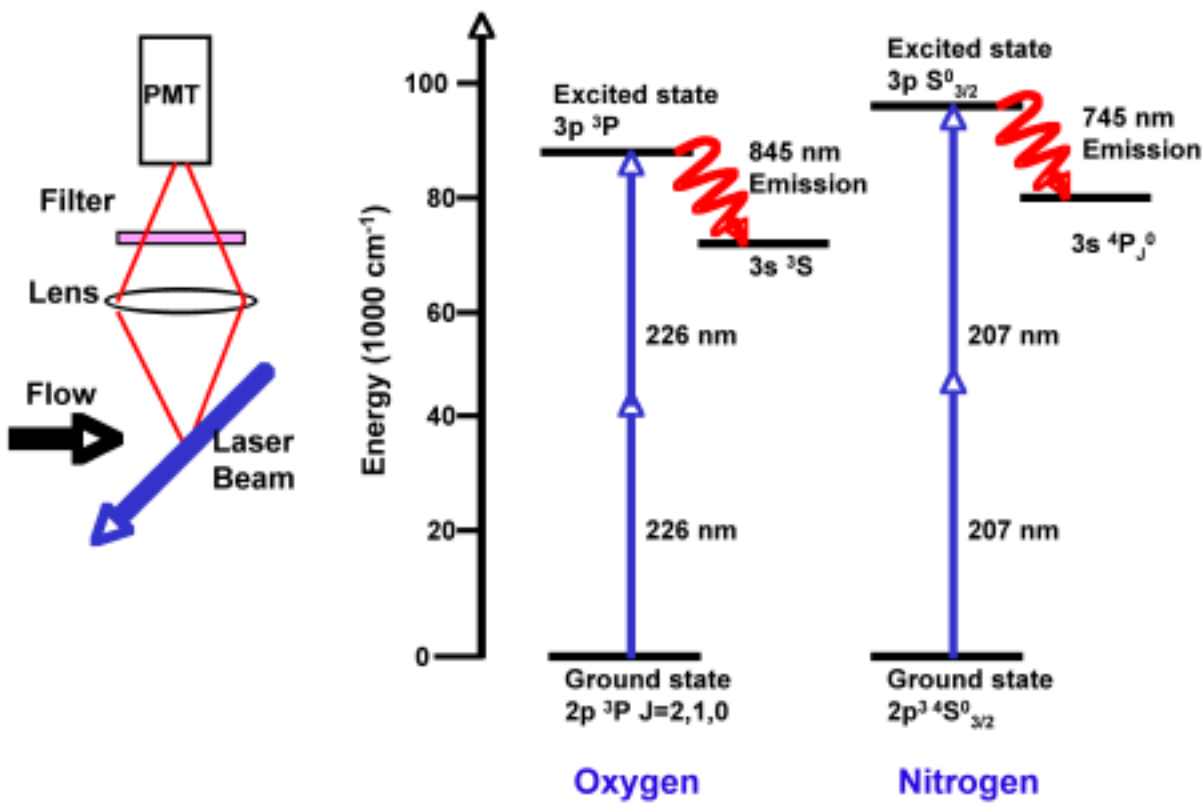


Fig. 7. Energy level diagrams for two common two-photon LIF schemes for probing atomic oxygen and atomic nitrogen. The spatial resolution of the LIF approach is indicated by the cartoon at the left.

The experimental arrangement for probing either atomic oxygen or nitrogen is essentially the same, as shown in Fig. 8. A Nd:YAG-pumped dye laser provides the fundamental output, which is converted by the appropriate tripling crystal arrangement to the desired ultraviolet, two-photon wavelength. As indicated in the figure, the ultraviolet output is split into three different paths. The first is directed toward the plasma stream (either ICP or arc-jet), while the other two paths are directed toward a NO reference cell and a microwave-discharge flow reactor, respectively. The NO cell is used to assess the laser performance and to guide laser tuning toward the relatively sparse two-photon excitation wavelengths. Within the flow reactor, the microwave discharge creates a stable, non-equilibrium population of atoms at known pressure and temperature, and the fluorescence from this population can be used to calibrate the fluorescence signals from the plasma stream. This calibration enables measurement of translation temperature, flow velocity (depending on the facility and beam orientation), and number density of the target species.

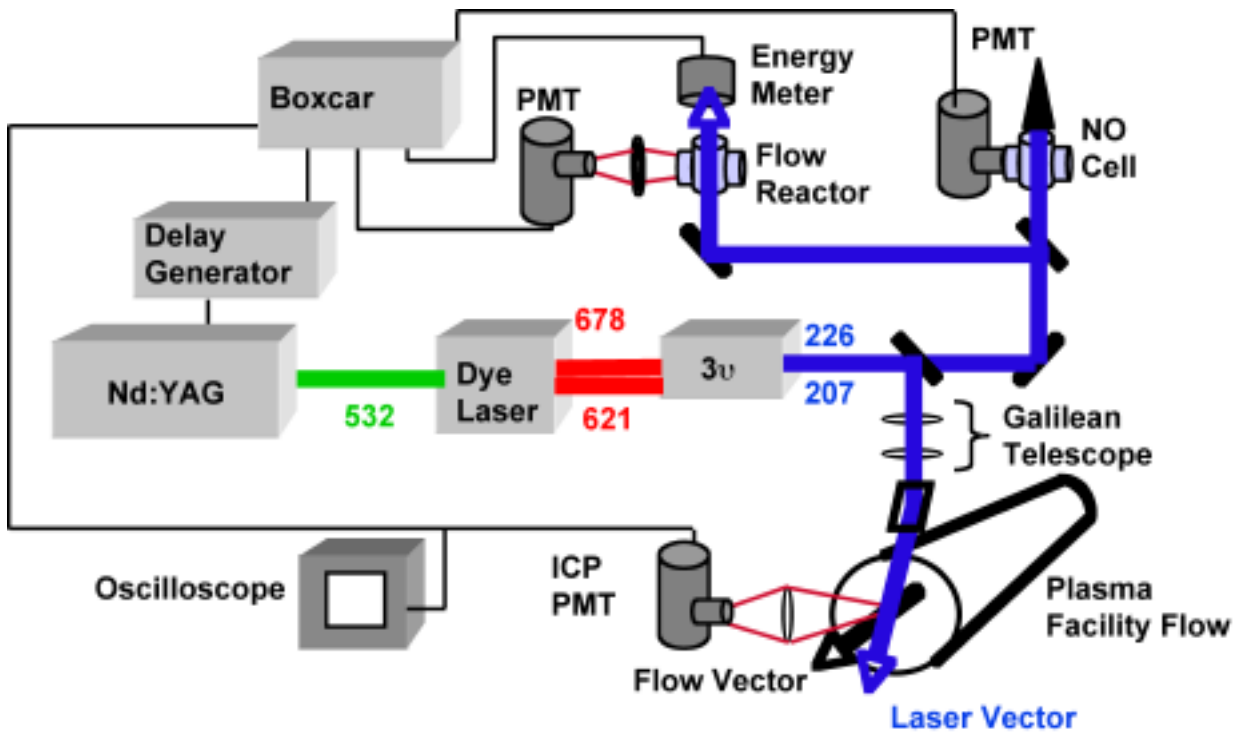


Fig. 8. Schematic of the experimental configuration for two-photon LIF implementation in arc-jet and ICP facilities. In addition to measuring LIF from the plasma facility, measurements are made in a nitric oxide cell for laser wavelength monitoring and in a flow reactor for calibration of the facility measurements. The temperature and atomic number density in the flow reactor are known independently of the laser measurements.

An example of atomic nitrogen fluorescence acquired in an ICP facility is shown in Fig. 9, where the atomic nitrogen fluorescence is plotted as a function of the dye laser fundamental wavelength. The broader of the two traces is the signal collected from plasma stream at the boundary layer edge and the narrower, less noisy signal is from a microwave-discharge flow reactor. The smooth curves for each LIF signal are nonlinear least-squares fits to the line profiles using a spectral model that includes the relevant broadening mechanisms and uses the total line width as a fitting parameter. Line shape fit results from the flow reactor signal are used to extract information from the plasma stream measurements as explained in the following paragraphs. Finally, the temperature value derived for this particular measurement is indicated on the figure, along with the flow reactor temperature used to extract the laser line width.

The translation gas temperature is derived from a measurement of the total width of the transition once the laser line width is determined from the flow reactor line shape as,

$$T = \frac{M_N c^2}{8 \ln(2) k_B n_A \hat{\nu}^2} \left[\Delta \hat{\nu}_{T,F}^2 - (\Delta \hat{\nu}_{T,R}^2 - \Delta \hat{\nu}_{D,R}^2) \right] , \quad (10)$$

where M is the molar mass, c is the speed of light, k_B is the Boltzmann constant, n_A is Avogadro's number, and $\hat{\nu}$ is the transition frequency in cm^{-1} . The different widths $\Delta \hat{\nu}^2$ (also cm^{-1}) are labeled with subscripts that designate Total or Doppler and Flow or Reactor. The flow velocity can be determined from the Doppler shift of the central transition wavelength, λ , as

$$v = \frac{c \Delta \lambda}{\lambda \cos \theta} , \quad (11)$$

and only a separate measurement of the angle between the velocity and laser propagation vectors, \square , is needed. While the Doppler shift in the free stream of supersonic arc-jet facilities is quite large, and can be used to reliably measure the free stream velocity, the Doppler shift in subsonic ICP facilities is too small for velocity determination, as is clearly evident in Fig. 9.

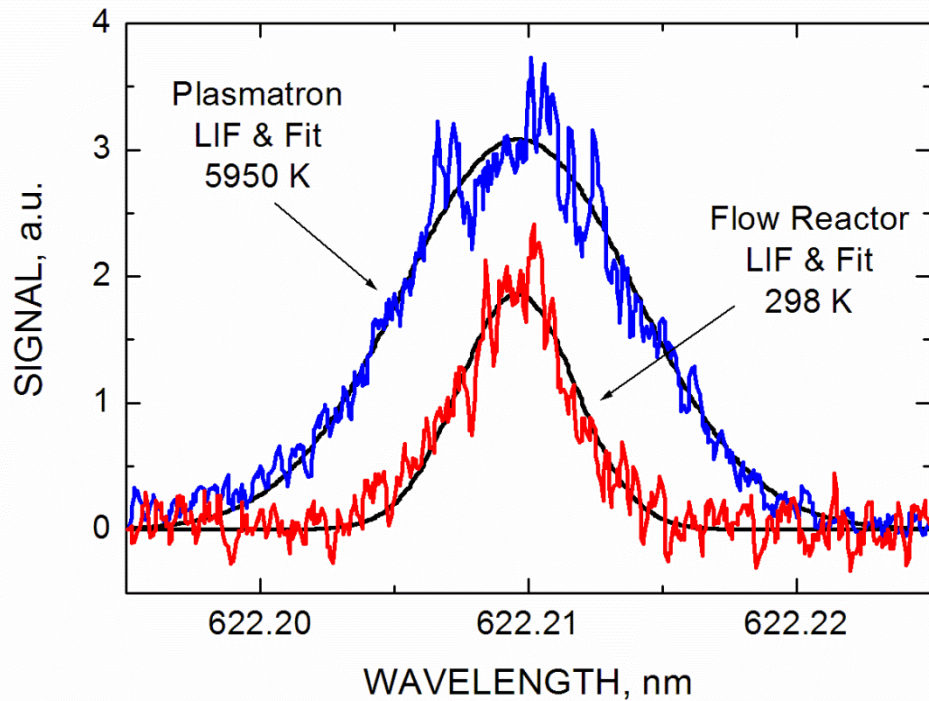


Fig. 9. Two-photon LIF signals from excitation of the 207 nm transition of atomic nitrogen at the boundary layer edge in the VKI Plasmatron ICP Torch Facility. Despite the fact that the beam is angled with respect to the axial stream velocity (as shown in Fig. 8) the subsonic flow speed does not provide a measurable shift between the flow-reactor and ICP stream transition line centers. The spectral fit assumes that Doppler broadening is the dominant line broadening mechanism.

Finally, the local number density of atomic nitrogen is determined from integrated LIF signal. Several additional measurements are required to obtain absolute values of number density, including characterization of the fluorescence collection efficiency, the temporal and spatial characteristics of the laser beam, and finally the use of either a known N-atom reference population, a rare gas calibration,⁶⁷⁻⁶⁹ or a two-photon excitation cross-section measurement.⁶⁴⁻⁶⁶ For the latter approach, the expression for nitrogen atom number density is

$$n_N = \frac{4\pi}{D} \frac{\tau_{rad}}{\tau_{obs}} \frac{A_p}{\int F^2(t) dt} \frac{(hv)^2}{G^{(2)} \sigma^{(2)}} \int \frac{S_N(\omega)}{E_p^2} d\omega , \quad (12)$$

where S_N is the LIF signal in volts, τ are the radiative and observed lifetimes, A_p is the beam area, D is the collection optics calibration factor, $F^2(t)$ is the square of the temporal laser pulse shape and the $G^{(2)} \sigma^{(2)}$ product represents the two-photon LIF cross section.

Two-photon LIF has been implemented in arc-jets to characterize the free stream conditions^{58,59} and to investigate free stream property gradients.^{61,70} By measuring the three quantities noted above in nitrogen/argon plasma flows, and making use of a pitot pressure measurement and facility data, it is possible to calculate the stream total enthalpy and to quantify the different contributions: thermal, kinetic, and chemical. This is extremely useful for establishing stream conditions, extrapolating the free stream test conditions to a flight environment, and provides experimental data against which a CFD computation of gas flow through the arc-jet nozzle and towards the test article can be tested. However, arc-jet free stream measurements still only provide a different starting point for the eventual assessment of the boundary layer conditions above a test article.

The arc-jet free stream measurements indicate low translational temperatures, high velocity and non-equilibrium atom number densities.^{58,59} In contrast, the boundary layer edge measurement from the ICP facility discussed above (Fig. 9) indicates high translational temperature and low velocity. It is reasonable to expect that within the boundary layer in an arc-jet test, LIF measurements would be quite different from those of the free stream, and more likely, similar to those of the ICP facility boundary layer edge.

For material test applications temperature and species information from the reacting boundary layer is extremely important. While LIF measurements in the boundary layer are relatively rare, recent experiments indicate their feasibility.^{60,70} Two strategies exist for measuring species and temperature profiles above the surface. The first is a point-wise approach that involves translating the laser probe volume toward the surface, as indicated in Fig. 10, and the other is a planar approach that requires sufficient laser pulse energy to spread the beam into a light sheet. In the latter, an intensified camera is needed to record the fluorescence signals, which complicates the interpretation of the measured signals.

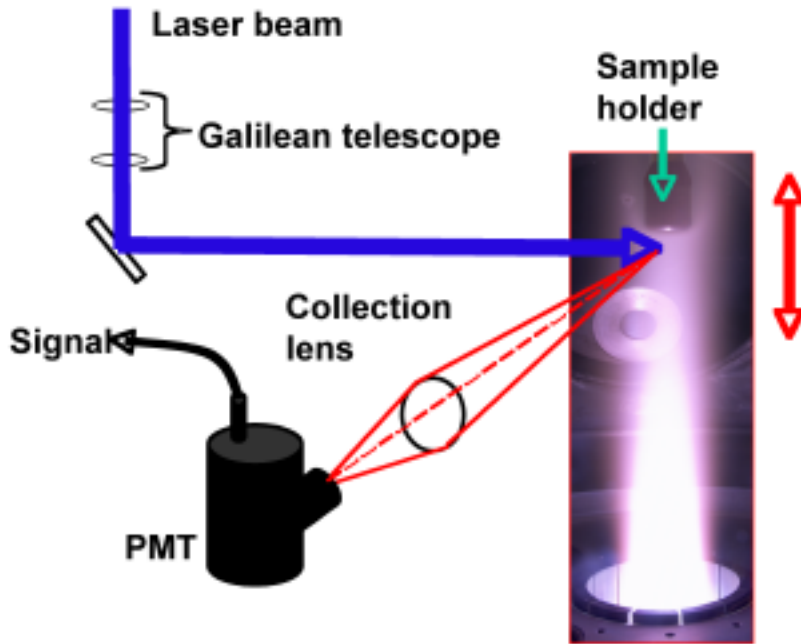


Fig. 10. Translation of either the test article or the beam delivery and collection optics to measure the species number densities and temperature in the boundary layer approaching the test article in the stagnation region.

Figure 11 shows computed boundary layer profiles of temperature, and total and species number densities, for an air plasma along the stagnation streamline for a particular high-enthalpy test condition.¹⁷ The catalytic efficiency of the surface was set to a relatively low 10^{-4} for these computations. Temperature and number densities are normalized by their boundary layer edge values. Different information is available from different species measurements. All species number densities increase with approach to the surface because of the decreasing gas temperature in a constant pressure boundary layer. The relative O-atom number density and total mixture number density curves overlay each other in Fig. 11, indicating that for these plasma conditions, relatively little gas-phase recombination of O to O₂ occurs. The N-atom number density increases more slowly and the N₂ number density more rapidly than the total number density, indicating that gas-phase recombination of N to N₂ is important at these conditions.

Whether probing N or O, if a simultaneous measurement of the atom number density and translational temperature can be obtained (as described above) as a function of distance from the sample surface, the total number density can then be computed from a pressure measurement and the translational temperature using the ideal gas equation of state $n = P/k_B T$. This, along with the measured atom number density, gives the mole fraction of the probed atomic species. For a pure nitrogen plasma this can completely characterize the local thermodynamic conditions, as long as ionization is not significant, since the N₂ number density can be found from $n_{N_2} = n - n_N$. For an air plasma, measurements of both O-atom and N-atom number densities are needed for a complete understanding of the local thermodynamic state.

The relative species density profiles presented in Fig. 11 show trends characteristic of a low catalyicity, non-reacting surface, wherein the relative number densities increase towards the wall as determined by the gas temperature profile and gas-phase recombination reactions. For a highly catalytic surface the atomic species number densities should trend downward approaching the surface to very small levels. Reported species density uncertainties^{60,70} suggest that measurement of gradients with density changes of two to four are realizable, especially when relative LIF signals are used to measure the trend of a normalized species density.

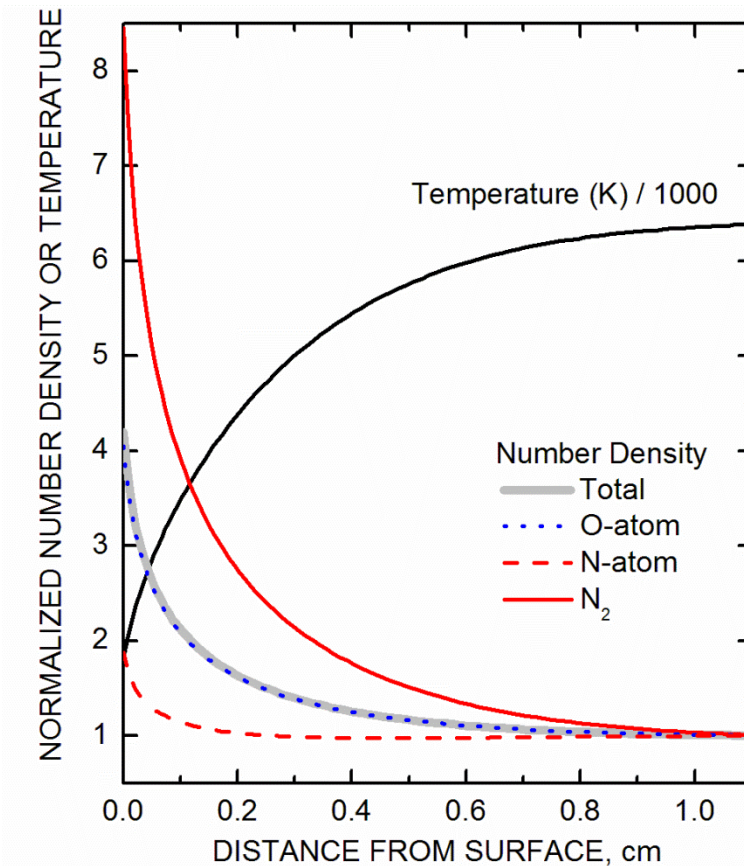


Fig. 11. Computed temperature, mixture density, and species number density variations along the stagnation streamline for the flow over a low-catalyicity sample in the VKI Plasmatron ICP Torch Facility. The number densities are normalized by their free stream (boundary layer edge) values. Note that the total and O-atom number density curves overlay one another, indicating that for these boundary layer conditions there is little gas-phase recombination of O to O₂.

The monitoring of volatile products during high-enthalpy UHTC testing by LIF is also possible, although such work has not yet been reported. Both B atoms⁷¹ and BO molecules^{72,73} have been detected by LIF schemes, as have Si atoms^{74,75} and SiO molecules^{74,76}. Feigl and Auweter-Kurtz⁷⁷ have used LIF to monitor SiO concentrations in front of SiC materials oxidized in argon-oxygen-nitrogen plasma flows, by exciting the SiO ($A\ ^1D \leftarrow X\ ^1\Sigma^+(0,0)$) transition near

234 nm and collecting fluorescence near 260 nm from the $(A\ ^1D \rightarrow X\ ^1\Sigma^+(0,3))$ band. They associate rapid rises of SiO in the gas phase with the transition between passive and active SiC oxidation (i.e., between reactions (4) and (5)). Beyond the simple detection of volatile species, spatially-resolved LIF of volatiles in the boundary layer would enable the measurement of species gradients that could in principle be related to volatilization rates from the surface. No measurements of this type have yet been attempted and their interpretation would require additional gas-phase chemistry inputs to existing CFD programs.

4.4. Other Techniques

4.4.1 Fourier Transform Infrared Spectroscopy

Fourier Transform Infrared (FTIR) spectroscopy is a technique used to capture and spectrally resolve infrared radiation using a scanning interferometer, typically at wavelengths between 1 and 40 μm . Transmission FTIR spectroscopy is often used as a laboratory technique to identify chemical species in gas or liquid samples, by absorption features that occur at characteristic energies (wavelengths) related to particular vibrational modes of different chemical bonds. These characteristic absorption features are relatively sharp in the gas phase, and often broaden and shift slightly in the liquid phase. A similar technique is used to detect molecules on surfaces by reflection FTIR and can be used to monitor thin film growth.

Estimates of the temperature-dependant total, hemispherical emittance are often derived from spectrally-resolved, hemispherical reflectance measurements performed at room temperature using FTIR instruments fit with integrating spheres.¹⁷ The measured spectral reflectance, $\rho_{298}(\lambda)$, is converted to spectral absorbance, $\alpha_{298}(\lambda)$, using the relation $\alpha_{298}(\lambda) = 1 - \rho_{298}(\lambda)$ valid for an opaque surface, and the spectral absorbance is equated to the spectral emittance based on Kirchhoff's law, $\varepsilon_{298}(\lambda) = \alpha_{298}(\lambda)$. Total hemispherical emittance at any temperature is then computed by averaging the room-temperature emittance over the Planck blackbody radiation function:

$$\varepsilon(T) \approx \frac{\int_{\lambda_1}^{\lambda_2} \varepsilon_{298}(\lambda) E_b(\lambda, T) d\lambda}{\int_{\lambda_1}^{\lambda_2} E_b(\lambda, T) d\lambda} \quad . \quad (13)$$

This process assumes that the temperature dependence of total emittance is dominated by the temperature dependence of the Planck function and not by the optical constants of the material. It also presumes that the spectral range of the measurement, λ_1 to λ_2 , is sufficiently broad that it contains the spectral region dominating the emissive power at each temperature.

A variant of this technique - emission FTIR - was recently used in a laboratory setting to capture thermal emission from C/ZrB₂-SiC composites over the 200 to 800°C temperature range and an effective temperature-dependant emittance was computed.⁷⁸ However, the spectral range of the FTIR instrument used in this work was only 8–14 μm and this limited range contains just ~40% of the radiative power emitted at 200°C and less than 10% of the emitted power at 800°C. The derived emittance values are thus tenuous approximations for the total emittance.

Marschall et al.¹⁷ have shown how a broad feature in the FTIR reflectance spectra of virgin ZrB₂-30SiC in the 10-13 μm range was removed and replaced by a sharper feature centered near 9 μm after oxidation. The former feature can be related to stretching mode vibrations of Si-C bonds and the latter to stretching mode vibrations of Si-O bonds. A similar enhanced reflectance feature predicted for ZrO₂ near 14 μm was not observed in oxidized samples, consistent with the fact that the outer scale was dominated by silica-rich glass.

Related spectral features should appear as emittance modifications to the Planck blackbody radiation function in thermal emission. This suggests that FTIR emission spectroscopy might be used as an *in situ* monitor for changing surface compositions during high-enthalpy testing. Measurements of this type were made by Hirsch et al.⁵² for characterizing the oxidation behavior of carbon/carbon and carbon/silicon carbide composites in the ICP wind tunnels. However, this concept has never been explored as an *in situ* diagnostic for UHTC materials systems.

Even without reference to a blackbody standard, the broad mid-IR spectral features associated with SiO₂, SiC, ZrO₂ and HfO₂ are sufficiently separated that difference spectra should track shifts in the dominant surface composition with time. This approach has the potential to monitor important thermodynamic and chemical transitions as test conditions are varied or as constituents are depleted over time. For example, changes in the relative strengths of the SiO₂ and SiC spectral features could be used to track the important transition from passive SiC oxidation with the formation of condensed silica to active SiC oxidation with the formation of volatile SiO. The identification of temperature and pressure thresholds at which the loss of SiO₂ from the oxide scale becomes large—be it by active oxidation, evaporation, or melt flow—is critical to UHTC performance and should be evidenced by the appearance of the ZrO₂ or HfO₂ features above 14 μm .

4.4.2 Absorption Spectroscopy

The spatial resolution advantage of the LIF technique has been contrasted above with path-integrated emission measurements, which can also clearly provide useful information for material test applications. Similarly, absorption measurements can provide useful information since they typically probe either ground or low-lying electronic states even though this information is also path-integrated. One such application is the measurement of molecular species formed by gas/surface interactions.

Advances in semiconductor processing have enabled rapid development of Tunable Diode Laser Absorption Spectroscopy (TDLAS). Relatively inexpensive, but tunable, diode

lasers operating with narrow line widths can be optimized for overlap with favorable rotational-vibrational transition features of important molecular species that have dipole moments, such as NO, CO₂, CO, H₂O, SiO, and BO. Access to ground electronic state population information is often available by probing rotational-vibrational transitions in the 1 to 5 μm wavelength region. Neither O₂ nor N₂ have dipole moments, and so are not considered candidate species for this approach; however, in the case of O₂, it is possible to probe the ground state by absorption via the A electronic band transition ($b^1 \Sigma_g^+ \leftarrow X^3 \Sigma_g^-$) near 760 nm. This approach has been used to characterize shock tube flows,⁷⁹ but has not yet been applied to either arc-jet or ICP facility measurements.

Recently, the TDLAS technique was used to probe CO in a Mars atmosphere study in an arc-jet facility, where path-integrated values of translation temperature, velocity, and CO concentration were obtained.⁸⁰ To date however, the application of TDLAS in the boundary layer near a catalytic or reacting material surface in a plasma facility to quantify recombined or reaction-produced molecules has not been reported.

4.4.3 Raman Spectroscopy

Raman scattering, like LIF, is an inelastic scattering process, but involves excitation to a virtual upper energy level. In Raman spectroscopy, a laser beam illuminates the gas mixture and Raman scattered photons are detected at wavelengths offset from the illumination wavelength by increments determined by the vibrational and rotational energy spacing of molecules in gas. By choosing an appropriate laser wavelength (typically in the ultraviolet since Raman cross sections scale as frequency to the fourth power), and using a high-resolution spectral filter (often a spectrometer), scattered signals from molecules in a gas mixture can be recorded and analyzed for species concentration and temperature. Details of this common spectroscopic technique can be found in Eckbreth.⁵⁶

An attractive attribute of Raman scattering is that, as in the case of LIF, it provides spatially resolved information, and so can be used to map temperature and species gradients. In addition, each molecular species present scatters at its characteristic Raman wavelengths, so a single laser frequency can access multiple species, depending on the strength of their Raman cross sections. Since all molecules are Raman-active, this technique can detect important species involved in UHTC oxidation and volatilization processes, like SiO, SiO₂, BO, BO₂, CO, and CO₂.

While applications to plasma flows in arc-jet and ICP facilities are relatively sparse, one recent investigation has demonstrated the potential of this technique in the area of recombined molecular species quantification.⁸¹ In this investigation a frequency tripled Nd:YAG laser operating at 355 nm was used to probe the boundary layer of an air plasma flowing over a flat stainless steel plate in an ICP facility. Despite the relatively weak Raman cross sections ($\sim 10^{-31} \text{ cm}^2 \text{ sr}^{-1}$) profiles of N₂ and O₂ number density, rotational temperature, and vibrational temperature were obtained in the boundary layer flow. Long steady test times were needed to achieve usable signal-to-noise levels, but the results are promising for future applications.

Summary

Arc-jet and ICP plasma tunnels remain the primary facilities used to ground test the performance of UHTC TPS materials and components for hypersonic flight. We have highlighted the main features of the test conditions obtained in these two types of facilities and discussed their similarities and differences. Various *in situ* optical diagnostics, both established and under development, were described, that can provide information to document test conditions, monitor the evolution of test articles, and provide data that can be used to strengthen the accuracy of CFD models. The importance of CFD modeling of the arc-jet and ICP test environments, and in particular the computation of species concentrations at specimen surfaces, is emphasized as essential for materials science interpretations of UHTC test results. The increasing integration of CFD modeling and *in situ* optical diagnostics in plasma tunnel testing is sure to enhance the understanding and optimization of UHTC material performance in aerothermal environments.

Acknowledgements

This work was supported by the High-Temperature Aerospace Materials Program of the Air Force Office of Scientific Research through contracts FA9550-08-C-0049 (J. Marschall) and FA9550-08-1-0414 (D. Fletcher). We acknowledge Jan Thömel for the CFD results presented in Sections 3 and 4.3, and Mickaël Playez for the emission measurements highlighted in Section 4.2.

References

¹Fuller, J., Blum, Y., and Marschall, J., Topical Issue on Ultra-High-Temperature Ceramics. *J. Am. Ceram. Soc.*, 2008, **91**, 1397-1502.

²Fuller, J. and Sacks, M., Special Section: Ultra-High Temperature Ceramics. *J. Mater. Sci.*, 2004, **39**, 5885-6066.

³Kaufman, L., Boride Composites - A New Generation of Nose Cap and Leading Edge Materials for Reusable Lifting Re-entry Systems. AIAA Advanced Space Transportation Meeting, AIAA Paper 70-278, February 1970.

⁴Bull, J., Kolodziej, P., Salute, J., and Keese, D., Design, Instrumentation and Preflight Testing of a Sharp Ultra-High Temperature Ceramic Nose tip. NASA TM-1998-112229, October 1998.

⁵Kolodziej, P., Bull, J., Salute, J., and Keese, D. L., First Flight Demonstration of a Sharp Ultra-High Temperature Ceramic Nose tip. NASA TM-112215, December 1997.

⁶Kinney, D. J., Bowles, J. V., Yang, L. H., and Roberts, C. D., Conceptual Design of a "SHARP"-CTV. 35th AIAA Thermophysics Conference, AIAA Paper 2001-2887, June 2001.

⁷Reuther, J., Kinney, D., Smith, S., Kontinos, D., Gage, P., and Saunders, D., A Reusable Space Vehicle Design Study Exploring Sharp Leading Edges. 35th AIAA Thermophysics Conference, AIAA Paper 2001-2884, June 2001.

⁸Metcalfe, A. G., Elsner, N. B., Allen, D. T., Wuchina, E., Opeka, M., and Opila, E., Oxidation of Hafnium Diboride. *Electrochemical Society Proceedings*, 1999, **99-38**, 489-501.

⁹Wuchina, E. J. and Opeka, M. M., Oxidation of Hf-Based Ceramics. *Electrochemical Society Proceedings*, 1999, **99-38**, 477-488.

¹⁰Opila, E., Levine, S., and Lorincz, J., Oxidation of ZrB₂- and HfB₂-Based Ultra-High Temperature Ceramics: Effect of Ta Additions. *J. Mater. Sci.*, 2004, **39**, 5969-5977.

¹¹Gasch, M., Ellerby, D., Irby, E., Beckman, S., Gusman, M., and Johnson, S., Processing, Properties, and Arc Jet Oxidation of Hafnium Diboride/Silicon Carbide Ultra High Temperature Ceramics. *J. Mater. Sci.*, 2004, **39**, 5925-5937.

¹²Chamberlain, A., Fahrenholtz, W., Hilmas, G., and Ellerby, D., Oxidation of ZrB₂-SiC Ceramics Under Atmospheric and Reentry Conditions. *Refractories Applications Transactions*, 2005, **1**, 2-8.

¹³Savino, R., De Stefano Fumo, M., Silvestroni, L., and Sciti, D., Arc-Jet Testing on HfB₂ and HfC-based Ultra-High Temperature Ceramic Materials. *Journal of the European Ceramic Society*, 2008, **28**, 1899-1907.

¹⁴Monteverde, F. and Savino, R., Stability of Ultra-High Temperature ZrB₂-SiC Ceramics Under Simulated Atmospheric Re-Entry Conditions. *Journal of the European Ceramic Society*, 2007, **27**, 4797-4805.

¹⁵Zhang, X., Hu, P., Han, J., and Meng, S., Ablation Behavior of ZrB₂-SiC Ultra High Temperature Ceramics under Simulated Atmospheric Re-Entry Conditions. *Composites Science and Technology*, 2008, **68**, 1718-1726.

¹⁶Ito, T., Kurotaki, T., Sumi, T., Fujita, K., Ishida, K., and Mizuno, M., Evaluation of Surface Catalytic Effect on TPS in 110kW ICP-Heated Wind Tunnel. 43rd AIAA Aerospace Sciences Meeting and Exhibit, AIAA Paper 2005-189, January 2005.

¹⁷Marschall, J., Pejaković, D. A., Fahrenholtz, W. G., Hilmas, G. E., Zhu, S., Ridge, J., Fletcher, D. G., Asma, C. O., and Thömel, J., Oxidation of ZrB₂-SiC Ultra-High Temperature Ceramic Composites in Dissociated Air. *J. Thermo. Heat Trans.*, 2009, **23**, 267-278.

¹⁸Playez, M., Fletcher, D. G., Marschall, J., Fahrenholtz, W. G., Hilmas, G. E., and Zhu, S., Optical Emission Spectroscopy during Plasmatron Testing of ZrB₂-SiC Ultra-High Temperature Ceramic Composites. *J. Thermo. Heat Trans.*, 2009, **23**, 279-285.

¹⁹Smith, R. K., Wagner, D. A., and Cunningham, J., A Survey of Current and Future Plasma Arc-Heated Test Facilities for Aerospace and Commercial Applications. 36th Aerospace Sciences Meeting and Exhibit, AIAA Paper 1998-0146, January 1998.

²⁰Ragsdale, R., Lanzo, C., Randall, D., and Thorpe, M., Reentry Heating Experiments Using an Induction Heated Plasma. NASA TM X-1978, Cleveland, OH, March 1970.

²¹Bose, D., Skokova, K., Wright, M. J., and Reuther, J., Ground-to-Flight Traceability Analysis of Arcjet Testing for the Crew Exploration Vehicle. 41st AIAA Thermophysics Conference, AIAA Paper 2009-3845, June 2009.

²²Kolesnikov, A. F., The Concept of Local Simulation for Stagnation Point Heat Transfer in Hypersonic Flows: Applications and Validation. 21st AIAA Aerodynamic Measurement Technology and Ground Testing Conference, AIAA Paper 2000-2515, June 2000.

²³Gökçen, T., Effects of Flowfield Nonequilibrium on Convective Heat Transfer to a Blunt Body. 34th Aerospace Sciences Meeting and Exhibit, AIAA Paper 96-0352, January 1996.

²⁴Barbante, P. F. and Chazot, O., Flight Extrapolation of Plasma Wind Tunnel Stagnation Region Flowfield. *J. Thermo. Heat Trans.*, 2006, **20**, 493-499.

²⁵Parthasarathy, T. A., Rapp, R. A., Opeka, M., and Kearns, R. J., A Model for the Oxidation of ZrB₂, HfB₂, and TiB₂. *Acta Mater.*, 2007, **55**, 5999-6010.

²⁶Rezaie, A., Fahrenholtz, W. G., and Hilmas, G. E., Evolution of Structure During the Oxidation of Zirconium Diboride-Silicon Carbide in Air up to 1500 °C. *Journal of the European Ceramic Society*, 2007, **27**, 2495-2501.

²⁷Fahrenholtz, W. G., Thermodynamic Analysis of ZrB₂-SiC Oxidation: Formation of a SiC-Depleted Region. *J. Am. Ceram. Soc.*, 2007, **90**, 143-148.

²⁸Li, J., Lenosky, T. J., Först, C. J., and Yip, S., Thermochemical and Mechanical Stabilities of the Oxide Scale of ZrB₂+SiC and Oxygen Transport Mechanisms. *J. Am. Ceram. Soc.*, 2008, **91**, 1475-1480.

²⁹Fletcher, D. G. and Playez, M., Characterization of Supersonic and Subsonic Plasma Flows. 25th AIAA Aerodynamic Measurement Technology and Ground Test Conference, AIAA Paper 2006-3294, June 2006.

³⁰Barbante, P. F., Degrez, G., and Sarma, G. S. R., Computation of Nonequilibrium High-Temperature Axisymmetric Boundary-Layer Flows. *J. Thermo. Heat Trans.*, 2002, **16**, 490-497.

³¹Magin, T., Vanden Abeele, D. P., and Degrez, G., An Implicit Multiblock Solver for Inductive Plasma Flows. *Fluids 2000*, AIAA Paper 2000-2480, June 2000.

³²Vanden Abeele, D. P. and Degrez, G., Numerical Model of High-Pressure Air Inductive Plasma Under Thermal and Chemical Non-Equilibrium. 31st AIAA Plasmadynamics and Laser Conference, AIAA Paper 2000-2416, June 2000.

³³Bottin, B., Vanden Abeele, D. P., Carbonaro, M., Degrez, G., and Sarma, G. S. R., Thermodynamic and Transport Properties for Inductive Plasma Modeling. *J. Thermo. Heat Trans.*, 1999, **13**, 343-350.

³⁴Wright, M. J., Candler, G. V., and Bose, D., Data-Parallel Line Relaxation Method for the Navier-Stokes Equations. *AIAA Journal*, 1998, **36**, 1603-1609.

³⁵Gökçen, T., Chen, Y.-K., Skokova, K. A., and Milos, F. S., Computational Analysis of Arc-Jet Stagnation Tests

Including Ablation and Shape Change. 41st AIAA Thermophysics Conference, AIAA Paper 2009-3596, June 2009.

³⁶Gökçen, T., Skokova, K., Balboni, J. A., Terrazas-Salinas, I., and Bose, D., Computational Analysis of Arc-Jet Wedge Calibration

Tests in IHF 6-Inch Conical Nozzle. 47th AIAA Aerospace Sciences Meeting, AIAA Paper 2009-1348, January 2009.

³⁷Gökçen, T. and Stewart, D. A., Computational Analysis of Semi-Elliptical Nozzle Arc-Jet Experiments: Calibration Plate and Wing Leading Edge. 35th AIAA Fluid Dynamics Conference and Exhibit, AIAA Paper 2005-4887, June 2005.

³⁸Gordon, S. and McBride, B. J., Computer Program for Calculation of Complex Chemical Equilibrium Compositions and Applications I. Analysis. NASA RP-1311, Cleveland, Ohio, October 1994.

³⁹Ramshaw, J. D., Self-Consistent Effective Binary Diffusion in Multicomponent Gas Mixtures. *Journal of Non-Equilibrium Thermodynamics*, 1990, **15**, 295-300.

⁴⁰Gupta, R., Yos, J., Thompson, R., and Lee, K., A Review of Reaction Rates and Thermodynamic and Transport Properties for an 11-Species Air Model for Chemical and Thermal Nonequilibrium Calculations to 30000 K. NASA RP-1232, August 1990.

⁴¹Wright, M. J., Bose, D., Palmer, G. E., and Levine, E., Recommended Collision Integrals for Transport Property Computations, Part 1: Air Species. *AIAA Journal*, 2005, **43**, 2558-2564.

⁴²Wright, M. J., Hwang, H. H., and Schwenke, D. W., Recommended Collision Integrals for Transport Property Computations Part 2: Mars and Venus Entries. *AIAA Journal*, 2007, **45**, 281-288.

⁴³Scatteia, L., Borrelli, R., Cosentino, G., Bêche, E., Sans, J.-L., and Balat-Pichelin, M., Catalytic and Radiative Behaviors of ZrB₂-SiC Ultrahigh Temperature Ceramic Composites. *J. Spacecraft Rock.*, 2006, **43**, 1004-1012.

⁴⁴Scatteia, L., Alfano, D., Monteverde, F., Sans, J.-L., and Balat-Pichelin, M., Effect of Machining Method on the Catalytic and Emissivity of ZrB₂ and ZrB₂-HfB₂-Based Ceramics. *J. Am. Ceram. Soc.*, 2008.

⁴⁵Park, C. and Moore, D., A Polynomial Method for Determining Local Emission Intensity by Abel Inversion. NASA TN D-5677, February 1970.

⁴⁶Spalding, M. J., Krier, H., and Burton, R. L., Boron Suboxides Measured During Ignition and Combustion of Boron in Shocked Ar/F/O₂ and Ar/N₂/O₂ Mixtures. *Comb. Flame*, 2000, **120**, 200-210.

⁴⁷Ralchenko, Y., Kramida, A. E., and Reader, J., NIST Atomic Spectra Database (Version 3.1.5). National Institute of Standards and Technology, <http://physics.nist.gov/asd3>, 2008.

⁴⁸Monteverde, F. and Bellosi, A., Oxidation of ZrB₂-Based Ceramics in Dry Air. *Journal of the Electrochemical Society*, 2003, **150**, B552-B559.

⁴⁹Monteverde, F. and Bellosi, A., The Resistance to Oxidation of an HfB₂-SiC Composite. *Journal of the European Ceramic Society*, 2005, **25**, 1025-1031.

⁵⁰Rizzo, H. F., "Oxidation of Boron at Temperatures between 400 and 1300 °C in Air." in *Boron - Synthesis, Structure, and Properties*, edited by J. A. Kohn and W. F. Nye, (Plenum Press, New York, 1968), p. 175-189.

⁵¹Roine, A., HSC Chemistry for Windows, Version 5.11. Outokumpu Research Oy, Pori, Finland, (2006).

⁵²Hirsch, K., Roth, B., Altmann, I., Barth, K.-L., Jentschke, H., Lunk, A., and Schumacher, U., Plasma-Induced Silica-Like Protection Layer Formation on C/C-SiC Heat-Shield Materials for Re-Entry Vehicles. *High Temperatures - High Pressures*, 1999, **31**, 455-465.

⁵³Altmann, I., Bauer, G., Hirsch, K., Jentschke, H., Klenga, S., Roth, B., Schinköth, D., and Schumacher, U., In-Situ Diagnostics of the Interaction Region Between a Nitrogen-Oxygen Plasma Jet and Hot C/C-SiC Ceramic Materials. *High Temperatures - High Pressures*, 2000, **32**, 573-579.

⁵⁴Jentschke, H., Hirsch, K., Klenga, S., and Schumacher, U., High Resolution Emission and Absorption Spectroscopy for Erosion Product Analysis in Boundary Plasmas. *Review of Scientific Instruments*, 1999, **70**, 336-339.

⁵⁵Herdrich, G., Fertig, M., Löhle, S., Pidan, S., and Augweter-Kurtz, M., Oxidation Behavior of Siliconcarbide-Based Materials by Using New Probe Techniques. *J. Spacecraft Rock.*, 2005, **42**, 817-824.

⁵⁶Eckbreth, A. C., *Laser Diagnostics for Combustion Temperature and Species*. Abacus Press, Cambridge, 1988.

⁵⁷Crosley, D. R., Jeffries, J. B., and Smith, G. P., Absolute Concentration Measurements of Chemically-Important Flame Radicals. *Israel Journal of Chemistry*, 1999, **39**, 41-48.

⁵⁸Fletcher, D., Arc-Jet Flow Properties Determined from Laser-Induced Fluorescence of Atomic Nitrogen. *Appl. Opt.*, 1999, **38**, 1850-1858.

⁵⁹Fletcher, D. G. and Bamford, D. J., Arcjet Flow Characterization Using Laser-Induced Fluorescence of Atomic Species. 7th AIAA/ASME Joint Thermophysics and Heat Transfer Conference, AIAA Paper 98-2458, June 1998.

⁶⁰Löhle, S., Auweter-Kurtz, M., Herdrich, G., and Laux, T., Measurements of NO in N₂/O₂ and N₂/CO₂ Plasma Flows. 36th AIAA Thermophysics Conference, AIAA Paper 2003-3487, June 2003.

⁶¹Grinstead, J., Driver, D., and Raiche, G., Radial Profiles of Arc-Jet Flow Properties Measured with Laser-Induced Fluorescence of Atomic Nitrogen. 41st Aerospace Sciences Meeting and Exhibit, AIAA Paper 2003-0400, January, 2003.

⁶²Laux, T., Feigl, M., Stöckle, T., and Auweter-Kurtz, M., Estimation of the Surface Catalytic Properties of PVD-Coatings by Simultaneous Heat Flux and LIF Measurements in High Enthalpy Air Flows. 34th AIAA Thermophysics Conference, AIAA Paper 2000-2364, June 2000.

⁶³Bamford, D. G., Dyer, M. J., and Bischel, W. K., Single-Frequency Laser Measurements of Two-Photon Cross Sections and Doppler-Free Spectra for Atomic Oxygen. *Phys. Rev. A*, 1987, **36**, 3497-3500.

⁶⁴Bamford, D. J., Bischel, W. K., Hickman, A. P., and Dyer, M. J., in *Proceedings of the Society of Photo-Optical Instrumentation Engineers*; Vol. 912 (1988), p. 139-144.

⁶⁵Bamford, D. J., Jusinski, L. E., and Bischel, W. K., Absolute Two-Photon Absorption and Three-Photon Ionization Cross Sections for Atomic Oxygen. *Phys. Rev. A*, 1986, **34**, 185-198.

⁶⁶Fletcher, D. G., Arcjet Flow Properties Determined from Laser-Induced Fluorescence of Atomic Nitrogen. 36th Aerospace Sciences Meeting and Exhibit, AIAA Paper 98-0205, January 1998.

⁶⁷Goehlich, A., Kawetzki, T., and Döbele, H. F., On Absolute Calibration with Xenon of Laser Diagnostic Methods Based on Two-Photon Absorption. *J. Chem. Phys.*, 1998, **108**, 9362-9370.

⁶⁸Niemi, K., Gathen, V. S.-v. d., and Döbele, H. F., Absolute Atomic Oxygen Density Measurements by Two-Photon Absorption Laser-Induced Fluorescence Spectroscopy in an RF-Excited Atmospheric Pressure Plasma Jet. *Plasma Sources Science and Technology*, 2005, **14**, 375-386.

⁶⁹Niemi, K., Gathen, V. S.-v. d., and Döbele, H. F., Absolute Calibration of Atomic Density Measurements by Laser-Induced Fluorescence Spectroscopy with Two-Photon Excitation. *Journal of Physics D: Applied Physics*, 2001, **34**, 2330-2335.

⁷⁰Koch, U., Gülhan, A., and Esser, B., "Two Dimensional Spatially Resolved Two Photon Oxygen Atom Laser Induced Fluorescence Measurements in the Flow Field of the Arc Heated Facility L3K." in *Proceedings of the Fifth European Symposium on Aerothermodynamics for Space Vehicles (SP-563)*, edited by D. Danesy, (European Space Agency, Noordwijk, The Netherlands, 2005), p. 493.

⁷¹Canosa, A., Le Picard, S. D., and Geppert, W. D., Experimental Kinetics Study of the Reaction of Boron Atoms, $B(^2P_J)$, with Ethylene at Very Low Temperatures (23-295K). *J. Phys. Chem. A*, 2004, **108**, 6183-6185.

⁷²Stanton, C. T., Garland, N. L., and Nelson, H. H., Temperature Dependence of the Kinetics of the Reaction $BO + O_2$. *J. Phys. Chem.*, 1991, **95**, 8741-8744.

⁷³Hinchen, J. J., Kinetics for Quenching and Relaxation of Boron Oxide. *J. Chem. Phys.*, 1993, **99**, 4403-4410.

⁷⁴Takahara, A., Tezaki, A., and Matsui, H., Production of SiO and $Si(^3P)$ in the Reaction of Silane with $O(^1D)$. *J. Phys. Chem. A*, 1999, **103**, 11315-11320.

⁷⁵Okano, A. and Takayanagi, K., Laser-Induced Fluorescence from Collisionally Excited Si Atoms in Laser Ablation Plume. *J. Appl. Phys.*, 1999, **86**, 3964-3972.

⁷⁶Walkup, R. E. and Raider, S. I., *In Situ* measurements of $SiO(g)$ Production During Dry Oxidation of Crystalline Silicon. *Appl. Phys. Lett.*, 1988, **53**, 888-890.

⁷⁷Feigl, M. and Auweter-Kurtz, M., Investigation of SiO Production in Front of Si-Based Material Surfaces to Determine the Transition from Passive to Active Oxidation using Planar Laser-Induced Fluorescence. 35th AIAA Thermophysics Conference, AIAA Paper 2001-3022.

⁷⁸Tang, S., Deng, J., Wang, S., and Liu, W., Comparison of Thermal and Ablation Behavior of C/SiC Composites and C/ZrB₂-SiC Composites. *Corrosion Science*, 2009, **51**, 54-61.

⁷⁹Philippe, L. and Hanson, R., Tunable Diode Laser Absorption Sensor for Temperature and Velocity Measurement of O_2 in Air Flows. 29th AIAA Aerospace Sciences Meeting and Exhibit, AIAA Paper 91-0360, January 1991.

⁸⁰Koch, U., Riehmer, J., Esser, B., and Gülhan, A., "Laser Induced Fluorescence and Diode Laser Absorption Spectroscopy Measurements in CO/CO₂ Hypersonic Flow of LBK." in *Proceedings of the Sixth European Symposium on Aerothermodynamics for Space Vehicles (SP-659)*, edited by H. Lacoste and L. Ouwehand, (European Space Agency, Noordwijk, The Netherlands, 2009).

⁸¹Studer, D. and Vervisch, P., Raman Scattering Measurements Within a Flat Plate Boundary Layer in an Inductively Coupled Plasma Wind Tunnel. *J. Appl. Phys.*, 2007, **102**, 03303-1-8.

APPENDIX 4

Material Property Requirements for Analysis and Design of UHTC Components in Hypersonic Applications*

Thomas H. Squire

Thermal Protection Materials & Systems Branch
NASA Ames Research Center, Moffett Field, California 94035

and

Jochen Marschall

Molecular Physics Laboratory
SRI International, Menlo Park, California 94025

Abstract

Analytical modeling of thermal and mechanical response is a fundamental step in the design process for ultra-high temperature ceramic components, such as nose tips and wing leading edges for hypersonic applications. The purpose of the analyses is to understand the response of test articles to high-enthalpy flows in ground tests and to predict component performance in particular flight environments. Performing these analyses and evaluating the results require comprehensive and accurate physical, thermal, and mechanical properties. In this paper, we explain the nature of the analyses, highlight the essential material properties that are required and why they are important, and describe the impact of property accuracy and uncertainty on the design process.

1. Introduction

Certain characteristics of ultra-high temperature ceramic (UHTC) materials containing transition metal borides and carbides give them a potential advantage over more traditional materials for use in hypersonic applications. In particular, hafnium and zirconium diborides and carbides, as well as their oxides, hafnia and zirconia, have extremely high melting points, all in excess of 2500 °C (4530°F).¹ While HfC and ZrC have higher melting points than HfB₂ and ZrB₂, the diborides have substantially higher thermal conductivities than the carbides.^{2,3} This combination of high-temperature capability and high thermal conductivity make HfB₂ and ZrB₂ particularly attractive for use in sharp wing leading edges (WLEs) and nose tips.⁴ In practice, the high-temperature oxidation resistance of pure diboride materials is not sufficient for aerothermal flight environments. The best oxidation performance is found for monolithic materials hot-

* This Appendix is an edited version of the manuscript published in The Journal of the European Ceramic Society, Vol. 30, 2010, pp. 2239-2251.

pressed from mixtures of ceramic powders containing a silica former as a minor component.^{5,6} The most common compositions typically contain 10 to 30 volume percent SiC,⁷⁻¹² although other silica formers like MoSi₂ and TaSi₂ have also been investigated.¹³⁻¹⁶

The design of high-performance hypersonic vehicles generally involves relatively sharp nose tips and WLEs. (An arcjet model of a concept UHTC WLE section is shown in Fig. 1.) While not an achievable design in practice, in the context of supersonic flow theory, a “sharp” leading edge is one with zero radius of curvature. In a practical design context, “sharp” usually refers to a leading edge radius that is much smaller than the nose, wing, or vehicle length scale, while “blunt” implies the converse.

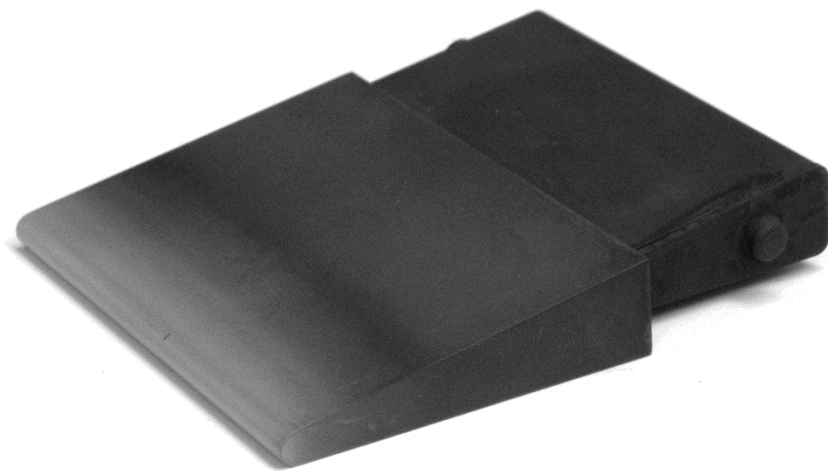


Fig. 1. UHTC wing leading edge arcjet model.

Sharp leading edges help reduce the vehicle’s drag, enhance maneuverability and performance, and also improve safety due to an increased cross-range capability.¹⁷ The WLE of the Space Shuttle orbiter has a radius of approximately 10 cm at the tip, while design concepts for some hypersonic maneuvering vehicles, such as the one under development in Defense Advanced Research Projects Agency (DARPA)’s Falcon program, have leading edge radii on the order of millimeters. The challenge with sharp WLE designs is that the convective heating to the surface, and hence the surface temperature, increases as the WLE radius decreases. The surface temperature on the stagnation region of such sharp leading edges can potentially exceed 2000 °C (3632 °F). Few materials can survive extended periods at these temperatures and retain their dimensional and structural integrity in an aggressive oxidizing flow environment.

The performance advantage of diboride-based UHTC materials comes not only from their high-temperature capability, but also from their high thermal conductivity. Convective energy that enters the surface near the stagnation region is conducted away to cooler regions of the leading edge, where it can be radiated back to the environment (Fig. 2). The higher the thermal conductivity of the leading edge material, the more efficient this process becomes.¹⁸ The UHTC

leading edge then behaves much like a passive heat pipe, to move energy through, and eventually out of, the system.

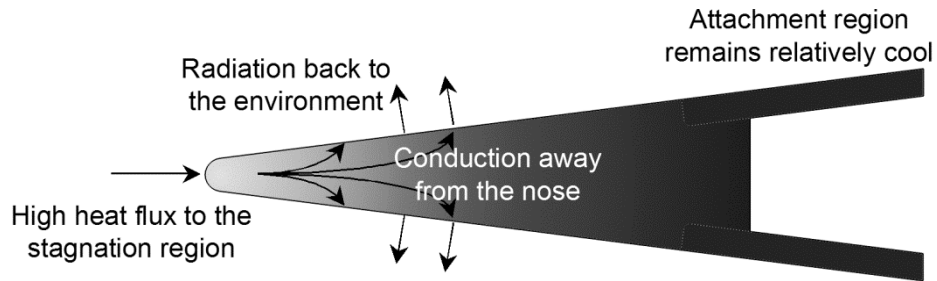


Fig. 2. UHTC leading edge thermal management concept.

The hypersonic applications of UHTC materials involve complex interactions between the material and the aerothermodynamic environment. Although most designers would choose to build concept vehicles and conduct flight tests in relevant environments, such testing opportunities are rare, often impractical, and always very expensive. Consequently, the design process for UHTC components for hypersonic vehicles is heavily dependent on computational methods and ground-based testing. Analytical performance predictions and the interpretation of ground-based testing require a self-consistent set of accurate material properties with well-defined uncertainties. Because UHTC components have to operate in environments from room temperature to nearly 2000 °C (3630°F), it is important that most UHTC properties be measured over this entire temperature range.

The purpose of this paper is to describe the material properties that are most important for UHTC component design and the reasons why. Section 2 provides a brief introduction to hypersonic aerothermodynamics; to understand why a UHTC material might be used in a hypersonic application, materials developers must have at least a basic understanding of the hypersonic flight environment. Section 3 provides an overview of the design process and how it is influenced by material property uncertainties. Section 4 describes general materials information useful for designers and analysts. Section 5 discusses specific material properties and how they influence the design and analysis of the UHTC components. Section 6 provides a simple numerical example of how property uncertainties can impact the design space. Finally, Section 7 summarizes the conclusions and provides recommendations to UHTC material developers.

2. Summary of Hypersonic Aerothermodynamics

The analysis, design, and testing of UHTC components is driven by the hypersonic aerothermodynamic environment in which they are to be used. Generally, the term “hypersonic” refers to speeds in excess of Mach 5, or more than five times the speed of sound in the gas

medium. Vehicles transiting an atmosphere at hypersonic speeds are exposed to extreme convective heating from high-enthalpy gas flowing past the vehicle. In some flight regimes, radiative heating for hot gases can also be important. This section serves as a brief introduction to the fundamental aspects of hypersonic flow.

2.1 Shock and boundary layers

At hypersonic speeds, a bow shock forms in front of the nose tip or WLE (Fig. 3). The stagnation point is the location on the leading edge, facing directly into the flow. The shock standoff length defines the distance between the bow shock and the stagnation point. Gases passing through the bow shock are compressed and increase in density, pressure, static enthalpy, and temperature. At sufficiently high enthalpies, the gas may become dissociated and ionized. In air, dissociation means that the N_2 and O_2 molecules break apart to become highly reactive N and O atoms. Because of their lower bond energy (5.1 vs. 9.8 eV), O_2 molecules dissociate at lower enthalpy levels than N_2 molecules. The exothermic recombination of these atoms at the surface can contribute significantly to the total aerothermal heating experienced by a component, depending on the particular flight or test environment.

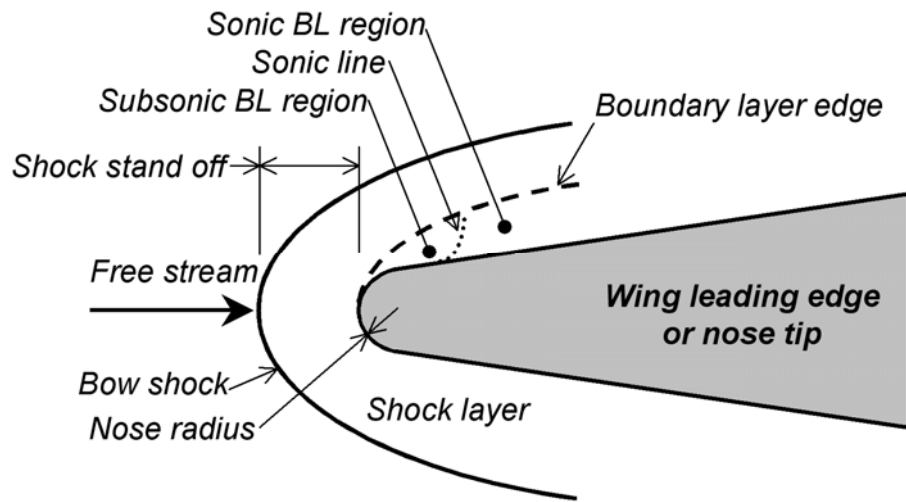


Fig. 3. Hypersonic flow features.

When the high-enthalpy gas formed in the bow shock impinges on the leading edge, a boundary layer forms along the surface of the component (Fig. 3). The boundary layer region is characterized by large temperature, momentum, and chemical composition gradients normal to the surface. The gas flow is decelerated at the stagnation point, forming a thin boundary layer and a local subsonic region. The boundary layer thickens as the flow is redirected and accelerates around the WLE or nose tip, regaining supersonic velocities. Boundary layer conditions

determine local convective heating to the surface. Convective heating is typically highest in the stagnation point region and decreases, often significantly, away from the stagnation point.

2.2 Surface energy balance

The wall temperature on a hypersonic vehicle is determined by an energy balance that accounts for all of the heat transfer processes transporting energy into and out of the surface. Figure 4 is a schematic of a steady-state energy balance at the surface, considering convective heating from the boundary layer, chemical heating from surface recombination reactions, re-radiation into the ambient environment, and conduction into the interior of the material.

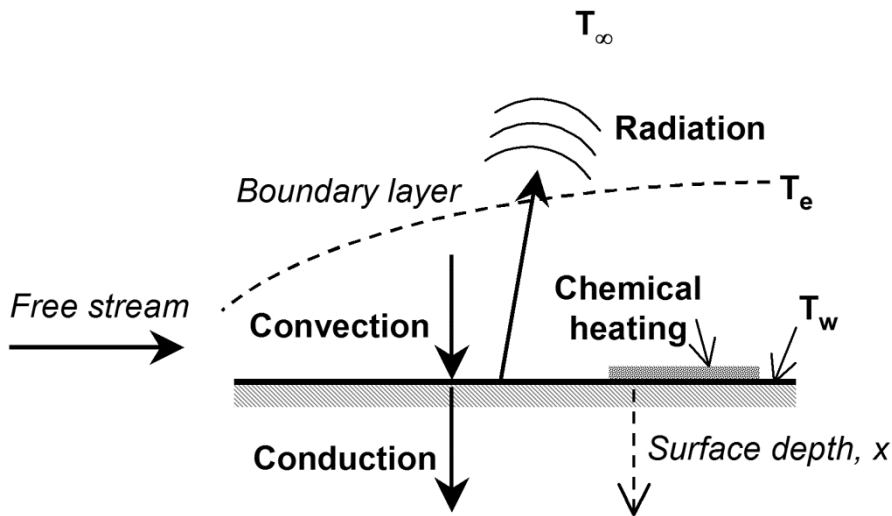


Fig. 4. Surface energy balance.

The sensible convective heat flux to the surface, \dot{q}_{conv} , can be defined as a function of the gas enthalpy at the edge of the boundary layer, h_e , the enthalpy of the gas at the wall, h_w , and a transfer coefficient, C_H . The expression for convective heat flux can be written as

$$\dot{q}_{conv} = C_H [h_e(T_e) - h_w(T_w)], \quad (1)$$

where T_e is the boundary layer edge gas temperature and T_w is the temperature of the wall (surface).

The transfer coefficient is a function of the boundary layer conditions, which are dependent on the free stream conditions (speed, temperature, and pressure), the gas composition, and the geometry of the leading edge. The transfer coefficient is also a function of whether the boundary layer flow is laminar or turbulent. Turbulence can significantly increase the convective heating to

the surface. Hypersonic aircraft are usually meticulously designed to avoid turbulent flow and prevent laminar boundary layers from becoming turbulent. The roughness of the surface material can be a critical aspect of transition to turbulence; this will be addressed in Section 5.

High levels of dissociated gases can be present in flight and also in the free streams of high-enthalpy test facilities, including arcjets and inductively-coupled plasma wind tunnels, such as the Plasmatron at the von Karman Institute for Fluid Dynamics in Belgium. The diffusion of these species to the surface, and their exothermic heterogeneous reaction on or with the surface material, can transfer additional energy to the surface. Gas-surface chemical interactions can be quite complex, and approximate computational models are almost always used. A simplified model of chemical heating that considers only independent oxygen and nitrogen surface recombination can be written as

$$\dot{q}_{chem} = \gamma'_O(T_w) \frac{\Delta E_{dis,O_2}}{2} \Gamma_O + \gamma'_N(T_w) \frac{\Delta E_{dis,N_2}}{2} \Gamma_N , \quad (2)$$

where γ' is the total catalytic recombination efficiency, Γ_i is the surface impingement flux for reactant species i , and $\Delta E_{dis,j}$ is the dissociation energy of product j . The total catalytic recombination efficiency (γ') is the product of the species recombination efficiency, γ , and the energy accommodation efficiency, β . The species recombination efficiency (γ) is the fraction of collisions with the surface that result in loss of the reactant from the gas phase, and the energy accommodation efficiency (β) is the fraction of exothermic reaction energy that is transferred to the surface. For independent reactions γ' , γ and β may all vary from a minimum of 0 to a maximum of 1. The surface impingement flux, Γ_i , is typically taken as the gas kinetic expression $n_i \sqrt{RT_w/2\pi M_i}$, where R is the universal gas constant, and n_i and M_i are the number density and molar mass of the reactant, respectively.

The re-radiation away from the surface is a function of the wall temperature, the environment temperature, T_∞ , the Stefan-Boltzmann constant, σ , and the emissivity, ε , and can be expressed by the Stefan-Boltzmann relationship

$$\dot{q}_{rad} = \varepsilon(T_w) \sigma [T_w^4 - T_\infty^4] . \quad (3)$$

The emissivity may vary from 0 to 1; $\varepsilon = 1$ for a perfect blackbody radiator.

Energy conduction into the interior is a function of the local temperature gradient into the surface and the thermal conductivity, k , of the material through Fourier's law:

$$\dot{q}_{cond} = -k(T_w) \frac{dT}{dx} \Big|_w . \quad (4)$$

The steady-state surface energy balance equates the total aerothermal heating of the surface ($\dot{q}_{conv} + \dot{q}_{chem}$) to the energy transferred away from the surface ($\dot{q}_{rad} + \dot{q}_{cond}$):

$$C_H [h_e(T_e) - h_w(T_w)] + \gamma'_O(T_w) \frac{\Delta E_{dis,O_2}}{2} \Gamma_O + \gamma'_N \frac{\Delta E_{dis,N_2}}{2} (T_w) \Gamma_N = \epsilon(T_w) \sigma [T_w^4 - T_\infty^4] - k(T_w) \frac{dT}{dx} \Big|_w \quad (5)$$

The surface energy balance can be used to compute the surface temperature, given the conditions of the flow, environment, and material properties. The actual solution of the expression is complicated by the fact that the properties of real materials, such as UHTCs, are functions of temperature. Moreover, Eq. (5) is a simplification of the more general case, which might also include radiation transfer to the surface from hot gases in the shock layer, more complicated surface reactions, as well as energy storage effects associated with transient heating conditions. Generally, the solution is part of a large numerical thermal analysis using computational fluid dynamics (CFD) programs and involving multidimensional geometry and time-dependent boundary conditions that are usually provided by an independent solution of the flow field and boundary layer.

The significance of Eq. (5) for material scientists is that the surface temperature experienced by a UHTC component during hypersonic flight or high-enthalpy flow testing is determined not only by the environment and vehicle or component shape, but also by temperature-dependent material properties, such as emissivity, thermal conductivity, and catalytic efficiency (as well as absorbance and heat capacity in the more general case).

2.3 Approximate analyses and estimates

Because of the coupled nature of the surface energy balance, complicated numerical analyses are typically required for accurate solutions. However, two approximate analyses are in common use, particularly in the early stages of vehicle or mission design.

Hypersonic aerothermal environments are often quantified in terms of a heat flux to the vehicle surface. For example, vehicle designers may specify that a candidate leading-edge material must sustain a particular peak stagnation-point heating rate. The transfer coefficient and boundary layer edge temperature are relatively insensitive to the thermal conditions at the wall and are often predicted independent of the wall conditions, using CFD codes or engineering correlations, together with information about the free-stream conditions and the nose tip or WLE geometry. One common approximation for the aerothermal heat flux is to ignore the surface

energy balance and calculate heating directly from the left hand side of Eq. (5), assuming a fixed, low-wall temperature, typically 300 K, and fully catalytic behavior ($\gamma' = 1$).

The heat flux defined in this way is referred to as $\dot{q}_{fc,cw}$, a “fully catalytic cold-wall” heat flux. The advantage of this definition is that $\dot{q}_{fc,cw}$ is only a function of the flow conditions (free stream and geometry) and is completely independent of the surface thermal conditions. It provides a common reference point for the comparison of different flow environments. In a sense, the fully catalytic cold-wall heat flux represents the energy in the environment that is potentially available to heat the surface. Usually, when aerospace engineers or aerothermodynamicists refer to the “peak heat flux” in a hypersonic flight regime, they are referencing to a fully catalytic, cold-wall value. The fully catalytic, cold-wall heat flux is always higher than the corresponding hot-wall flux in flight, as surface temperatures in flight will typically be much hotter than 300 K, and real materials are not fully catalytic.

The distinction between cold-wall and hot-wall heat flux is also important when evaluating material performance in ground-test environments. For example, test conditions in arcjet or Plasmatron wind tunnels are routinely characterized using water-cooled copper calorimeters, whose surface temperatures remain near room temperature during the measurement.^{19,20} Such a measurement is essentially a cold-wall heat flux measurement on a highly catalytic surface. The heat flux experienced by the test specimen under the identical flow conditions will be a hot-wall heat flux, on a surface that is probably much less catalytic than copper.

A second common approximation, useful for quickly estimating thermal response to a prescribed heat flux, is the “radiation equilibrium temperature.” This approximation simplifies the surface energy balance by assuming negligible heat conduction into the material ($\dot{q}_{cond} = 0$) and a constant value for aerothermal heat flux, often a fully catalytic, cold-wall heat flux value obtained as described above. With these assumptions, the energy balance can be rearranged as an algebraic equation for T_w :

$$T_w = \sqrt[4]{\frac{\dot{q}_{fc,cw}}{\varepsilon\sigma} + T_\infty^4} . \quad (6)$$

Since Eq. (6) ignores the effect of heat conduction into the interior, the radiation equilibrium temperature generally represents the maximum potential surface temperature for a given heat flux condition, assuming a conservative (low) value of surface emissivity is used. The radiation equilibrium temperature can be a valuable engineering level tool for quickly estimating thermal response and as a sanity check for validating computational analyses. However, the approximation of zero heat conduction is generally not valid for materials with relatively high thermal conductivities, such as metals or UHTCs. As discussed previously, high thermal conductivity is one of the enabling properties of diboride-based UHTC materials, because it allows heat to be drawn out of the stagnation region and re-radiated from a larger surface area.

Thus, a radiative equilibrium temperature may significantly overestimate the steady-state surface temperature in the stagnation point region of a sharp UHTC nose tip or WLE.

2.4 Computational methods

Predicting the aerothermal conditions and material thermal response of a UHTC component in a hypersonic vehicle design usually requires the application of numerical computations. Even for simple sphere-cone geometries, the flow conditions and thermal response are too complex to evaluate with direct analytical methods. In a real aerothermal flight environment, the thermal conditions at the material surface and the boundary layer conditions are interdependent. However, for dimensionally stable (non-ablating, non-pyrolyzing) thermal protection systems, this interaction is often weak, when compared to the effect that the free-stream flow conditions and vehicle shape have on the boundary layer. Under these conditions, it is preferable to perform design computations in which the numerical analyses of the flow conditions and the material thermal response are performed independently — and in which the interface between the fluid and solid regions is treated as a boundary condition in each of the independent analyses.

NASA uses computational fluid dynamics programs, such as the Data Parallel Line Relaxation (DPLR) program²¹ or the Langley Aerothermodynamic Upwind Relaxation Algorithm (LAURA),²² to predict the flow conditions around a vehicle traveling a particular flight trajectory through the atmosphere. These programs solve the Navier-Stokes equations and can predict the dynamic, thermodynamic, and chemical conditions in the shock layer and boundary layer, as well as provide the surface heat flux as a boundary condition to the materials response model. Material response analyses employ finite-difference, finite-volume, or finite-element methods to perform computations as a function of transient heating. NASA Ames Research Center uses the commercial finite-element MSC.Marc package^{23,24} to predict the transient surface and in-depth thermal response of UHTC nose tip and WLE components. Other researchers have used the commercial codes ABAQUS,²⁵ COMOS/M, COSTAR,²⁶ and ANSYS^{27,28} to model UHTC thermal and mechanical response.

The complexity associated with the prediction of material response along a flight trajectory is highly dependent on the level of coupling between the flow field and material analyses. Decoupled solutions are obtained by setting surface temperatures to either cold-wall or radiative equilibrium values in the CFD analyses and then using the computed transient convective heating profile as a boundary condition to a material response model. In this approach, no material properties are required for the flow field analysis, if the surface temperature is set to an arbitrary cold-wall value, and only the surface emissivity is required if the radiative equilibrium temperature assumption is used. Although the radiation equilibrium temperature generally over predicts the actual surface temperature, the estimate is usually much closer than assuming a cold wall.

However, for sharp UHTC components, the combination of high thermal conductivity, multi-dimensional heat conduction, and significant volumetric heat capacity, often necessitates some level of coupling between the flow field and material response computations, in order to achieve

time-accurate predictions for temperature and stress in a transient aerothermal heating environment. Loose coupling is achieved by incrementing flow field and material response computations sequentially during each time step, while full coupling requires the iterative solution of the flow field and material responses to satisfy the full surface-energy balance during every time step. For trajectory-based design space studies, solution of the full Navier-Stokes equations is sometimes replaced by more approximate analytic-flow correlations and boundary-layer solutions to make the computations more tractable.²⁴ Requirements for the level of coupling to achieve time-accurate solutions for UHTC components are discussed in the literature.^{24,29,30}

3. The Design Process and Property Uncertainty

Hypersonic vehicle designs are driven by mission objectives that demand certain performance criteria. Designers attempt to fulfill these criteria in a constrained optimization process, adjusting the shape and mass of a vehicle to achieve the desired flight characteristics, while simultaneously remaining within bounds imposed by the properties of available aerospace materials. Material property uncertainties, along with the variations or dispersions in the other parameters, such as aerothermal heating or aerodynamic loads, are used to define the design space, assess the design against system requirements, and determine margins or factors of safety. Components and systems must “buy” their way onto a vehicle design by proving that they are lower risks than competing systems. Reducing uncertainties in material properties reduces the risks in the design — risks associated with component failure, mission failure, or loss of the vehicle. The aerospace industry maintains standards that define the design process and the role that material properties play in that process. NASA has developed its own standards for the design and assessment of spaceflight hardware and thermal protection system design.³¹⁻³⁴

An important early step in the design process is defining and selecting the specific set of material property values that will be used in analyses. The design team must evaluate different data sources and select the data sets deemed most directly applicable and reliable for the given application. Often this step includes down selection from a large property database, like NASA’s TPSX Material Properties Database.³⁵ The availability and quality of property uncertainties associated with different data sets is always a key criterion for this down-selection process. At this stage, the lack of quality uncertainty information or specific experimental data often dictates that new property measurements be made.

Material property data are usually provided as either compiled statistical values, such as a mean and standard deviation on a particular property, or as a set of data points from which the statistical values can be derived. It is typical for designers to use bounding values of ± 3 standard deviations (3σ) to define the dispersions in the design. A large variation in a measured property may mean that the 3σ values push some design parameters beyond acceptable limits. Some specific approaches for the use of property uncertainty data include performing sensitivity studies, in which material properties are parameters that are varied in a regular pattern to ascertain their effect on the thermal and mechanical response of the system. A common application of this approach is to assess the system with a “worst-on-worst” combination of

material properties and flight loads. Another approach uses a Monte Carlo simulation to run a large number of analyses, randomly varying material properties and other design parameters based on their nominal values and standard deviations.³⁶ These analyses are very effective for identifying the parameters that have the largest influence on the system performance.

4. General Material Information

Before proceeding to a discussion of specific material properties used in design computations, it is helpful to outline the general material information that designers and analysts need when developing hypersonic vehicles. This information is useful in assessing the results of analyses or in determining the potential applicability of a material.

4.1 Sources of uncertainty

Multiple tests for the same material property usually yield a distribution of values, even for relatively easy-to-measure properties such as density. Designers need to know these distributions, in order to define bounding cases and dispersions in the design space. Distributions in material properties arise from a variety of sources, including manufacturing variability, the use of different techniques to derive the same material property, and inherent uncertainties in different measurements techniques.

No material manufacturing process is perfectly reproducible. Lot-to-lot variations are expected and tolerated (within certain limits). UHTC materials are certainly no exception to this rule. Manufacturing processes, such as hot pressing of ceramic powders, are defined by a large number of variables that can only be controlled within certain tolerances. Even under nominal processing conditions, acceptable material lots will have properties that vary about some average value. It is also common for materials manufactured in a pressing, molding, or casting process to exhibit non-uniform material properties within a single billet. Such non-uniformities can occur, for example, near surfaces, due to interactions with die or mold surfaces, or along directions aligned with the application of stresses or gravity that cause segregation of constituents.¹² It is important for materials researchers to quantify both inter-billet and intra-billet property distributions.

Whenever possible, multiple material property measurements should be made on specimens from the same billet or manufactured from the same lot of starting material. Such data are more valuable than properties measured on specimens from different starting billets or material lots, because they allow material developers and vehicle designers to determine correlations among material properties and to estimate trends in manufacturing.

Consistency in test specimens is also important for any material property derived from combinations of separate test data. For example, the thermal conductivity is related to the density, ρ , specific heat, c_p , and thermal diffusivity, α , by the relationship

$$k = \alpha \rho c_p \quad . \quad (7)$$

Thermal diffusivity is often measured directly at high temperature using laser-flash techniques,³⁷ but it is usually thermal conductivity that is required as an input to thermal analysis programs. The thermal conductivity must then be derived from the measurements of density, specific heat, and diffusivity, and if these properties are measured on unrelated samples, the calculation of thermal conductivity may result in inconsistent values at best, or, even worse, significantly inaccurate values.

Many material properties can be measured with a variety of experimental techniques. Often these techniques and their associated data reduction procedures are quite different. For example, tensile modulus can be measured by acoustic techniques or mechanical tests; fracture strength can be measured in tension, compression, or bending geometries; thermal conductivity can be obtained directly using steady-state methods like guarded hot-plate testing, or indirectly, by transient methods like laser-flash or photothermal radiometry, which measure thermal diffusivity.

It is important to describe or reference measurement methods well, so that informed judgments can be made and discrepancies among different property values resolved. In this regard, standard measurement techniques, such as those defined by the American Society for Testing and Materials (ASTM), are desirable, because both the measurement procedure and uncertainty are defined in the standard. The use of nonstandard techniques should be avoided, whenever possible, because uncertainty is more difficult to assess.

In summary, the more information supplied to the designer about how a property was measured and what sources of uncertainty are incorporated into quoted errors, the tighter the resulting design space. Missing information inevitably forces analysts to assume conservative uncertainties that may vastly exceed those that actually exist.

4.2 Material morphology

UHTC materials are often referred to as monolithic and are treated as having homogeneous properties. But a micrograph of an HfB₂-SiC UHTC sample (Fig. 5) clearly shows the composite nature of the material. Microstructure significantly influences the properties of a material through the distribution of different material phases and the location and size of defects and voids. Information about material microstructure can help analysts interpret the macroscopic performance of the material and is particularly useful in understanding and predicting failure modes.

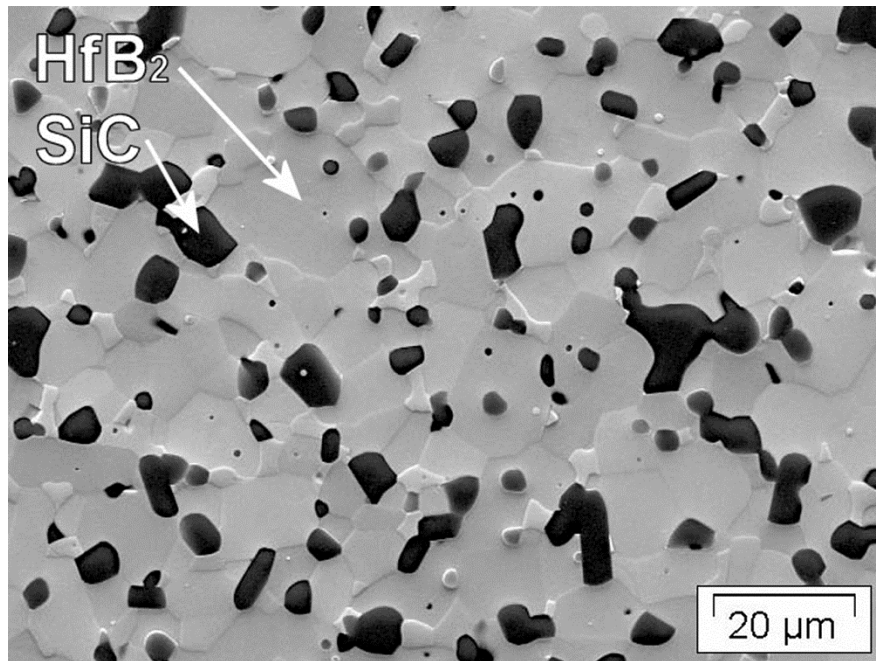


Fig. 5. Scanning electron micrograph of a HfB₂ UHTC composite containing 20 volume percent SiC; the light grains are HfB₂ and the dark grains are SiC.

An important aspect of material morphology is the introduction of anisotropic material properties. Many aerospace materials, such as carbon fiber composites or rigid ceramic tile insulations, exhibit direction-dependent thermal and mechanical properties. Generally, these materials fall into two categories: orthotropic materials with properties oriented in three mutually orthogonal directions, and transverse isotropic materials, with properties oriented in two orthogonal directions, though-the-thickness and in-plane. Most hot-pressed UHTCs are treated as isotropic in analysis and design, but it is important for material developers to investigate the directional dependence and verify that the isotropic assumption is valid. Failure to incorporate significant orthotropic or transverse isotropic properties in analyses can lead to erroneous predictions of thermal and mechanical performance and, ultimately, poor component design.

4.3 Material use limits

Some material parameters are not measured directly, but are determined by material performance. Maximum temperature limits and maximum stress limits are examples of such parameters. Designers need to establish these limits based on an analysis of a collection of material properties and behaviors.

Obviously, the extreme upper temperature limit is set by a material's melting point or eutectic temperature. However, a hypersonic vehicle designer will never expect to use a material up to that temperature. Instead, the designer needs to define a practical temperature limit beyond which the thermal, mechanical, and other properties are potentially degraded to such a point that

the material can no longer perform its required function. The material composition, although not used directly in design computations, can be useful information in defining capabilities and material limits. For example, if any of the material components are susceptible to oxidation, it is important to know the temperature at which oxidation rates become significant. Such information would not be used directly in a computational analysis, but may affect the operational limits of the vehicle or may demand that components be coated with an oxidation barrier.

The mechanical performance constraints may be associated with more than one type of stress limit, depending on the mode of loading: tensile, compressive, or shear. Maximum stress limits are usually obtained from mechanical failure data. While the thermal and electrical properties of UHTC materials are somewhat “metallic” in nature, the failure characteristics are more typical of the brittle fracture of a ceramic. Most fracture strength data on UHTC materials are obtained in flexure testing.^{10,12,38-42} UHTC fracture strengths tend to decrease with increasing temperature.

Because it is difficult to perform failure-prediction analyses of brittle materials, analysts generally perform standard mechanical or thermal/mechanical analyses and then compare the predicted stress results with experimentally measured mechanical strength values. For brittle materials, this may be in the form of statistical data, such as Weibull^{12,43} Designers will usually apply some factor of safety to the strength values and use those marginated values for comparison with mechanical analyses. If mechanical strength data are not accurate or extensive enough to generate robust statistics, the designers may be required to apply a higher factor of safety to cover the uncertainty, which can lead to overly conservative designs.

In general, material developers need to provide enough accurate material property data under sufficiently stressful testing conditions so that proper use limits can be established to within an acceptable uncertainty. Testing UHTC materials and components at very high temperatures and past the point of failure are import aspects of material characterization.

4.4 Properties not used in component analyses

There are many properties commonly reported for UHTC materials that are not directly useful for thermal or mechanical analyses. Some examples are hardness or microhardness^{5,12,44,45} fracture toughness,^{10,39,41,46-49} and thermal shock parameters.^{5,11,50} These properties can be valuable indicators for tracking processing-related changes and for optimizing desired properties or capabilities in UHTC materials. They can also be helpful when screening candidate materials for particular applications and for assessing performance issues, such as damage resistance during handling or shipping. However, properties like hardness, fracture toughness, and thermal shock resistance, are of marginal importance in design computations, as their numerical values are never input directly into any analyses.

5. Specific Material Properties

The design and analysis of UHTC components for hypersonic applications ultimately require numerical values of specific physical, thermal, mechanical, and surface properties. The important material properties discussed below appear directly in either boundary conditions like Eq. (5) or in governing equations for heat transfer and mechanical equilibrium. Some examples of governing equations for an isotropic material are the energy conservation equation

$$\rho c_p \frac{\partial T}{\partial t} = \frac{\partial}{\partial x} \left(k \frac{\partial T}{\partial x} \right) + \frac{\partial}{\partial y} \left(k \frac{\partial T}{\partial y} \right) + \frac{\partial}{\partial z} \left(k \frac{\partial T}{\partial z} \right), \quad (8)$$

which relates the energy storage rate to heat flux gradients within a material, and Hooke's law,

$$\begin{bmatrix} \varepsilon_{xx} \\ \varepsilon_{yy} \\ \varepsilon_{zz} \\ \varepsilon_{yz} \\ \varepsilon_{zx} \\ \varepsilon_{xy} \end{bmatrix} = \frac{1}{E} \begin{bmatrix} 1 & -\nu & -\nu & 0 & 0 & 0 \\ -\nu & 1 & -\nu & 0 & 0 & 0 \\ -\nu & -\nu & 1 & 0 & 0 & 0 \\ 0 & 0 & 0 & 1+\nu & 0 & 0 \\ 0 & 0 & 0 & 0 & 1+\nu & 0 \\ 0 & 0 & 0 & 0 & 0 & 1+\nu \end{bmatrix} \begin{bmatrix} \sigma_{xx} \\ \sigma_{yy} \\ \sigma_{zz} \\ \sigma_{yz} \\ \sigma_{zx} \\ \sigma_{xy} \end{bmatrix}, \quad (9)$$

which relates the elastic strains, ε_{ij} , and stresses, σ_{ij} , within a material through the tensile modulus, E , and the Poisson's ratio, ν .

Because UHTC materials in hypersonic vehicle applications are required to operate at very high temperatures, designers and analysts will require that most of the properties discussed below be provided as a function of temperature over the entire temperature range of interest. Measuring material properties at high temperatures is always difficult and sometimes impossible. In such cases, material developers should provide estimates of high-temperature properties based on engineering judgment, similarity with other materials, or extrapolation of existing data. Whatever approach is used, an estimate of the uncertainty or error in the high-temperature properties should also be provided.

5.1 Physical properties

The most important physical properties for UHTC materials are the density and the coefficient of thermal expansion (CTE).

Density appears as a first order term in the governing equations for thermal and dynamic mechanical response (for example, vibration). Because variations in density have a large effect on the thermal and dynamic mechanical performance of components, material developers should provide as accurate a value as possible with as tight a tolerance as possible. It should be possible to make individual density measurements with measurement errors less than 1%. Density also

determines the mass (weight) of a component, which is always a critical aspect of the design. UHTC materials are much denser than typical aerospace materials, such as carbon composites or aluminum alloys, and managing the total and distributed mass of a vehicle is one of the most important functions of the designer. Typical designs for UHTC wing leading edges and nose tips require very little material, due to the high temperature capability and high thermal conductivity. Additionally, the location of the high density UHTCs at the forward end of the vehicle can have the beneficial effect of moving the center of gravity further forward, which often results in better aerodynamic stability.

Most materials exhibit changes in density as a function of temperature associated with thermal expansion. The effects of density changes on heat transfer performance are usually negligible. In the analysis of thermo-mechanical responses, the thermal expansion behavior of a material is typically incorporated in the linear coefficient of thermal expansion (CTE). The CTE is a critical material property. Local thermal expansion within a UHTC component can produce large internal strains and stresses, particularly under conditions that cause rapid temperature changes. Differential thermal expansion between a UHTC component and a neighboring material can cause undesirable contact stresses. Thermally induced stresses often limit the size and shape of a UHTC component. When predicted thermal stresses approach maximum allowable stress limits, conditions for thermal shock failure exist and components may have to be redesigned to dissipate heat more effectively. This generally means making smaller UHTC components with lower aspect ratios. For non-isotropic materials, the CTE must be provided in each of the primary material directions.

The CTE is usually derived from measurements of the elongation of a material at elevated temperatures. Because the CTE is the first derivative, or slope, of the curve of elongation versus temperature, measurements must be performed with sufficient resolution to extract this derivative, without introducing undesirable artifacts into the CTE values. The CTE can also be obtained for pure crystalline materials using X-ray diffraction techniques to measure changes in lattice constants with temperature. Often the thermal expansion behavior over a large temperature range is non-linear and must be defined by several average CTE values over sequential temperature intervals. Typical CTE values for ZrB_2 and HfB_2 composites lie in the $5\text{--}8 \times 10^{-6} \text{ K}^{-1}$ range, with the higher values found at higher temperatures.^{11,12,48,49,51}

5.2 Thermal properties

The most important thermal properties for UHTC materials are the specific heat and the thermal conductivity. Both properties appear as first-order terms in the governing conservation-of-energy equation.

The specific heat can have a large effect on the transient thermal response of a UHTC component during heating or cooling. Specific heat is generally a strong function of temperature for UHTC materials, particularly from room temperature up to $\sim 1000^\circ\text{C}$. For example, the specific heat of HfB_2 increases by about a factor of two over this temperature range.⁵² While specific heat values for composite materials can be estimated from measurements performed on

isolated constituents, values measured directly on the actual material are much preferred. Sample volumes used in calorimetry are often small. For UHTC composites, it is important to ensure that the samples used for specific heat measurements accurately reflect the composition of the bulk material. During high temperature calorimetry, the absence of chemical reactions between UHTC constituents and sample containers must be verified.

Thermal conductivity exerts a dominant effect on heat transfer and coupled thermo-mechanical responses and is a particularly important property for sharp UHTC leading edge components, as the ability to conduct heat away from sharp edges is an enabling characteristic. In general, thermal conductivity can be directionally dependent. If a material exhibits anisotropic behavior, analysts will require thermal conductivity values for all of the primary material orientations.

UHTC materials exhibit thermal conductivities with a wide range of magnitudes and a variety of temperature dependencies.^{3,52} Because the thermal conductivity of UHTC composites depends on many different factors, including microstructure, composition, defect and impurity levels, contact resistance between grains, and porosity, values cannot be estimated with any confidence from published data or measurements performed on individual constituents. Even nominally similar UHTC composites may not have the same heat transport characteristics, because the factors that affect thermal conductivity are largely determined by manufacturing details, for example, the raw ceramic powders sources, powder processing procedures, and hot-pressing schedules.^{12,52} Thus thermal conductivities over the entire temperature range of interest must be measured for the exact UHTC material to be used in a particular component application.

Since most high-temperature thermal conductivity values are actually derived from thermal diffusivity measurements (as previously described), it is important that the specific heat and density values required to extract thermal conductivity from thermal diffusivity be measured on the same lot of UHTC material, preferably the same test specimen, if possible. Typical uncertainties reported for direct UHTC thermal property measurements are $\pm 3\%$ for specific heat,^{13,53,54} $\pm 5\%$ for thermal diffusivity,^{13,53} and $\pm 5\%$ for thermal conductivity.⁵⁵ These uncertainties are associated with measurement technique and the consistency of repeated measurements on the same sample and do not include multiple sample statistics. Note also that if thermal conductivity is calculated from $k = \alpha \rho c_p$, uncertainties in the contributing properties combine and propagate.

5.3 Mechanical properties

The primary mechanical properties required for analyses of isotropic UHTC components are the tensile modulus and the Poisson's ratio. Both appear as first order terms in the governing static equations. For isotropic materials, the shear modulus, G , can be calculated from the tensile modulus and Poisson's ratio as $G = E / [2(1 + \nu)]$ and does not have to be independently specified.

The tensile modulus (also called the Young's modulus or elastic modulus) has a large effect on the mechanical response of the component. Ideally, tensile modulus values are derived from the slope (or first derivative) of a material's stress-strain curve under uniaxial tension in the elastic loading regime. However UHTC materials have very limited ductility, and their tensile moduli are almost always either measured by acoustic methods or derived from experimental stress-strain curves obtained during flexure testing. The flexure method was found to produce somewhat lower (by ~15%) values for some UHTC materials than the tensile and acoustic methods.^{3,56}

Tensile modulus values can be used directly in mechanical analyses, but it is often more accurate to incorporate the actual stress-strain relationship. Most analytical software packages can handle inputs of either type. Incorporating the experimental stress-strain curve is particularly advantageous for materials that exhibit non-linear elastic response or for when the experimental stress-strain curve contains plastic strain contributions deemed important for a particular application. Nonlinear, elastic deformation behaviors are observed for some UHTC materials at elevated temperatures.^{3,40-42,57} The tensile modulus magnitude tends to decrease with increasing temperature. Accurate temperature-dependent modulus data are desirable, but difficult to measure. In practice, if the expected thermal and load environments combine to push a UHTC component into a highly non-linear or highly temperature-dependent mechanical property regime, a redesign of the component or system is likely.

The Poisson's ratio is defined as the ratio of lateral contraction to axial extension under uniaxial loading. It can be measured during a uniaxial tensile test or by acoustic methods. Although the Poisson's ratio does not often have a large influence on the magnitude of predicted stresses and strains in a component, it can significantly affect the distribution and orientation of those stresses and strains. This is particularly important when modeling three-dimensional sharp components subjected to large temperature gradients. Typical values for metals are around 0.3; UHTC materials generally have lower Poisson's ratios, in the 0.1–0.2 range at room temperature.^{10,11,39} The Poisson's ratio does not tend to be highly temperature dependent for real materials, so analysts do not usually require temperature dependent values.

The number of mechanical properties that must be measured increases rapidly with anisotropy. For transverse isotropic materials, two tensile moduli, two Poisson's ratios, and one shear modulus are required, and for orthotropic materials, three tensile moduli, three Poisson's ratios, and three shear moduli are required. As with the tensile modulus, it is desirable to define the temperature-dependent behavior of the shear modulus, but estimates of that behavior are often good enough.

5.4 Surface properties

The three most important surface properties for UHTC materials are the emissivity (or emittance), the catalytic efficiency, and the surface roughness. The first two properties enter into the surface energy balance, while the third influences laminar-to-turbulent transitions in the boundary layer flow.

In the general case, emissivity is a function of wavelength, emission direction, and temperature. The total hemispherical emissivity — a value averaged over all wavelengths and emission directions — is required in the surface energy balance. Because emissivity acts as a multiplicative coefficient to the Stephan-Boltzmann radiation function, it has a large effect on the ability of the surface to reject heat, and thus, on the steady-state surface temperature reached by a component. The total hemispherical emissivity can be a strong function of temperature; so temperature-dependent emissivity values are usually required. Direct measurements of hemispherical emissivity at elevated temperatures are difficult, and few such data are available in the literature for UHTC materials. The measurements of Scatteia et al.^{58,59} for ZrB₂-15SiC-2MoSi₂, ZrB₂-15SiC, and ZrB₂-15SiC-10HfB₂ composites are a notable exception. Emissivity values ranged from 0.49 to 0.81, depending on material composition, temperature, machining method, and ambient oxygen environment. Scatteia et al.^{58,59} assign errors of $\pm 5\%$ to their measurements.

Often temperature-dependent emissivity values are estimated from room-temperature hemispherical spectral reflectance measurements.⁶⁰ We use optical relations for an opaque solid and Kirchhoff's law to obtain spectral emissivity from the measured spectral reflectance and then average the spectral emissivity over the Planck function at different temperatures to compute temperature-dependent total emissivity values. It is difficult to assign rigorous uncertainties to this process.

An *in situ* emissivity measurement can be made during testing in high-enthalpy facilities by simultaneous one-color and two-color radiometry, wherein the surface temperature is determined by the two-color measurement, and the emissivity is derived from the one-color measurement, using the known surface temperature. A value of 0.9 was reported by Monteverde and Savino⁶¹ for ZrB₂-15SiC samples, using this technique. However, this emissivity is a directional value appropriate for the wavelength band of the one-color radiometer and cannot be used in the energy balance without introducing major uncertainty.

Design computations often assume that all atoms reaching the surface recombine (full catalytic recombination) and that all of the exothermic energy is released to the surface (full energy accommodation). These assumptions are extremely conservative for flight and can be very unrealistic when applied in analyses of ground tests. Temperature-dependent species recombination efficiencies for some UHTC materials have been measured in laboratory experiments.^{58,59,62} Maximum values of $\gamma \cong 0.1$ were reported for oxygen atom recombination by Scatteia et al.⁵⁹ on ZrB₂-15SiC and ZrB₂-15SiC-10HfB₂ materials at 1800 K, indicating less than fully catalytic behavior. Scatteia et al.^{58,59} assigned an uncertainty of $\pm 30\%$ to their species recombination coefficient measurements. The total catalytic efficiency γ' can be derived from heat flux and surface temperature measurements during arcjet or Plasmatron tests using CFD models.^{60,63} At similar surface temperatures, Marschall et al.⁶⁰ found values of $\gamma' \cong 0.001 - 0.002$ for ZrB₂-30SiC surfaces during Plasmatron exposure, which seems to indicate that energy accommodation is also not complete. Marschall et al. demonstrated that the uncertainty in deriving γ' by this approach can reach an order of magnitude and is greatly affected by the value of surface emissivity assumed in the analysis.

The surface roughness of the material can have profound effects on the boundary layer flow. Hypersonic vehicles with sharp nose tips and WLEs are designed to operate in laminar flow environments. If the laminar boundary layer should “trip” and become turbulent, the convective heating to the surface can increase dramatically. CFD tools employ analytical models and empirical correlation methods to predict roughness-induced transitions from laminar to turbulent flow and the induced turbulent surface heating. These correlations typically make use of “average” roughness heights,⁶⁴⁻⁶⁶ derived from experimental distributions of roughness height and the peak-to-peak distance. Models that predict laminar-to-turbulent flow transitions only require the average distributed roughness height of the surface as an input. Once the flow has become turbulent, any large-scale surface roughness that rises above the laminar sublayer in the boundary layer can further augment the turbulent heating. Models to predict this augmented heating typically require the average peak-to-valley roughness height and the lateral spacing between the large roughness elements.

Note that surface properties can be strongly influenced by manufacturing techniques and tolerances, so that these properties should be measured on UHTC surfaces prepared in a similar manner as the prospective component. Additionally, exposure to a high enthalpy flow can produce significant changes in the surface topology, microstructure, and chemical composition, as the result of oxidation reactions, volatilization processes, and phase changes. Therefore, emissivity, catalytic behavior, and surface roughness should be measured on both virgin materials and samples that have been exposed to surface heating conditions similar to those expected during flight. This is another reason why the use of arcjet and Plasmatron testing is critical to understanding the performance of UHTC components. To date, little research has been reported in the literature on the catalycity, emissivity, and surface roughness of UHTC materials as a function of machining methods or environmental exposure.^{58,59,62}

6. Computational example

To present a simple computational example illustrating the effects of property variations on the thermal and mechanical response of a UHTC component, we performed finite element analyses on a representative WLE section exposed to a constant convective heat flux distribution. This distribution is based on a worst-case estimate of reentry conditions for a winged crew transfer vehicle.⁶⁷ The WLE cross-section is a cylinder-wedge configuration with a nose radius of 1 mm, a half angle of 5.6 degrees and an overall length of the 76.2 mm (3 inches). Figure 6 shows the WLE cross-section and the applied heat flux as a function of stream length coordinate (the distance along the surface starting at the stagnation point).

Transient solutions for the UHTC thermal and mechanical response to heating were obtained using MSC.Marc, a commercial fully non-linear finite element analysis package. The finite element grid was 3-dimensional and used 28640 8-noded, bi-linear elements. The UHTC surface was allowed to re-radiate energy to an environment at 300 K. A node at the aft end of the WLE model was fixed to prevent rigid body movement; the rest of the model was then allowed to expand and contract without constraint. The mechanical analyses were quasi-static — at each time step the strain was predicted, based on the CTE and current temperature distribution.

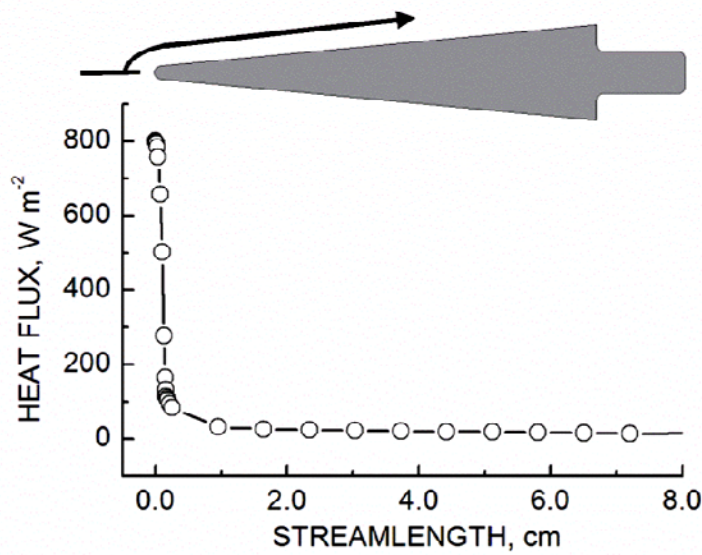


Fig. 6. Cross-section of model UHTC WLE and applied heat flux distribution.

Table 1 shows the nominal physical, thermal, mechanical, and surface properties for a monolithic hot-pressed HfB₂/SiC composite used in the analyses.^{12,43,52}

Table 1. Nominal UHTC material properties used in analysis^{12,43,52}

Property	Value
Density, kg/m ³	9520
CTE, K ⁻¹	5.96×10 ⁻⁶
Specific heat, J/(kg-K)	270 (295 K) to 500 (2000 K)
Thermal conductivity, W/(m-K)	130 (295 K) to 71 (2000 K)
Tensile modulus, GPa	530 (295 K) to 180 (2000 K)
Poisson's ratio	0.14
Emissivity	0.9

Figures 7a, 7b, 7c, and 7d show temperature, principal total strain maxima, principal tensile stress maxima, and shear stress maxima contours at the peak tensile stress time during heating (~7 seconds after application of the heat flux). While the strain contours follow the temperature contours closely, the coupled thermal/mechanical analysis reveals very different spatial distributions for temperature and stress in a complex 3-dimensional part. The locations of the highest principal tensile stresses are not in the stagnation region of leading edge, which sees the highest heat flux and experiences the highest surface temperatures, but rather in the interior of the wedge away from the leading edge and the lateral wedge faces. The highest shear stresses occur at the sides of WLE towards the leading edge and do not coincide with the locations of the highest tensile stresses.

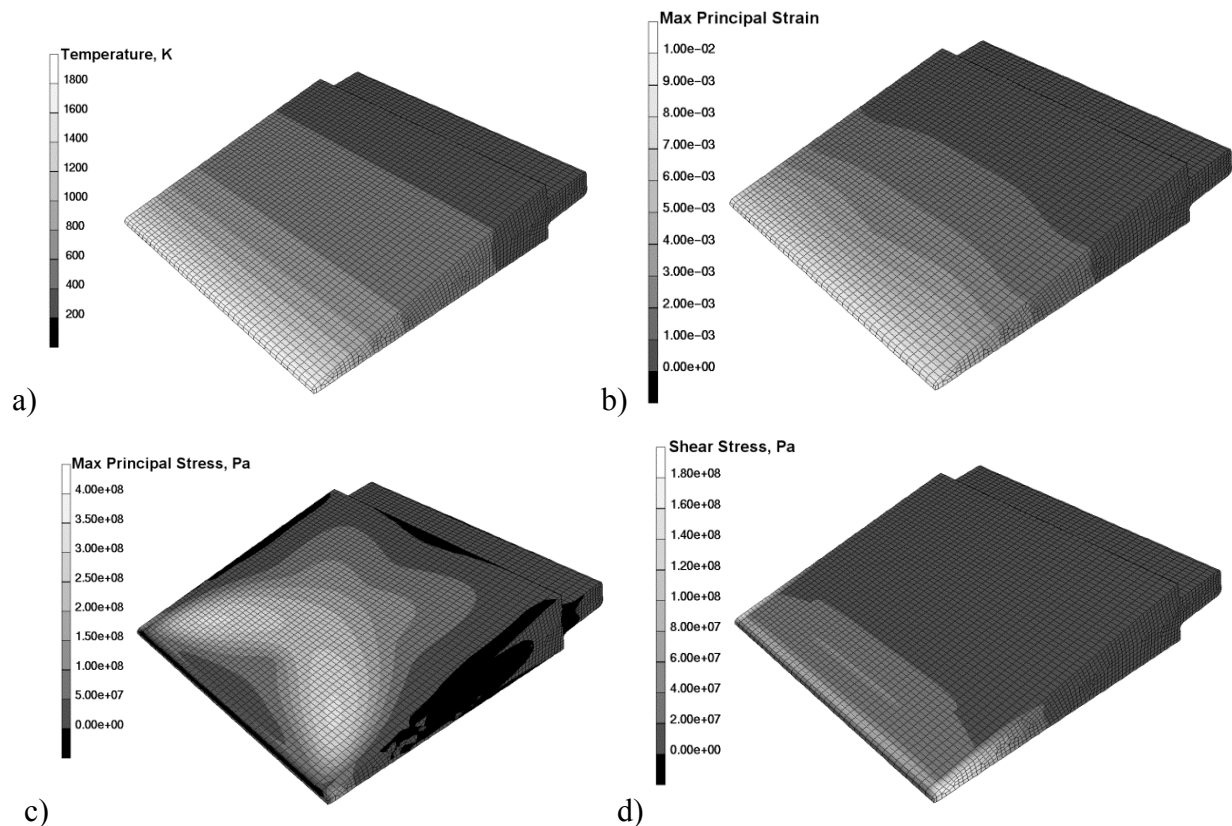


Fig. 7. Contours of a) temperature, b) principal total strain maxima, c) principal tensile stress maxima, and d) shear stress maxima, at the time of peak stress during heating, about 7 seconds after application of the heat flux.

Figure 8 shows how the magnitude of the predicted maximum principal stress is changed by dispersions about the nominal thermal conductivity and CTE values. In these computations, all other material properties were held fixed. The peak tensile stress for the nominal thermal conductivity and CTE value is 334 MPa. The highest peak stresses are found for combinations of low thermal conductivity and large CTE, as expected. A standard deviation of $\sigma = \pm 5\%$ would not be unreasonable for either property, and the inner white box shows the boundaries of possible peak stress solutions for this level of uncertainty. The outer white box shows the boundaries for a corresponding 3σ analysis, as might be done by a vehicle designer. Obviously, a much larger range of possible peak stress solutions is accessed in a 3σ analysis, since the magnitude of the reported uncertainty is amplified, and it becomes much more likely that a critical maximum stress level is exceeded.

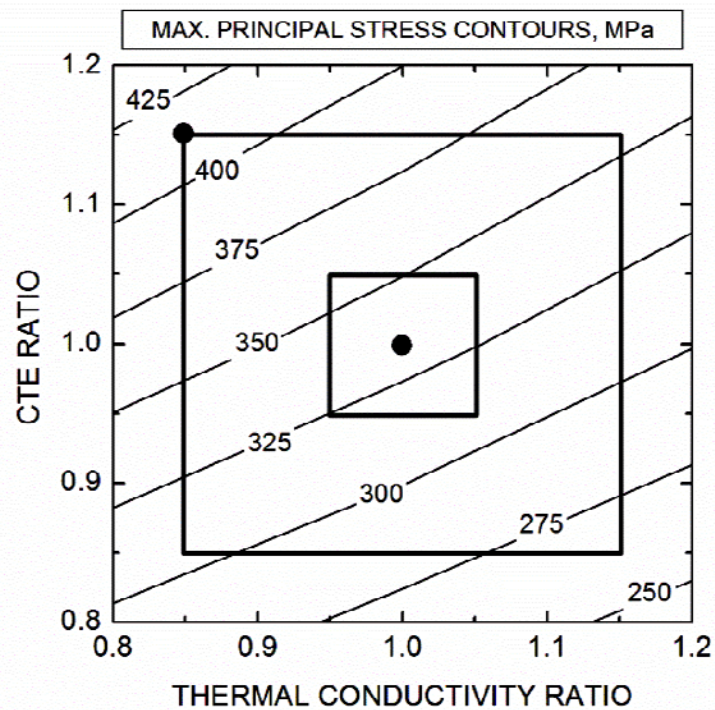


Fig. 8. Predicted maximum principal stress as a function of thermal conductivity and CTE varied about their nominal values. The center black symbol locates the maximum predicted stress (334 MPa) for the nominal property values; the inner black box is the maximum stress boundary for $\sigma = \pm 5\%$; the outer black box is the corresponding 3σ ($\pm 15\%$) boundary; the black symbol on the upper left corner of the 3σ boundary locates the maximum predicted stress (413 MPa) for the worst case combination of property values.

For brittle materials like UHTCs, statistical failure criteria are often associated with the volume of material stressed beyond a certain limit.⁴³ Figure 9 plots the volume fractions of the UHTC WLE that exceed different levels of maximum principal tensile stress, for the nominal properties, and for the worst-case 3σ combination found in Fig. 8 (that is, a conductivity ratio of 0.85 and a CTE ratio of 1.15). The volume of WLE material in which the stress level exceeds 300 MPa increases by ~450%, going from the nominal to the worst-case combination of properties.

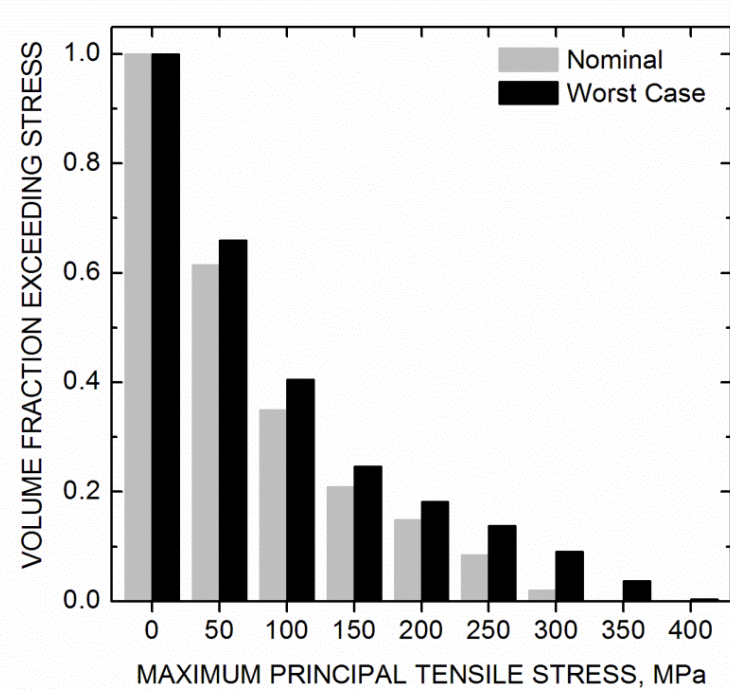


Fig. 9. The volume fraction of the UHTC WLE exceeding different levels of maximum principal tensile stress, for nominal properties and for the worst case 3σ combination (conductivity ratio of 0.85 and CTE ratio of 1.15) in Fig. 8.

Note that coincident unfavorable changes in properties that have been held at nominal values in this analysis — in particular a higher tensile modulus and emissivity — could push the maximum stress magnitudes and the volume fractions exceeding certain stress levels significantly higher.

7. Conclusions

The design and analysis of UHTC components in hypersonic applications requires a complete set of accurate material properties, along with associated uncertainties and supporting

information. Some key aspects that make UHTC property measurements more useful for analysts and designers are summarized below:

- The temperature dependence of material properties is always desired, but is especially critical for thermal conductivity, specific heat, emissivity, tensile modulus and thermal expansion coefficient (CTE).
- Measurement techniques should be referenced to standard tests, whenever possible.
- Measurements should always be reported with well-defined errors (that is, an explicit statement of what the error represents: technique, repeat measurements, sample-to-sample variability, and so forth).
- Isotropy and homogeneity of UHTC materials should be confirmed; failing that, the orientation of test specimens relative to the manufacturing process should be stated.

Material developers should strive to work closely with the application developers to deliver the best material property information possible. High fidelity material properties, together with well-defined uncertainties, statistically significant data sets, and supporting information, lead to more accurate performance predictions and a tighter design space.

Acknowledgments

The authors wish to thank Dr. Joan Fuller of the Air Force Office of Scientific Research (AFOSR) for suggesting the topic of this paper. The contributions of Jochen Marschall were supported by AFOSR contract FA9550-08-C-0049. Information for this paper was gathered from several NASA programs, including the Space Launch Initiative, Next Generation Launch Technology, and the Fundamental Aeronautics Program.

References

¹Upadhy, K., Yang, J.-M., and Hoffman, W.P., "Materials for Ultrahigh Temperature Structural Applications," *The American Ceramic Society Bulletin*, Vol. 76, No. 12, 1997, pp. 51-56.

²Fridlender, B.A., Neshpor, V.S., Ordan'yan, S.S., and Unrod, V.I., "Thermal Conductivity and Diffusivity of Binary Alloys of the ZrC-ZrB₂ System at High Temperature," *High Temperature*, Vol. 17, No. 6, 1979, pp. 1001-1005.

³Opeka, M.M., Talmy, I.G., Wuchina, E.J., Zaykoski, J.A., and Causey, S.J., "Mechanical, Thermal, and Oxidation Properties of Refractory Hafnium and Zirconium Compounds," *Journal of the European Ceramic Society*, Vol. 19, 1999, pp. 2405-2414.

⁴Kolodziej, P., Bowles, J.V., and Roberts, C., "Optimizing Hypersonic Sharp Body Concepts from a Thermal Protection System Perspective," AIAA Paper 1998-1610, April 1998.

⁵Fahrenholtz, W.G., Hilmas, G.E., Talmy, I.G., and Zaykoski, J.A., "Refractory Diborides of Zirconium and Hafnium," *Journal of the American Ceramic Society*, Vol. 90, No. 5, 2007, pp. 1347-1364.

⁶Opeka, M.M., Talmy, I.G., and Zaykoski, J.A., "Oxidation-Based Materials Selection for 2000 °C+ Hypersonic Aerosurfaces: Theoretical Considerations and Historical Experience," *Journal of Materials Science*, Vol. 39, No. 19, 2004, pp. 5887-5904.

⁷Monteverde, F. and Bellosi, A., "Oxidation of ZrB₂-Based Ceramics in Dry Air," *Journal of the Electrochemical Society*, Vol. 150, No. 11, 2003, pp. B552-B559.

⁸Clougherty, E.V., Pober, R.L., and Kaufman, L., "Synthesis of Oxidation Resistant Metal Diboride Composites," *Transactions of the Metallurgical Society of AIME*, Vol. 242, 1968, pp. 1077-1082.

⁹Tripp, W.C., Davis, H.H., and Graham, H.C., "Effect of an SiC Addition on the Oxidation of ZrB₂," *Ceramic Bulletin*, Vol. 52, No. 8, 1973, pp. 612-616.

¹⁰Chamberlain, A.L., Fahrenholtz, W.G., Hilmas, G.E., and Ellerby, D.T., "High-Strength Zirconium Diboride-Based Ceramics," *Journal of the American Ceramic Society*, Vol. 87, No. 6, 2004, pp. 1170-1172.

¹¹Monteverde, F. and Scatteia, L., "Resistance to Thermal Shock and to Oxidation of Metal Diborides-SiC Ceramics for Aerospace Application," *Journal of the American Ceramic Society*, Vol. 90, No. 4, 2007, pp. 1130-1138.

¹²Gasch, M., Ellerby, D., Irby, E., Beckman, S., Gusman, M., and Johnson, S., "Processing, Properties, and Arc Jet Oxidation of Hafnium Diboride/Silicon Carbide Ultra High Temperature Ceramics," *Journal of Materials Science*, Vol. 39, No. 19, 2004, pp. 5925-5937.

¹³Guo, S., Kagawa, Y., Nishimura, T., and Tanaka, H., "Thermal and Electrical Properties in Hot-Pressed ZrB₂-MoSi₂-SiC Composites," *Journal of the American Ceramic Society*, Vol. 90, No. 7, 2007, pp. 2255-2258.

¹⁴Sciti, D., Brach, M., and Bellosi, A., "Long-Term Oxidation Behavior and Mechanical Strength Degradation of a Pressurelessly Sintered ZrB₂-MoSi₂ Ceramic," *Scripta Materialia*, Vol. 53, 2005, pp. 1297-1302.

¹⁵Sciti, D., Brach, M., and Bellosi, A., "Oxidation Behavior of a Pressureless Sintered ZrB₂-MoSi₂ Ceramic Composite," *Journal of Materials Research*, Vol. 20, No. 4, 2005, pp. 922-930.

¹⁶Opila, E., Levine, S., and Lorincz, J., "Oxidation of ZrB₂- and HfB₂-Based Ultra-High Temperature Ceramics: Effect of Ta Additions," *Journal of Materials Science*, Vol. 39, 2004, pp. 5969-5977.

¹⁷Reuther, J., Kinney, D., Smith, S., Kontinos, D., Gage, P., and Saunders, D., "A Reusable Space Vehicle Design Study Exploring Sharp Leading Edges," AIAA Paper 2001-2884, June 2001.

¹⁸Nonweiler, T.R.F., "Heat Shield Design for Re-entry and Launch. The Use of Conduction-Assisted Radiation on Sharp-Edged Wings," *Philosophical Transactions of the Royal Society of London Series A*, Vol. 357, No. 1759, 1999, pp. 2197-2225.

¹⁹Gülhan, A. and Esser, B., "A Study on Heat Flux Measurements in High Enthalpy Flows," AIAA Paper 2001-3011, June 2001.

²⁰Smith, D.M., Moody, H., Wanstall, C., and Terrazas-Salinas, I., "The Design and Use of Calorimeters for Characterization of High-Enthalpy Flows in Arc-Heated Test Facilities," AIAA Paper 2002-5236, September 2002.

²¹Wright, M.J., Candler, G.V., and Bose, D., "Data-Parallel Line Relaxation Method for the Navier-Stokes Equations," *AIAA Journal*, Vol. 36, No. 9, 1998, pp. 1603-1609.

²²Cheatwood, F.M. and Gnoffo, P.A., "User's Manual for the Langley Aerothermodynamic Upwind Relaxation Algorithm (LAURA)," NASA TM-4764, NASA, April 1996.

²³Anon., *MSC.MARC Finite Element Program* MSC Software, Santa Ana, CA, 1994.

²⁴Chen, Y.-K., Milos, F.S., Bull, J.D., and Squire, T.H., "Integrated Analysis Tool for Ultra-High Temperature Ceramic Slender-Body Reentry Vehicles," AIAA Paper 99-0350, January, 1999.

²⁵Thomas, D.J., "Design and Analysis of UHTC Leading Edge Attachment," NASA CR 2002-211505, July 2002.

²⁶Kowalski, T., Buesking, K., Kolodziej, P., and Bull, J., "A Thermostructural Analysis of a Diboride Composite Leading Edge," NASA TM 110407, NASA, July 1996.

²⁷Kontinos, D.A., Gee, K., and Prabhu, D.K., "Temperature Constraints at the Sharp Leading Edge of a Crew Transfer Vehicle," AIAA Paper 2001-2886, June 2001.

²⁸Scatteia, L., Riccio, A., Rufolo, G., Filippis, F.D., Vecchio, A.D., and Marino, G., "PRORA-USV SHS: Ultra High Temperature Ceramic Materials for Sharp Hot Structures," AIAA Paper 2005-3266, May 2005.

²⁹Savino, R., De Stefano Fumo, M., Paterna, D., and Serpico, M., "Aerothral Study of UHTC-Based Thermal Protection Systems," *Aerospace Science and Technology*, Vol. 9, 2005, pp. 151-160.

³⁰Monti, R., de Stefano Fumo, M., and Savino, R., "Thermal Shielding of a Reentry Vehicle by Ultra-High-Temperature Ceramic Materials," *Journal of Thermophysics and Heat Transfer*, Vol. 20, No. 3, 2006, pp. 500-506.

³¹Mulville, D.R., "Structural Design and Test Factors of Safety for Spaceflight Hardware," NASA-STD-5001, NASA, June 1996.

³²Olynick, D., Loomis, M., Chen, Y.-K., Venkatapathy, E., and Allen, G., "New TPS Design Stratagies for Planetary Entry Vehicle Design," AIAA Paper 1999-0348, January 1999.

³³Rasky, D.J., Kolodziej, P., Newfield, M.E., Laub, B., and Chen, Y.-K., "Assessing Factors of Safety, Margins of Safety, and Reliability of Thermal Protection Systems," AIAA Paper 2003-4043, June 2003.

³⁴Sherman, M.M., "Entry Thermal Protection," NASA-SP-8014, NASA, August 1968.

³⁵Squire, T.H., Milos, F.S., and Hartlieb, G.C., "Aerospace Materials Property Database (TPSX)," *Journal of Spacecraft and Rockets*, Vol. 46, No. 3, 2009, pp. 733-736.

³⁶Chen, Y.-K., Squire, T., Laub, B., and Wright, M., "Monte Carlo Analysis for Spacecraft Thermal Protection System Design," AIAA Paper 2006-2951.

³⁷Cowan, R.D., "Pulse Method of Measuring Thermal Diffusivity at High Temperatures," *Journal of Applied Physics*, Vol. 34, No. 4, 1963, pp. 926-927.

³⁸Chamberlain, A.L., Fahrenholtz, W.G., and Hilmas, G.E., "Pressureless Sintering of Zirconium Diboride," *Journal of the American Ceramic Society*, Vol. 89, No. 2, 2006, pp. 450-456.

³⁹Zhu, A., Fahrenholtz, W.G., and Hilmas, G.E., "Influence of Silicon Carbide Particle Size on the Microstructure and Mechanical Properties of Zirconium Diboride-Silicon Carbide Ceramics," *Journal of the European Ceramic Society*, Vol. 27, 2007, pp. 2077-2083.

⁴⁰Monteverde, F., "Progress in the Fabrication of Ultra-High-Temperature Ceramics: "in situ" Synthesis, Microstructure and Properties of a Reactive Hot-Pressed HfB₂-SiC Composite," *Composite Science and Technology*, Vol. 65, 2005, pp. 1869-1879.

⁴¹Monteverde, F. and Bellosi, A., "Development and Characterization of Metal-Diboride-Based Composites Toughened with Ultra-Fine SiC Particulates," *Solid State Sciences*, Vol. 7, 2005, pp. 622-630.

⁴²Monteverde, F., Guicciardi, S., and Bellosi, A., "Advances in Microstructure and Mechanical Properties of Zirconium Diboride Based Ceramics," *Materials Science and Engineering*, Vol. A346, 2003, pp. 310-319.

⁴³Bull, J., Kolodziej, P., Salute, J., and Keese, D., "Design, Instrumentation and Preflight Testing of a Sharp Ultra-High Temperature Ceramic Nosecone," NASA TM-1998-112229, October 1998.

⁴⁴Marschall, J., Erlich, D.C., Manning, H., Duppler, W., Ellerby, D., and Gasch, M., "Microhardness and High-Velocity Impact Resistance of HfB₂/SiC and ZrB₂/SiC Composites," *Journal of Materials Science*, Vol. 39, No. 19, 2004, pp. 5959-5968.

⁴⁵Sanders, W.A. and Probst, H.B., "Hardness of Five Borides at 1625 °C," *Journal of the American Ceramic Society*, Vol. 49, No. 4, 1966, pp. 231-232.

⁴⁶Fahrenholtz, W.G., Hilmas, G.E., Chamberlain, A.L., and Zimmermann, J.W., "Processing and Characterization of ZrB₂-Based Ultra-High Temperature Monolithic and Fibrous Monolithic Ceramics," *Journal of Materials Science*, Vol. 39, 2004, pp. 5951-5957.

⁴⁷Monteverde, F., "Ultra-High Temperature HfB₂-SiC Ceramics Consolidated by Hot-Pressing and Spark Plasma Sintering," *Journal of Alloys and Compounds*, Vol. 428, 2007, pp. 197-205.

⁴⁸Monteverde, F., Bellosi, A., and Guicciardi, S., "Processing and Properties of Zirconium Diboride-Based Composites," *Journal of the European Ceramic Society*, Vol. 22, 2002, pp. 279-288.

⁴⁹Monteverde, F., Melandri, C., and Guicciardi, S., "Microstructure and Mechanical Properties of an HfB₂ + 30 vol. % SiC Composite Consolidated by Spark Plasma Sintering," *Materials Chemistry and Physics*, Vol. 100, 2006, pp. 513-519.

⁵⁰Kalish, D., Clougherty, E.V., and Kreder, K., "Strength, Fracture Mode, and Thermal Stress Resistance of HfB₂ and ZrB₂," *Journal of the American Ceramic Society*, Vol. 52, No. 1, 1969, pp. 30-36.

⁵¹Keihn, F.G. and Keplin, E.J., "High-Temperature Thermal Expansion of Certain Group IV and Group V Diborides," *Journal of the American Ceramic Society*, Vol. 50, No. 2, 1967, pp. 81-84.

⁵²Gasch, M., Johnson, S., and Marschall, J., "Thermal Conductivity Characterization of Hafnium Diboride-Based Ultra High Temperature Ceramics," *Journal of the American Ceramic Society*, Vol. 91, No. 5, 2008, pp. 1423-1432.

⁵³Guo, S.-Q., Kagawa, Y., Nishimura, T., Chung, D., and Yang, J.-M., "Mechanical and Physical Behavior of Spark Plasma Sintered ZrC-ZrB₂-SiC Composites," *Journal of the European Ceramic Society*, Vol. 28, 2008, pp. 1279-1285.

⁵⁴Zimmermann, J.W., Hilmas, G.E., Fahrenholtz, W.G., Dinwiddie, R.B., Porter, W.D., and Wang, H., "Thermophysical Properties of ZrB₂ and ZrB₂-SiC Ceramics," *Journal of the American Ceramic Society*, Vol. 91, No. 5, 2008, pp. 1405-1411.

⁵⁵Tye, R.P. and Clougherty, E.V., "The Thermal and Electrical Conductivities of Some Electrically Conducting Compounds, in, Newton, MA, 1970 (ASME), p. 396-401.

⁵⁶Wuchina, E., Opeka, M., Causey, S., Buesking, K., Spain, J., Cull, A., Routbort, J., and Gutierrez-Mora, F., "Designing for Ultrahigh-Temperature Applications: The Mechanical and Thermal Properties of HfB₂, HfC_x, HfN_x and a-Hf(N)," *Journal of Materials Science*, Vol. 39, 2004, pp. 5939-5949.

⁵⁷Wuchina, E., Opeka, M., Gutierrez-Mora, F., Koritala, R.E., Goretta, K.C., and Routbort, J.L., "Processing and Mechanical Properties of Materials in the Hf-N System," *Journal of the European Ceramic Society*, Vol. 22, 2002, pp. 2571-2576.

⁵⁸Scatteia, L., Borrelli, R., Cosentino, G., Bêche, E., Sans, J.-L., and Balat-Pichelin, M., "Catalytic and Radiative Behaviors of ZrB₂-SiC Ultrahigh Temperature Ceramic Composites," *Journal of Spacecraft and Rockets*, Vol. 43, No. 5, 2006, pp. 1004-1012.

⁵⁹Scatteia, L., Alfano, D., Monteverde, F., Sans, J.-L., and Balat-Pichelin, M., "Effect of Machining Method on the Catalytic and Emissivity of ZrB₂ and ZrB₂-HfB₂-Based Ceramics," *Journal of the American Ceramic Society*, Vol., 2008, pp.

⁶⁰Marschall, J., Pejaković, D.A., Fahrenholtz, W.G., Hilmas, G.E., Zhu, S., Ridge, J., Fletcher, D.G., Asma, C.O., and Thömel, J., "Oxidation of ZrB₂-SiC Ultra-High Temperature Ceramic Composites in Dissociated Air," *Journal of Thermophysics and Heat Transfer*, Vol. 23, No. 2, 2009, pp. 267-278.

⁶¹Monteverde, F. and Savino, R., "Stability of Ultra-High Temperature ZrB₂-SiC Ceramics Under Simulated Atmospheric Re-Entry Conditions," *Journal of the European Ceramic Society*, Vol. 27, 2007, pp. 4797-4805.

⁶²Marschall, J., Chamberlain, A., Crunkleton, D., and Rogers, B., "Catalytic Atom Recombination on ZrB₂/SiC and HfB₂/SiC Ultrahigh-Temperature Ceramic Composites," *Journal of Spacecraft and Rockets*, Vol. 41, No. 4, 2004, pp. 576-581.

⁶³Savino, R., De Stefano Fumo, M., Silvestroni, L., and Sciti, D., "Arc-Jet Testing on HfB₂ and HfC-based Ultra-High Temperature Ceramic Materials," *Journal of the European Ceramic Society*, Vol. 28, 2008, pp. 1899-1907.

⁶⁴Reda, D.C., "Correlation of Noisetip Boundary-Layer Transition Data Measured in Ballistic-Range Experiments," *AIAA Journal*, Vol. 19, No. 3, 1981, pp. 329-339.

⁶⁵Reda, D.C., "Review and Synthesis of Roughness-Dominated Transition Correlations for Reentry Applications," *Journal of Spacecraft and Rockets*, Vol. 39, No. 2, 2002, pp. 161-167.

⁶⁶Reda, D.C., Wilder, M.C., Bogdanoff, D.W., and Prabhu, D.K., "Transition Experiments on Blunt Bodies with Distributed Roughness in Hypersonic Free Flight," AIAA Paper 2007-306, January 2007.

⁶⁷Kinney, D.J., Bowles, J.V., Yang, L.H., and Roberts, C.D., "Conceptual Design of a "SHARP"-CTV," AIAA Paper 2001-2887, June 2001.